Novel approaches to singlet oxygen photosensitization in the nano- and bio-era

Oriol Planas Marquès

DOCTORAL THESIS

Title	**Novel approaches to singlet oxygen photosensitization in the *nano*- and *bio*-era**
Presented by	**Oriol Planas Marquès**
Centre	**IQS School of Engineering**
Department	**Analytical and Applied Chemistry**
Directed by	**Prof. Dr. Santi Nonell Marrugat**

C. Claravall, 1-3 | 08022 Barcelona | Tel. 93 602 22 00 | Fax 93 602 22 49 | info@url.edu | www.url.edu

To my mother, father and brother

To all fotoQs & Eli

ACKNOWLEDGMENTS

Financial support for this research has been provided by the Spanish Ministerio de Economía y Competitividad through grants No. CTQ2013-48767-C3-1-R and CTQ2016-78454-C2-1-R.

I would like to thank the European Social Funds and the SUR del DEC de la Generalitat de Catalunya for my predoctoral fellowship (grants No. 2014FI_B00777, 2015FI_B1 00063 and 2016FI_B2 00100). Additional financial support from the European Molecular Biology Organization (EMBO) for visiting the Philipps Universität of Marburg (grant No. ASTF 337 – 2016), from the European Society for Photobiology (ESP) for attending the 16th Congress of the ESP and from the Organic Division of the Royal Society of Chemistry and the Society of Porphyrins and Phthalocyanines for attending the 9th International Conference on Porphyrins and Phthalocyanines (ICPP-9) are gratefully acknowledged.

I a tot els que heu estat amb mi durant aquests quasi 4 anys...

MOLTES GRÀCIES!

ABSTRACT

Different new molecular, bio- and nano-engineered approaches to enhance the photosensitization and detection of singlet oxygen in biological media are reported in this thesis.

First, a novel fluoro-chromogenic click reaction for the labeling of proteins and nanoparticles with porphycene derivatives is presented. Reaction of porphycene isothiocyanate with primary and secondary amines yields 2-aminothiazolo[4,5-c]porphycene derivatives with a concomitant red-shift of their absorption and fluorescence emission spectra by more than 70 nm. This unexpected reaction has been explained on the grounds of a spontaneous cyclization of the initially-formed 9-thiourea porphycene derivative onto a fused thiazoloporphycene and its scope has been expanded to other porphycene derivatives such as 9-amidoporphycenes. Furthermore, porphycene isothiocyanates have been used to label biomolecules and nanoparticles yielding near-infrared theranostic nanoconjugates.

Secondly, the role of the morphology of silica nanoparticles onto the production and deactivation of singlet oxygen by protoporphyrin IX has been investigated. Aggregation of the photosensitizer onto the surface of the nanoparticle limits the production of singlet oxygen. In addition, as the porosity of the nanomaterial increases, different populations of singlet oxygen can be detected; one population is able to escape from the nanoparticle surface and decay in the bulk solvent while the other is trapped inside the silica pores. Results reveal that controlling the aggregation state of the photosensitizer and its location is of crucial importance when preparing nanoporous materials for singlet oxygen delivery.

Finally, plasmonic photosensitizers capable of boosting the production and radiative decay of single oxygen have been designed and studied. Via time-resolved and steady state spectroscopic techniques, we demonstrate the silver core exerts a dual role of enhancing both the production of singlet oxygen, through enhanced absorption of light, and its radiative decay, which in turn boosts singlet oxygen phosphorescence emission to a greater extent. Furthermore, we show both the enhancement of the production and the emission of singlet oxygen to be dependent on proximity to the plasmonic nanostructure. Three distinct regimes have been identified as the photosensitizer moves apart the plasmonic nanostructure, with greater enhancement at distances between 10 and 20 nm. Moreover, hybrid plasmonic nanoparticles can be delivered to both Gram-positive and Gram-negative bacteria boosting both photoantibacterial activity and detection limit of singlet oxygen in cells.

RESUMEN

En esta tesis se detallan nuevas aproximaciones nano- y biomoleculares para mejorar la fotosensibilización y detección del oxígeno singlete en medio biológico.

En primer lugar se presenta una nueva reacción fluoro- y cromogénica para el etiquetado de proteínas y nanopartículas con derivados de porficeno. Concretamente, la reacción de porficenos isotiocianato con aminas primarias y secundarias genera 2-aminotiazolo[4,5-c]porficeno derivados con un desplazamiento concomitante en sus espectros de absorción y emisión por más de 70 nm. Esta reacción inesperada ha sido racionalizada en base a la ciclación espontánea del derivado 9-tiourea porficeno generado tras la reacción para dar lugar a un tiazoloporficeno fusionado. El alcance de dicha reacción ha sido expandido a otros derivados de porficeno como los 9-amidoporficenos. Finalmente, los porficenos isotiocianato han sido usados para el marcaje de biomoléculas y nanopartículas, dando nanoconjugados teranósticos en el infrarrojo cercano.

En segundo lugar, se ha sido estudiado el efecto de la morfología de las nanopartículas de sílice sobre la capacidad de producción y desactivación de oxígeno singlete por protoporfirina IX. La agregación del fotosensibilizador en la superficie de la nanopartícula limita la producción de oxígeno singlete. Por otro lado, a medida que aumenta la porosidad del nanomaterial es posible detectar distintas poblaciones de oxígeno singlete; una de ellas capaz de escapar de la superficie de las nanopartículas y decaer en el disolvente mientras que la otra se mantiene atrapada dentro de los poros de sílice. Los resultados revelan que controlar el grado de agregación del fotosensibilizador y su localización en la red de sílice son factores críticos a tener en cuenta en la preparación de materiales nanoporosos para liberación de oxígeno singlete.

Finalmente se han diseñado y estudiado fotosensibilizadores plasmónicos capaces de aumentar la producción y el decaimiento radiante del oxígeno singlete. Mediante técnicas de espectroscopia estacionaria y resuelta en el tiempo se demuestra que el núcleo de plata ejerce un efecto dual mediante la absorción incrementada de luz y el aumento del decaimiento radiante del oxígeno singlete, lo que se traduce en un mayor aumento de su fosforescencia. Además se demuestra que el aumento en la producción y en decaimiento radiante del oxígeno singlete depende enormemente de la proximidad del fotosensibilizador a la nanopartícula plasmónica. Así, se han identificado 3 regímenes distintos a medida que el fotosensibilizador se aleja de la nanoestructura plasmónica, situándose el máximo factor de aumento a distancias entre 10 y 20 nm del núcleo metálico. Adicionalmente, las nanopartículas plasmónicas se han usado en bacterias Gram-positivas y Gram-negativas, observando un aumento tanto de su actividad antimicrobiana como en el límite de detección de oxígeno singlete.

RESUM

En aquesta tesis es detallen noves aproximacions nano- i biomoleculars amb l'objectiu de millorar la fotosensibilització i detecció d'oxigen singlet en medi biològic.

En primer lloc es presenta una nova reacció fluoro- i cromogènica pel marcatge de proteïnes i nanopartícules amb derivats de porficè. Concretament, la reacció de porficens isotiocianat amb amines primàries i secundaries generen 2-aminotiazolo[4,5-c]poricè derivats amb un desplaçament concomitant en els seus espectres d'absorció i emissió per més de 70 nm cap al vermell. Aquesta reacció inesperada ha estat racionalitzada en base a la ciclació espontània del derivat 9-tiourea porficè generat en la reacció per donar lloc a un tiazoloporficè fusionat. L'abast de tal reacció s'ha expandit a altres derivats de porficè com els 9-amidoporficens. Finalment, s'ha utilitzat porficens isotiocianat pel marcatge de biomolècules i nanopartícules, lliurant conjugats teranòstics al infraroig proper.

En segon lloc s'ha estudiat l'efecte de la morfologia de les nanopartícules se sílice sobre la capacitat de producció i desactivació d'oxigen singlet per part de la protoporfirina IX. L'agregació del fotosensibilitzador en la superfície de la nanopartícula limita la producció d'oxigen singlet. Per altra banda, a mesura que augmenta la porositat del nanomaterial es possible detectar diferents poblacions d'oxigen singlet; una d'elles és capaç d'escapar de la superfície de les nanopartícules i de decaure en el dissolvent mentre que l'altra es manté atrapada dins dels porus de sílice. Els resultats revelen que controlar el grau d'agregació del fotosensibilitzador i la seva localització en la matriu de sílice són factors crítics a tenir en compte en la preparació de materials nanoporosos per a l'alliberació d'oxigen singlet.

Finalment s'han dissenyat i estudiat fotosensibilizadors plasmònics capaços d'augmentar la producció i el decaïment radiant del oxigen singlet. Mitjançant tècniques de espectroscòpia estacionària i resoltes en el temps es demostra que el nucli de plata exerceix un efecte dual a través d'una absorció incrementada de llum i un augment en el decaïment radiant d'oxigen singlet, fet que es tradueix en un augment de la seva fosforescència. A més a més es demostra que l'augment en la producció i en el decaïment radiant d'oxigen singlet depèn enormement de la proximitat entre fotosensibilitzador i nanopartícula plasmònica. D'aquesta manera s'han identificat 3 règims diferents a mesura que el fotosensibilitzador s'allunya de la nanoestructura plasmónica, essent la zona de major augment aquella compresa en distancies entre 10 i 20 nm del nucli metàl·lic. Addicionalment s'han utilitzat les nanopartícules per el tractament fotodinàmic de bactèries Gram-positives i Gram-negatives, observant un augment tant de la seva activitat antimicrobiana com en el límit de detecció d'oxigen singlet.

TABLE OF CONTENTS

1

Introduction

A general introduction to the subjects of the thesis is given in this chapter, along with the main objectives of this work and the disclosure of my contributions to the papers derived thereof. The current challenges facing the photosensitization of singlet oxygen are reviewed, together with the state of the art of molecular, bio- and nano-engineering approaches to photoinduced singlet oxygen production.

1.1. Singlet molecular oxygen

1.1.1. Ground and electronically excited states of molecular oxygen

Molecular oxygen is a diatomic homonuclear molecule which, despite its apparent simplicity, exhibits rather unusual properties with respect to its magnetic behavior, spectroscopy, energy transfer processes and chemical reactivity. These singularities come as a result of the particular electronic configuration of its ground and excited states.[1]

The electronic configuration of O_2 in its ground state is $(1\sigma_g)^2(1\sigma_u)^2(2\sigma_g)^2(2\sigma_u)^2(3\sigma_g)^2(3\sigma_u)^2(3\pi_g)^4(3\pi_u)^2$. Unlike other homonuclear molecules, ground state molecular oxygen has an open shell electronic configuration with two unpaired electrons which, according to Hund's rule, occupy different molecular orbitals (Figure 1.1). This electronic configuration is commonly designated with the terminology O_2 ($^3\Sigma_g^-$) or $^3O_2$; the superscript "3" indicates that it corresponds to a triplet state; the "Σ", that its orbital angular momentum (M_L) equals 0; and the subscript "g", that the symmetry of the molecule is pair (g from the German *gerade*). The two lowest-energy excited states of oxygen are both spin singlet states and have pair parity, but differ in M_L (Figure 1.1). The lowest-energy singlet excited state, O_2 ($^1\Delta_g$) or $^1O_2$, has an M_L equal to 2, depicted with the Δ symbol. On the other hand, the M_L of the next higher-energy singlet excited state is 0, being another sigma state, O_2 ($^1\Sigma_g^+$).

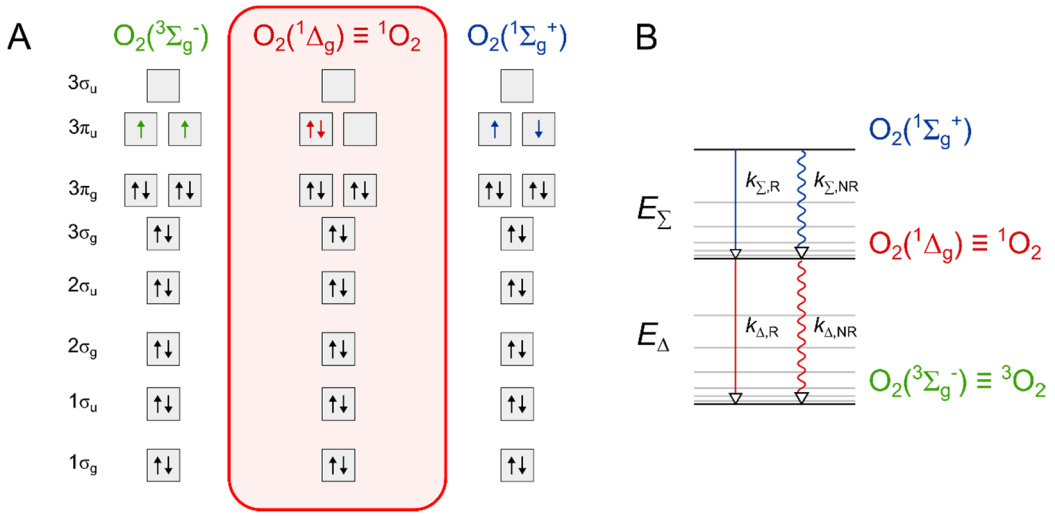

Figure 1.1. (A) Electronic configuration of ground state molecular oxygen O_2 ($^3\Sigma_g^-$), its first singlet excited state, O_2 ($^1\Delta_g$) namely singlet oxygen $^1O_2$, and its higher-energy singlet state, O_2 ($^1\Sigma_g^+$). (B) Jablonsky diagram of molecular oxygen and its first singlet excited states. Figure reproduced from ref. 1.

As for the thermodynamics of the ground and excited states of molecular oxygen, $^1O_2$ lies 94.3 kJ·mol^{-1} (E_Δ) above the ground state and O_2 ($^1\Sigma_g^+$) is 63 kJ·mol^{-1} higher in energy than the former (E_Σ, Figure 1.1). On the basis of these energy levels, luminescence decays of excited singlet states of oxygen are detected at 1270 nm ($^1O_2 \rightarrow {}^3O_2 + h\upsilon$) and at 762 nm ($O_2$ ($^1\Sigma_g^+$) $\rightarrow {}^3O_2 + h\upsilon$).

1.1.2. Reactivity of singlet oxygen

Oxidation reactions of organic molecules from ground state molecular oxygen are forbidden in terms of the spin angular momentum conservation (Wigner's rule).[2] According to this principle, the number of unpaired electrons must remain unaltered before and after each individual step of a reaction. Since ground state molecular oxygen is a triplet state and organic substrates are spin singlets, their reaction cannot proceed in an individual step (Scheme 1.1). Instead, the oxidation of organic compounds from ground state molecular oxygen proceeds following a radical pathway whereby different external stimuli initiate the production of radical species of the substrate ($R^{\bullet}$ or $ROO^{\bullet}$) that participate in radical chain reactions (Scheme 1.1). For example, a common way of autoxidation of organic compounds in the atmosphere is the so-called H-shift chemistry of peroxy radicals according to which the abstraction of an hydrogen of an unsaturated system by hydroxyl ($OH^{\bullet}$) or chlorine ($Cl^{\bullet}$) radicals leads to the formation of radical species ($R^{\bullet}$).[3] The reaction of these radical species with molecular oxygen results in the formation of a peroxyl radicals (R-$OO^{\bullet}$) which can further react in subsequent propagation steps.

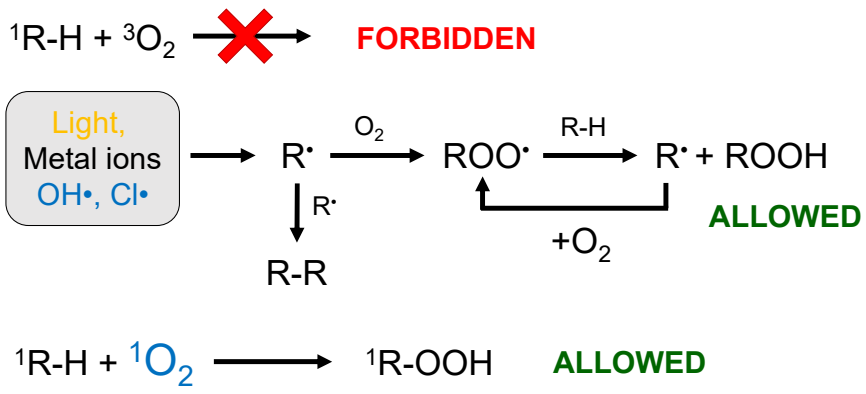

Scheme 1.1. Pathways for the autoxidation of organic substrates by molecular oxygen and $^1O_2$.

Contrary to ground state molecular oxygen, $^1O_2$ has the right spin to carry out the oxidation of organic compounds (Scheme 1.1). Accordingly, $^1O_2$ is kinetically far more reactive than $^3O_2$ due to its particular spin multiplicity. $^1O_2$ is highly reactive towards a broad variety of molecules and biomolecules, particularly lipids, proteins and nucleic acids. Moreover, an additional advantage of $^1O_2$ is that it is able to diffuse through the biological medium, which allows it to reach targets distant from the site of its generation and cause remote oxidative damage.[2]

1.1.3. Photodynamic therapy

Given its high reactivity and diffusion capability, $^1O_2$ has a preeminent position in the so called photodynamic therapy (PDT). PDT is a clinically approved phototherapeutic modality for the treatment of malignant and non-malignant diseases as well as pathogenic infections.[4–6] The treatment protocol is based on the administration of a photoactive drug, called photosensitizer (PS), followed by light exposure in the presence of oxygen. The combination of these three elements, all of them deprived of any cytotoxic effect *per se*, leads to the production of reactive oxygen species (ROS) capable of inflicting sever oxidative damage to a wide range of cell components (Figure 1.2).

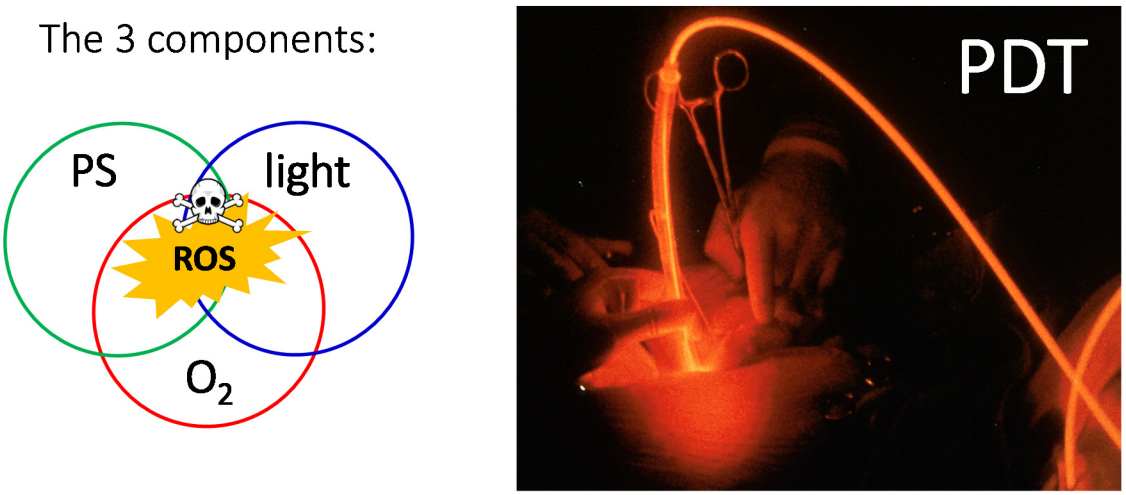

Figure 1.2. Photodynamic therapy is a clinically approved therapeutic modality based on the combination of 3 elements, namely a PS, light and oxygen to generate ROS which exert cellular damage. Photograph taken by John Crawford (National Cancer Institute) and licensed in Wikimedia Commons (ID 2267).

The photodynamic treatment is a 2-step process: first the PS is administered to the patient either systematically or locally and it is left to accumulate in the malignant tissue in the dark for a certain time. When the ratio of PS in the malignant tissue respect to the healthy one is considered to be maximal, light of appropriate wavelength is delivered in a convenient dose to the malignant area. Generation of ROS of high and unspecific reactivity ultimately cause the cell death via apoptosis, necrosis or autophagy. Due to its multi-target mode of action, the scope of PDT expands from the treatment of cancer cells, with the approval of 15 PSs for clinical use and several others undergoing clinical trials, to the treatment of microbial infections.[7] However, the inherent broad-reactivity of ROS makes that during PDT treatment both healthy and unhealthy cells will be damaged equally unless a precise localization of the PS or light is achieved. Since light can diffuse through tissues, it is critical to assure the PS location with respect to the healthy tissue to achieve more selective PDT treatments. Therefore, new methodologies to enhance the selectivity of this therapy are urgently needed.

1.2. Photosensitization of singlet oxygen

1.2.1. The photosensitization process

The most ubiquitous way to produce $^1O_2$ with spatiotemporal control is the photosensitization process, whereby a molecule referred to as the photosensitizer (PS) in its singlet or triplet excited states transfers its energy to molecular oxygen yielding $^1O_2$. In the literature many authors classified photosensitized reactions into two broad categories considering the nature of the resulting species, named Type I and Type II photosensitization processes.[8] Accordingly, Type-I photosensitization proceeds through radical intermediates whereas Type-II photosensitization is based on the neutral diradical $^1O_2$. However, nowadays the mechanism of many photosensitized reactions can be known in extreme detail and thus it appears more convenient to classify them according to the primary element transferred from PS (either **charge** or **energy**) and to specify the acceptor molecule involved.[9]

The photochemical mechanism of a PS in its excited state is generally depicted using a Jablonsky diagram. A simplified Jablonsky diagram can be found in Figure 1.3. Upon light absorption, an electron of the PS in its ground singlet state (^{1}PS) is promoted to a higher-energy orbital while conserving its spin. The excited state of PS rapidly relaxes to the first excited singlet state (^{1}PS*) via non-radiative processes (either vibrational relaxation or internal conversion). According to Kasha's rule, photochemical and photophysical processes occur from the first excited singlet state.

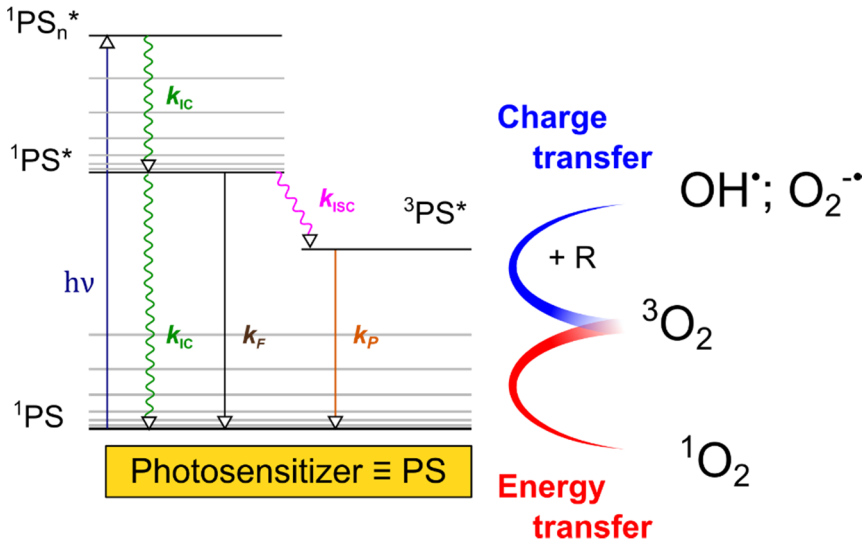

Figure 1.3. Jablonski diagram representing the energetic states of a PS, the photophysical processes occurring upon light absorption and the charge transfer or energy transfer processes leading to the generation of different ROS; where IC: internal conversion; ISC: intersystem crossing; F: fluorescence; P: phosphorescence; R: biological substrate

There are several pathways by which ^{1}PS* can release its excess of energy. The most popular ways are internal conversion or photon emission (fluorescence). Alternatively, the promoted electron in the singlet excited state can also experience a change on its spin in a process referred to as intersystem crossing to the first excited triplet state (^{3}PS*). Finally, a forth deactivation mechanism is possible by which ^{1}PS* transfers its energy to molecular oxygen yielding $^1O_2$ and the photosensitizer in its triplet excited state (^{3}PS*). However, the later process requires for sufficiently long lived singlet excited states.[10]

From the triplet excited state, ^{3}PS* can return to its ground singlet state by radiative processes (phosphorescence) or by internal conversion. However, in contrast to the deactivation of ^{1}PS*, the transition $^3PS^* \rightarrow {}^1$PS is forbidden as it implies a change on its spin. As a result, triplet excited states have 1000-fold longer lifetimes than singlet excited states. Being considerably long-lived excited states and of convenient spin, ^{3}PS* can **transfer its energy** to molecular oxygen yielding ^{1}PS and $^1O_2$ in a process where the total spin multiplicity is conserved.

Given that triplet states are endowed with long lifetimes (10^{-6} to hours), other photochemical mechanisms can compete with $^1O_2$ photosensitization from ^{3}PS*. For example, ^{3}PS* can transfer its energy to molecules different to molecular oxygen, as it has been proposed for some phototoxic reactions.[11] This mechanism demands for biomolecules of sufficiently low-lying excited states to accept energy from ^{3}PS*, such as carotenoids.[12–15] Apart from energy transfer processes, ^{3}PS* is in addition prone to undergo **charge transfer processes**. For example, certain biological substrates (R) can directly accept or transfer an electron to ^{3}PS*.[16] The resulting anion or cation radicals of R can further react with molecular oxygen yielding other ROS, such as superoxide radical ($O_2^{-\bullet}$) or hydroxyl radical ($OH^\bullet$).

Other interesting oxygen-independent pathways have been recently reported, including charge transfer from an excited PS to azide,[17,18] iodide[19] or bromide[20] anions, which have shown to be effective enhancers for the PDT inactivation of bacteria.

All the above mentioned reactions, along with light emission and heat dissipation from the excited state of the PS compete with $^1O_2$ photosensitization. Thus, in order to enhance the performance of molecular PSs, energy transfer to molecular oxygen should be favored while avoiding their deactivation through heat dissipation, light emission or charge transfer processes. Another alternative to enhance the production of $^1O_2$ comprises the use of plasmonic nanostructures, which will be addressed in the subsequent sections (section 1.5.3).

1.2.2. Singlet oxygen quantum yield

The ability of a PS to generate $^1O_2$ is quantified by its quantum yield of photosensitized $^1O_2$ production (Φ_Δ), which can be defined as the number of $^1O_2$ molecules generated per photon absorbed by a PS. Φ_Δ can be estimated considering the various photophysical and photochemical pathways involved in the generation of $^1O_2$. For the vast majority of PSs, whose singlet excited state is not capable of generating singlet oxygen, the most important pathways that ultimately yield $^1O_2$ are the following:[21]

Description	Reaction	
Singlet State Processes		
Light Absorption	$PS + h\upsilon_{exc} \longrightarrow {}^1PS^*$	(Eq. 1)
PS fluorescence	${}^1PS^* \xrightarrow{k_F} PS + h\upsilon_F$	(Eq. 2)
Internal Conversion	${}^1PS^* \xrightarrow{k_{IC}} PS$	(Eq. 3)
Intersystem Crossing	${}^1PS^* \xrightarrow{k_{ISC}} {}^3PS^*$	(Eq. 4)
Triplet State Processes		
PS phosphorescence	${}^3PS^* \xrightarrow{k_P} PS + h\upsilon_P$	(Eq. 5)
Non-Radiative decay	${}^3PS^* \xrightarrow{k_{T,NR}} PS$	(Eq. 6)
Energy transfer	${}^3PS^* + O_2 \xrightarrow{k_{T,\Delta}^{O_2}} PS + {}^1O_2$	(Eq. 7)
Other: Charge transfer processes	${}^3PS^* + O_2 \xrightarrow{k_{T,CT}^{O_2}} Other$	(Eq. 8)

Scheme 1: Summary of the elementary steps leading to $^1O_2$ production in a homogeneous system.

Considering the previous processes one can express the $^1O_2$ quantum yield of a triplet PS as:[21,22]

$$\Phi_\Delta = \Phi_T \times P_T^{O_2} \times f_{T,\Delta}^{O_2} \qquad \text{(Eq. 9)}$$

where Φ_T is the triplet quantum yield of the PS, $P_T^{O_2}$ the proportion of ^{3}PS* molecules quenched by oxygen and $f_{T,\Delta}^{O_2}$ the fraction of ^{3}PS* molecules quenched by O_2 which gives $^1O_2$. Thus, the main conclusion inferred from the above equation is that the number of $^1O_2$ molecules produced per absorbed photon is basically determined by 3 factors: (1) the ability of the PS molecule to undergo intersystem crossing from the singlet state to the triplet excited state, characterized by Φ_T; (2) the ability of oxygen to trap ^{3}PS* molecules before it decay, expressed by $P_T^{O_2}$; and (3) the efficiency of energy transfer from ^{3}PS* to molecular oxygen, $f_{T,\Delta}^{O_2}$.

1.3. Photosensitizers

1.3.1. Molecular photosensitizers

Standard molecular PSs are commonly organic planar molecules with highly delocalized π-orbitals capable of transferring charge or energy to molecular oxygen. In line with equation 9, from a photophysical and photochemical point of view molecular PSs with high Φ_Δ should preferably: (1) be endowed with high triplet quantum yields (Φ_T); (2) have long triplet state lifetimes (τ_T>1 μs) to facilitate their trapping by molecular oxygen and (3) show a triplet state of appropriate energy (E_T>95 kJ·mol^{-1}) to allow for efficient energy transfer to ground state molecular oxygen. Other desired photophysical properties are:[8] (4) high extinction coefficients in the spectral region of the light excitation and (5) high photostability.

According to the previous prerequisites nowadays we can find a large number of dye families capable of photosensitizing $^1O_2$ in high yields.[22] The main groups of molecular PS are: polynuclear aromatic hydrocarbons; aromatic ketones; aromatic heterocycles (coumarins, flavins, rose bengal, acridines, phenazines and phenothiazines); carbon nanoforms; coordination compounds of many transition metals, mainly Ru(II); and porphyrin and porphyrin derivatives (Figure 1.4).

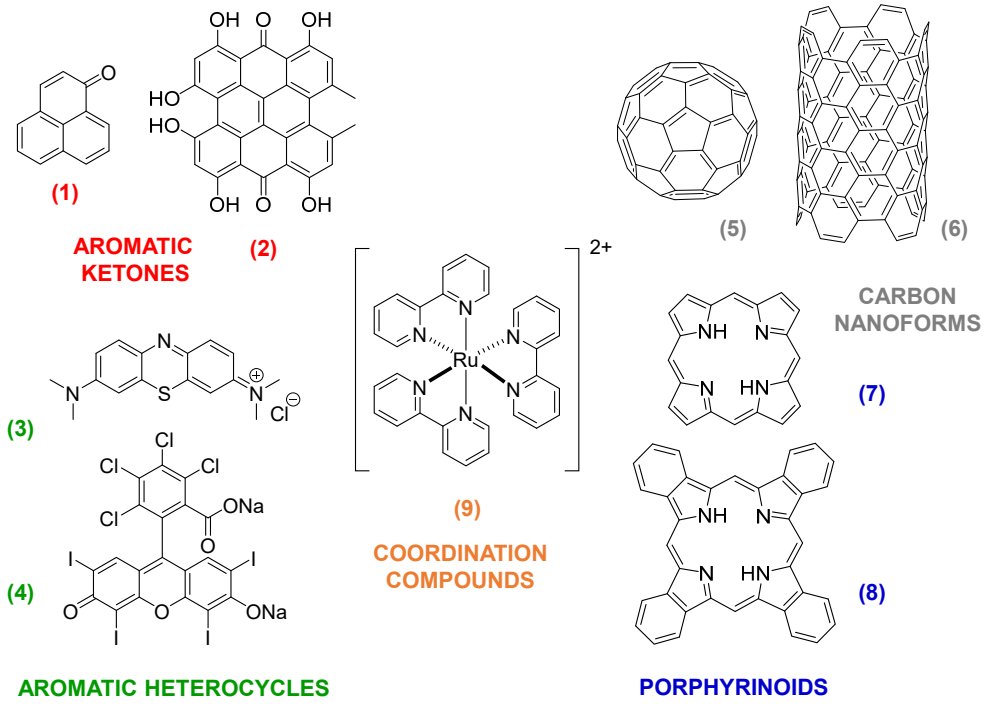

Figure 1.4. Structure of selected molecular PS: (1) phenalenone; (2) hypericin; (3) methylene blue; (4) rose Bengal; (5) fullerene – C_{60}; (6) single wall carbon nanotube; (7) porphyrin; (8) phthalocyanines and (9) tris(bipyridine)ruthenium(II).

Each particular type of PSs finds application in different areas basically depending on their photostability and their optical window. Among them all, the main family of approved PSs for phototherapeutic applications are porphyrins and porphyrin isomers. Porphyrins, also referred to as the pigments of life, are naturally occurring dyes that participate in many biological processes, including oxygen transport as constituents of haemoglobin or light harvesting in photosynthesis.[23] From a chemical point of view, porphyrins are heterocyclic macrocycles composed by four pyrrole subunits interconnected at their α carbons via methane bridges. The core macrocycle, named porphin, is aromatic and has 18-π conjugated electrons. The large aromatic conjugation of its core endows porphyrins with very intense absorption bands in the blue part of the spectrum and low absorption bands in the red. Thus, free-base porphyrins are generally deeply red or purple colored.

Monomeric porphyrins show characteristic absorption spectra with an intense absorption bands at about 400 nm (named B or Soret band) and a series of lower-intensity bands in the green-red spectral region (500-650 nm; Q bands). Free-base porphyrins are scarcely fluorescent (Φ_F<0.2) and have high intersystem crossing and triplet quantum yields. Moreover, they possess low-energy triplet excited states whose energy is really close to that of the $^1O_2 \leftarrow O_2$ transition (E_T≈150 kJ·mol^{-1}; E_Δ≈94 kJ·mol^{-1}) and their triplets are easily trapped by molecular oxygen before they decay ($f_{T,\Delta}^{O_2}$≈1). For example, tetraphenyl-porphyrin (TPP) has a Φ_F=0.10, Φ_T=0.73±0.1, $f_{T,\Delta}^{O_2}$=0.92±0.22 and Φ_Δ=0.67±0.14.[24]

Given their ubiquitous presence in biological systems and their promising photophysical and photosensitizing properties, porphyrins have been largely explored as PSs for the production of $^1O_2$, as well as other ROS, in biological media.[25,26] However, besides tremendous synthetic efforts to yield them pure and to introduce functionalities to render them water-soluble, the application of porphyrins into the clinics is still restricted. So far, only few porphyrin and porphyrin derivatives have been approved for medical applications (Table 1).

Table 1: Porphyrins and porphyrin prodrugs approved for therapeutic indications.

PS Name (Trade name)	Countries approved in (year of first approval)	Potential indications	Ref.
Haematoporphyrin derivative (Photofrin)	Canada (1993), Japan (1994), US (1995), Germany (1997), UK (1999), EU (2000), and 6 countries more	- Cervical, gastric and lung cancers - Basal cell carcinoma (BCC) and squamous cell carcinoma (SCC) - Endobronchial and esophageal cancers - Papillary bladder cancer - Barrett's esophagus	27–32
δ-Aminolevulinic acid HCl (Levulan, Alacare, Ameluz)	US (1999), EU-Sweden (2001), Austria (2009), Germany (2009) and others EU countries	Actinic keratosis (AK), BCC and, recently, esophageal dysplasia	28,29,31–35
Methyl aminolevulinate (Metvix)	EU (2001), Sweden (2001), US(2004), Canada (2009), Australia (2003), New Zealand (2004)	- BCC, AK, Bowen's disease	28,31–33
Hexaminolevulinate (Cysview or Hexvix)	EU (2006), US (2010),	- Colon and bladder cancer diagnosis, - Cervical intraepithelial neoplasia (CIN)	32,33,36

1.3.2. Limitations of the current molecular photosensitizers

Nowadays there is a vast number of molecular structures capable of photosensitizing the production of $^1O_2$ and other ROS. Rational design of molecular photosensitizers has allowed to achieve compounds with optimal photophysical and photochemical properties and currently several molecular structures can photosensitize the production of $^1O_2$ in yields proximal to 1, such as phenalenone or C_{60}. Notwithstanding with that fact, despite huge research efforts, only a relatively small number of PSs have received the approval so far.[7]

In fact, the translation of PS for clinical applications is limited since, apart from being excellent producers of $^1O_2$, other requisites are demanded to molecular PS. An ideal $^1O_2$ PS for phototherapeutic applications should pursue additional characteristics such as:[4,37] (1) be a pure compound and have good stability in storage; (2) be soluble in biological media (i.e. water); (3) have high extinction coefficients in the so called diagnostic or therapeutic window (approximately 600-800 nm); (4) have low levels of dark toxicity; (5) produce ROS in high yield; (6) be photostable; (7) selectively accumulate in the malignant cell or tissue and (8) show a relatively rapid clearance from healthy tissues.

Since standard molecular PS, particularly the ones clinically approved fail to fulfil one or more of the previous requirements there is an urgent need for the development of novel PSs and for the design of systems capable of enhancing the biological performance of the currently available molecular PSs.

The present thesis aims to improve the photosensitization of $^1O_2$ in biological *milieu* making it more effective for therapeutic applications. This objective has been pursued in two different directions: (a) the development of asymmetric porphycenes as a new family of molecular PS and (b) the use of the nano- and bio- technologies to enhance the performance of approved PS. This two topics are disclosed below.

1.4. Porphycenes

1.4.1. Structure and properties

The first family of porphyrin isomers ever synthetized were porphycenes. Porphycenes are aromatic 18π-electron porphyrin isomers consisting of two bipyrroles linked by ethylene bridges (Figure 1.5). They were first synthesized by Vogel *et al.* in 1986,[38] who named them as *porphycenes* since they combined the structural features of both porphyrin and acenes. Initial characterization of their physicochemical properties rapidly revealed that porphycenes are endowed with unique spectral, photophysical and redox properties as well as a rather different metal complexing ability. These features find application in multiple fields such as in PDT,[39–42] organic solar cells,[43–45] catalysis,[46,47] and theranostic applications.[48]

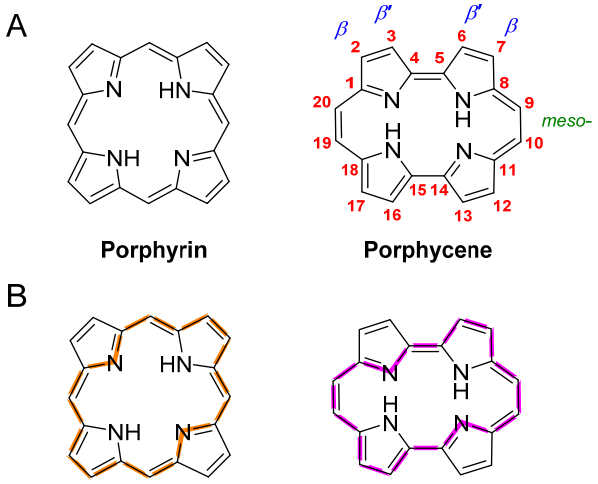

Figure 1.5. (A) Structure of porphyrin and porphycene; (B) schematic illustration of the electronic delocalization in the 18π-electron aromatic porphyrin and porphycene rings.

Both porphycenes and porphyrins are 18π-electron aromatic macrocycles. However, when comparing the molecular structure of the porphyrin *versus* the porphycene macrocycle, it becomes evident that the symmetry of the porphyrin macrocycle is lowered in their parent isomers (Figure 1.5). These modification in their electronic delocalization translates in an alteration of their photophysical properties. Porphycenes show two main different photophysical properties respect to porphyrins:

1. The electronic absorption spectra of porphycenes are reminiscent of those for porphyrins as two groups of bands (Soret and Q bands) can be observed, yet the probabilities of the spectroscopic transitions are very different, particularly in the Q region, in which porphycenes show **absorption coefficients one order of magnitude higher than porphyrins**.[49] In other words, porphycenes are endowed with approximately 10-fold higher molecular absorption coefficients in the diagnostic or therapeutic window.

2. Intersystem crossing (ISC) is reduced in porphycenes as compared to porphyrins. Therefore, **fluorescence quantum yields** of porphycenes are approximately 5 times **higher** than those of porphyrins.[49–51] Although this might seem a clear disadvantage as their photocytotoxicity is inevitably reduced, the higher fluorescence of porphycenes eases their location in biological tissues. Accordingly, porphycenes are better candidates for the so called phototheranostic applications, in which diagnostic and therapeutic abilities are combined in a single molecular entity.

The unique photophysical properties of both symmetric and asymmetric porphycenes make them very interesting photoactive molecules for biological applications. Porphycenes have been explored as potential candidates for PDT of cancer[39] and microbial infections.[40,52,53] Moreover, due to the abundant generation of reactive oxygen species (ROS) upon illumination, they have also been investigated for the treatment of other medical conditions such as psoriasis[54] and alterations of atherosclerotic plaque.[55]

1.4.2. Unusual properties of meso-substituted asymmetric porphycenes

From their discovery back in the late 1980s, the photophysical properties and photodynamic application of symmetric porphycene derivatives along with those of asymmetric porphycenes in the β,β-positions have been long explored.[56] In recent years, synthetic strategies for bringing asymmetry to porphycenes by functionalization of their *meso*-position have been developed (Figure 1.6), opening the way to an interesting class of porphycene derivatives: *meso*- or 9-susbtituted porphycenes.[57]

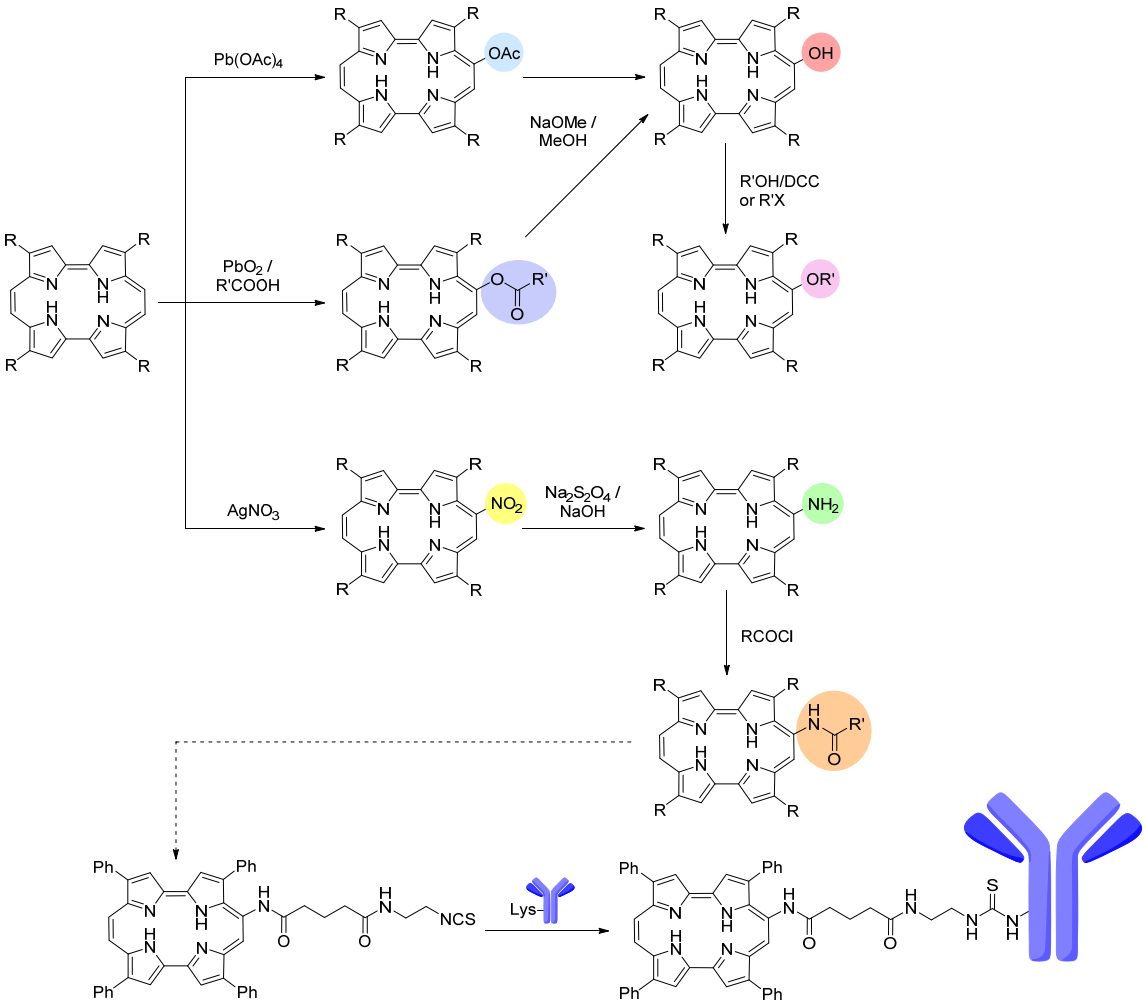

Figure 1.6. General strategies for the asymmetrization of porphycenes in the *meso*-position. Functionalization of porphycene with a residue bearing an ITC group has allowed its coupling to monoclonal antibodies.[55] Figure adapted from ref. 56.

Two main unusual properties should be highlighted about *meso*-substituted asymmetric porphycenes. First, the introduction of a single functionality in the *meso*- (9-) position of porphycenes breaks the symmetry of the macrocycle. As a result, the degeneracy of their different tautomers is lifted, thus rendering six different tautomers. These tautomers have been found to have different optical and photophysical properties. The most representative consequence of the symmetry break by the functionalization of the 9-position is the development of dual fluorescence emission, first observed for 9-amino-2,7,12,17-tetraphenylporphycene (9-ATPPo) and attributed to the existence of two different *trans*- tautomers.[58] Later studies on the photophysical properties of 9-substituted porphycene derivatives revealed that this was a rather more general phenomena affecting to other 9-amino substituted porphycene derivatives as well as other 9-subtituted compounds (Figure 1.7).[59] These studies revealed that the electronic properties of the different tautomers largely depend on the nature of the substituent at the *meso*

position. As a general trend, the higher the donor ability of the *meso* substituent, the higher the energy gap between the two *trans* tautomers.

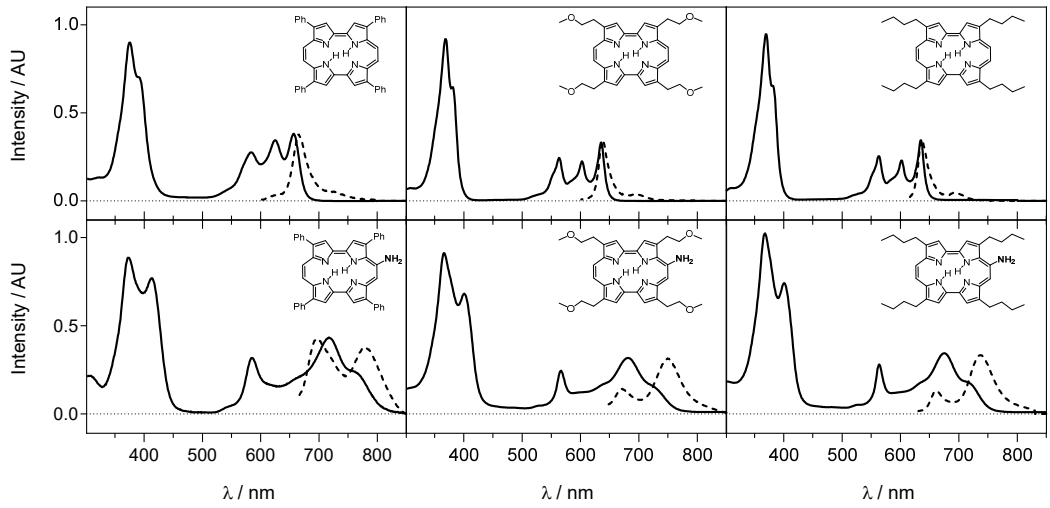

Figure 1.7. Absorption and fluorescence emission spectra of several 9-aminoporphycenes with different substituents in β compared to their parent unsubstituted porphycenes. Figure adapted from ref. 56.

Secondly, 9-substituted porphycenes offer new opportunities to conjugate the PS to nanoparticles or biologically relevant molecules. From a synthetic point of view, 9-hydroxy- and 9-amino- porphycenes can be prepared from the unsubstituted porphycene macrocycles in a two-step procedure (Figure 1.6).[57,60,61] These functionalities cannot directly react with biologically relevant molecules through click chemistry, but can be further functionalized with ester or amino groups bearing a reactive functionality. This strategy was pursued by Rosas *et al.* who developed a 9-glutaramido-2,7,12,17-tetraphenyl porphycene derivative bearing a terminal isothiocyanate (ITC) group.[55] This porphycene was conjugated to an ICAM-1 antibody through thiourea bonds, resultant from the reaction between the isothiocyanate group of the porphycene and the amines of the anti-ICAM-1 lysine residues. The conjugate was used to discriminate between surface changes in endothelial cells resulting from altered ICAM-1 expression thanks to the conjugate photocytotoxicity.

1.5. Enhanced production of singlet oxygen in the nano- and bio- era

The details of $^1O_2$ photosensitization by organic dyes are well understood as well as their limitations (see section 1.2 and 1.3). In addition to the development of new and improved molecular PSs, such as porphycenes, recent advances in fields as diverse as nanotechnology and bioengineering offer new opportunities to address some of the main current challenges in the $^1O_2$ field. Nanoparticles and biomolecules can provide new opportunities to the generation of $^1O_2$ in biological media as (1) superior spatiotemporal control on the photosensitization of $^1O_2$ thanks to their targeting capabilities, (2) become new photosensitizing materials with optical and photophysical properties that can outperform those of current organic PSs or (3) enhance the photophysical properties of molecular photosensitizers through nanoantenna effects. Reader will find herewith an overview of 3 different bio- and nano- approaches to improve the photosensitization of $^1O_2$ in biological media. Further information can be found in the literature.[7,62]

1.5.1. Protein-bound photosensitizers: photoimmunotherapy

Antibodies and antibody fragments have gained importance as active agents for cancer treatment and as vectors for the delivery of other anticancer drugs. For instance, two bioconjugates, brentuximab vedotin (Adcetris®) and trastuzumab emtansine (Kadcyla®), comprising a monoclonal antibody (mAb) and a chemotherapeutic drug have recently been approved by the regulatory agencies and some others are in phases II/III.[63] The PDT-community has also turned his attention to the use of mAb and/or antibody fragments for the development of photoimmunoconjugates (PICs) with improved PDT selectivity and efficiency. This new modality of cancer treatment is referred to as photoimmunoterapy (PIT) and its potential relies on the fact that mAb and their fragments can selectively bind to certain antigens overexpressed in cancer tissue or neovasculature, thus conveying the PS to the desired target cell.[64–67] This approach shows enormous potential for PDT applications since ROS damage, highly unspecific *per se*, would be confined within the target cell or tissue by an appropriate PIC.

Bioconjugation strategies: Antibodies and immune-fragments express certain residues, e.g., amino acids and oligosaccharides, that allow for covalent binding with conveniently functionalized PSs. A successful PIC must retain or ideally enhance the photophysical properties of the PS while preserving the immunoreactivity profile of the antibody. To achieve such convenient antibody-PS conjugation two different strategies, indirect and direct, can be performed. The indirect approach implies preconjugation of the PSs to polymeric scaffolds such as dextran, polylysine, polyethylene glycol, or polyglutamic acid, which act as spacers between

the PS and the antibody, precluding both the loss of immunoactivity and the aggregation of the PS.[68] The direct conjugation approach uses a PS conveniently modified with a highly reactive functionality that selectively reacts with certain residues of the protein, namely cysteines for maleimide modified PSs, and lysines for *N*-hydroxysuccinimide (NHS) activated esters as well as isothiocyanates (ITC) (Figure 1.8).[69]

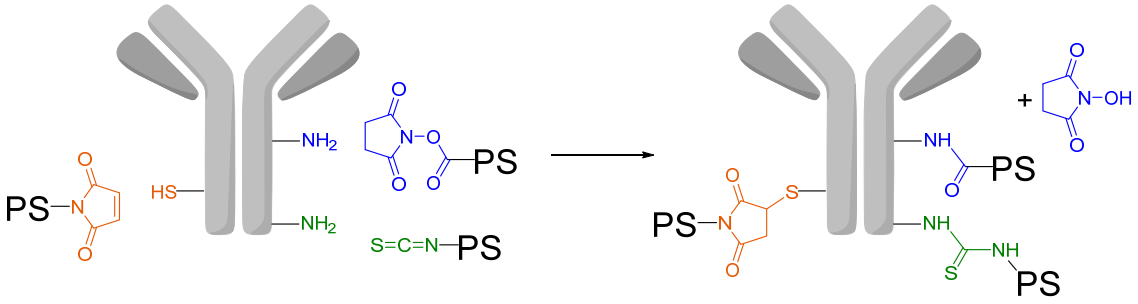

Figure 1.8. Maleimide, NHS and ITC bioconjugation strategies for the labeling of monoclonal antibodies with $^1O_2$ PSs.

PS conjugation to lysine residues using the ITC group occurs via an addition reaction yielding a thiourea bridge, thereby preventing the generation of by-products that could potentially contaminate the conjugate. This is a distinct advantage relative to the use of NHS-activated esters, which release the activating hydroxysuccinimide group.[70] Additionally, PS-ITCs are stable under regular storage conditions and their conjugation does not require supplementary activating reagents, allowing the bioconjugation to take place under mild conditions.[68,69] Several examples of PICs that used ITC chemistry for conjugation have been reported encompassing the majority of PS families.[55,71–74] As a general trend, given that the newly-formed thiourea bridge is non-conjugated with the chromophore, no-significant changes on the optical and fluorescent properties of the PSs are to be expected upon conjugation.

Early conjugates: With the aim of improving the solubility of hematoporphyrin and its targeting efficiency *versus* cancerous cells, Mew *et al.* reported in 1983 the first application of a PIC for the treatment of animal tumours.[64] Since this very first report, the synthesis of PICs has broadened leading to numerous publications in the field and a few patented bioconjugates, both varying the type of antibody and the PS used. These early efforts were limited to conjugation to mAbs and encountered several difficulties, mainly due to the tendency of the PIC to aggregate in aqueous saline buffers and of the hydrophobic PS to stick to the hydrophobic pockets of the mAb *via* non-covalent interactions.[73,75] Furthermore, conjugation of the antibodies to some PS with several functional groups, such as hematoporphyrin or chlorin e6, were found to result in cross-linking with the subsequent loss of the mAb specificity and of the PS activity.[69,76,77]

In order to overcome these limitations, several alternatives have been proposed over the years including: (i) enhancing the solubilization of the mAb and/or the PS adding small amounts of an organic solvent such as dimethylsulphoxide;[73,75,78] (ii) enhancing the stability of the PICs by attaching hydrophilic polymer chains to the antibody;[78,79] and (iii) enhancing the aqueous solubility of the PS by making it more hydrophilic and, even more preferably, cationic.[80]

Recent trends: Although mAb allow for a high degree of labelling since they contain several lysine residues available for bioconjugation, coupling of a large number of PS molecules to whole antibodies often impairs the antibody targeting ability and reduces the solubility of the PIC. Moreover, solid tumours have poor vascularisation, limiting the diffusion of the 150 kDa mAb PICs and enlarging its serum half-life. A growing approach to overcome the time needed for their tumour accumulation and the clearance of the unbound conjugates, is the use of smaller antibody fragments for bioconjugation, such as antigen-binding fragments ($F'(ab)_2$, ~100 kDa),[81] small immune proteins (SIP),[82] single-chain variable fragments (scFv, ~25 kDa)[83,84] and nanobodies (NB, ~15 kDa).[85] The lower the size of the antibody fragments, the higher blood clearance and faster tumour accumulation. This allows for a reduction in the time interval between the injection of the PIC and light exposure and upholds great promises in the clinical translation of PIT.[86]

A second trend in the development of PIT is the use of NIR dyes, for instance the phthalocyanine IRDye 700DX.[65,87–90] Photochemical studies on its PICs have recently shown that both type I and type II mechanisms take place upon light exposure, making its application oxygen dependent.[91] Moreover, the development of NIR dyes has been encompassed with the introduction of standardized LED light sources for PIT applications.[92]

Finally, an emergent approach in PIT is its combination with other therapeutic strategies such as nanoparticle-based delivery of drugs. It has been observed that PIT treatment primarily results in killing of perivascular tumour cells, thus increasing the leakage into the extravascular space. As a result, the delivery of nanosized systems into cancerous cells can be increased up to 20-times in a new therapeutic strategy referred to as super enhanced permeability and retention effect.[93,94]

1.5.2. Nanoparticle-bound photosensitizers

As presented above, one of the main challenges facing the clinical application of PDT nowadays is the improvement in its selectivity; in other words, the specific delivery of the PSs to the malignant cells, while sparing the healthy ones. Indeed, antibody and antibody-fragments are a solution to this problem. However, their cargo is generally limited to few (1-5) molecules of PS *per* antibody.[68] Nanoparticles offer an enriched strategy to address the selectivity of the PSs while

allowing high loading of PS. Nanoparticles can be thus conceived as nano-sized supports that allow:

1. high loading of molecular PSs in a nanocompartment,[95]
2. enhanced permeability and retention effects to malignant cells (passive targeting),[96]
3. further functionalization with targeting vectors for enhanced selectivity (active targeting).[97]

Attending to the PS organization relative to the nanoparticle structure, two types of nanoparticles can be distinguished: (1) nanostructures into which the PS is encapsulated and from which it is released into the target cells, such as liposomes, micelles and polymer based nanoparticles[98,99] or (2) nanoparticles possessing a three-dimensional rigid matrix with the PS located on their surface, such as silica[100] or metal nanoparticles.[101] In this thesis we have investigated the second kind of nanoparticles, both using a covalent binding of the PS to the external surface or an electrostatic binding.

A particularity of the attachment of the PS onto the nanoparticle surface is that molecular oxygen has to diffuse through the nanoparticle surface and that $^1O_2$ must be released from that location. Thus, several different aspects should be considered when designing nanoparticle-bound photosensitizers:[102]

1. **Accessibility of molecular oxygen to the PS:** the nanoparticles' matrix should be porous enough to be permeable to molecular oxygen so that it can reach the PS.
2. **Aggregation of the molecular PS:** [103] Most molecular PS are of hydrophobic nature and tend to aggregate when bound to nanostructures. Generally it is desirable to reduce such aggregation in order to enhance the photophysical performance of the PSs. Thus it is crucial to carefully control the amount of PS linked or adsorbed onto the nanoparticle surface in order to avoid stacking of the PS that would lead to a decrease of $^1O_2$ photosensitization.
3. **Photobleaching of the PS:** Since nanoparticles concentrate a high number of molecular PS in a reduced location it may occur that $^1O_2$ reacts with the PS itself, leading to photobleaching.
4. **Presence of quenching moieties:**[103] Once produced, $^1O_2$ may be quenched by the nanoparticle itself or by certain surface agents before being able to reach targeted cells. $^1O_2$ should be able to diffuse out the nanoparticle surface in order to achieve successful tissue damage.

5. **Location of the nanostructure relative to the cell:**[103] As discussed above, $^1O_2$ has to diffuse out of the nanoparticle surface and reach the targeted substrate. Given that $^1O_2$ diffusion in biological media is limited, the nanoparticle should be located close to the targeted substrate to achieve significant cell damage.

1.5.3. Plasmonic photosensitizers

The last decade has witnessed the birth and exponential growth of the science of nanoplasmonics, whereby the unique plasmonic features of metal nanoparticles (MNPs) have led to an ever-growing number of novel applications such as metal-enhanced spectroscopy. These new techniques rely on the unique ability of metal nanoparticles to both enhance the electromagnetic radiation on their surface (localized field enhancement)[104,105] and to conduct energy transfer from excited states to metal nanoparticles.[106,107] Thanks to the exploitation of the plasmonic effect, researchers have been able to enhance the fluorescence and phosphorescence of organic dyes in the so-called metal enhanced fluorescence[106,108] and phosphorescence phenomena.[107] Moreover, the localized field enhancement at the nanoparticle surface has been exploited to develop novel supports to enhance the Raman scattering signals of different substrates resulting in the inception of surface-enhanced Raman spectroscopy (SERS).[109] Rational improvement of SERS has allowed to achieve enhancements factors as much as 10^{10} to 10^{11}, permitting the detection at a single molecule level.[110]

In the $^1O_2$ field, the previous properties have allowed to increase the $^1O_2$ production quantum yield of conventional PSs,[111,112] and also to ease the detection of its luminescence by enhancing the radiative rate constant.[112,113] All-together, these findings have given rise to the development of **plasmonic photosensitizers of $^1O_2$**, which were first developed as solid supports and are nowadays moving to solution state.

Depending on the radiative transition that is boosted using MNPs, two designs of plasmonic photosensitizers of $^1O_2$ can be considered: MNPs aimed at enhancing either **(1) the production** or **(2) the radiative decay** of $^1O_2$ (Figure 1.9). Geddes *et al.* reported for the first time a 3-fold enhanced production of $^1O_2$ by rose bengal in the presence of silver island films (SIFs).[111] In turn, Toftegaard e*t al.* were the first to report an enhancement of the $^1O_2$ radiative constant by combining tetraphenylporphyrin with gold nanodiscs whose plasmon band matched the $^1O_2$ emission spectrum at 1270 nm.[113] Ragàs *et al.* studied the emission of $^1O_2$ photosensitized by C_{60} in the presence of the silver island films and measured a phosphorescence enhancement of 32, which resulted from enhancement of both the production and the radiative decay of $^1O_2$.[112] A

major factor limiting the enhancement of $^1O_2$ emission is its fast diffusion from the metal surface after its production.

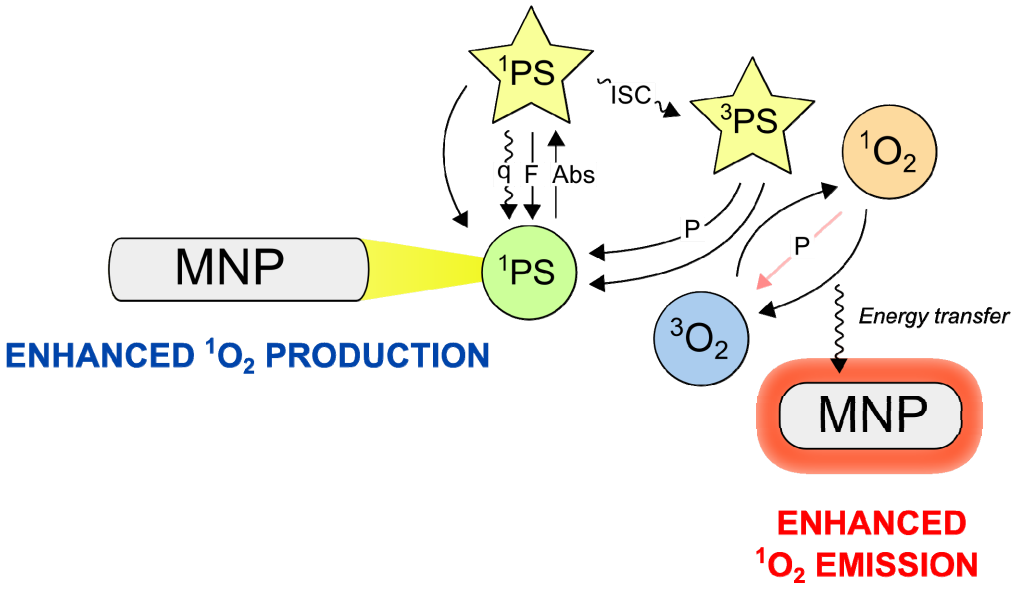

Figure 1.9. Illustration of the strategies for the design of plasmonic PS of $^1O_2$; where Abs: absorption; F: fluorescence; P: phosphorescence; q: non-radiative decays; ISC: intersystem crossing. Figure adapted from ref. 62.

As the enhanced generation of $^1O_2$ on solid supports was confirmed and improved, the attention of the $^1O_2$ community moved to the development of plasmonic photosensitizers of $^1O_2$ in solution. Several reports about $^1O_2$ enhancement in solution have been published revealing a wide range of nanostructures capable of increasing the production of $^1O_2$ in solution. Gold nanostructures/PpIX[114,115] and silver nanoparticles/RB[116,117] are the most studied *tandems* for $^1O_2$ production enhancement.

When developing plasmonic nanostructures, either those capable of enhancing the fluorescence or the phosphorescence of organic and inorganic emitters, the distance between the metallic core and the luminophore is of great importance.[118–121] At very short distances between the nanoparticle core and the emitter, efficient quenching of molecular transitions by nanoparticles takes place as MNPs act as a radiative quencher. On the other hand, MNPs have no influence on their surrounding at very long distances. But at intermediate distances, plasmon-dipole interaction between the plasmonic nanoparticles and the nearby molecules results in high an enhancement of either their excitation or they radiative decay rate, which ultimately translate into higher emission quantum yields. The exact distance profile for emission enhancement vary depending on the transition affected (fluorescence or phosphorescence) and the luminophore/nanoparticle nature. However, for the vast majority of emitters it is reasonably

accepted that the strongest enhancement are achieved when molecules are located within 5-15 nm from the plasmonic structure.[118–121]

Although the enhancement of $^1O_2$ had been described previously, prior to the development of this thesis, no single nanostructure had been reported to be capable of enhancing the $^1O_2$ radiative rate constant in biological media. Moreover, no reports of any distance effects had been disclosed, pointing to the necessity of further rationalizing this phenomena for $^1O_2$ using well defined nanostructures.

1.6. Objectives

The main goal of this thesis is to improve the photosensitization of $^1O_2$ in biological media using the new opportunities of the nano- and bio- era. This main goal can be further set in the following specific objectives:

- Development of conjugation strategies for the labelling of proteins and nanoparticles with porphycenes.
- Study of the nanoparticle morphology effects on the $^1O_2$ photosensitization by silica-bound photosensitizers.
- Investigation of the ability of plasmonic metal nanoparticles to enhance the production and radiative decay of $^1O_2$ in biological media.

1.7. Publications derived from the thesis

Investigation of the prior objectives has led so far to a total of five papers in peer-reviewed journals, one patent application, five book chapters and three communications in international congresses.

Papers

- *Zampini, G.; **Planas, O.**; Marmottini, F.; Gulías, O.; Agut, M.; Nonell, S.; Latterini, L. Morphology effects on singlet oxygen production and bacterial photoinactivation efficiency by different silica-Protoporphyrin IX nanocomposites. *RSC Adv.*, 2017, 7, 14422-14429. DOI: 10.1039/ c7ra00784a.
- ***Planas, O.**; Macia, N.; Agut, M.; Nonell, S.; Heyne, B. Distance-Dependent Plasmon-Enhanced Singlet Oxygen Production and Emission for Bacterial Inactivation. *J. Am. Chem. Soc.*, 2016, 138, 2762-2768. DOI: 10.1021/jacs.5b12704.
- ***Planas, O.**; Gallavardin, T.; Nonell, S.; A novel fluoro-chromogenic click reaction for the labelling of proteins and nanoparticles with near-IR theranostic agents. *Chem. Commun.*, 2015, 51, 5586-5589. DOI: 10.1039/c4cc09070e.
- **Planas, O.**; Bresolí-Obach, R.; Nos, J.; Gallavardin, T.; Ruiz-Gonzalez, R.; Agut, M.; Nonell, S.; Synthesis, photophysical characterization and photoinduced antibacterial activity of methylene blue-loaded amino- and mannose-targeted mesoporous silica nanoparticles. *Molecules*, 2015, 20, 6284-6298. DOI:10.3390/molecules20046284
- **Planas, O.**; Tejedor-Estrada, R.; Nonell, S.; Tautomerism and dual fluorescence in 9-substituted n-propyl- and methoxyethyl- porphycenes. *J. Porphyrins Phthalocyanines* 2012, 16, 633-640. DOI: 10.1142/S1088424612500526

Patent applications

- **Planas, O.**; Gallavardin, T.; Nonell, S.; *Near-infrared fluorogenic porphycene derivatives as fluorescent labels for photodiagnosis and phototherapeutic use*. Application number: PCT/EP2015/063907 and publication number WO/2015/197510.

Book Chapters

- Hally, C.; Rodríguez-Amigo, B.; Bresolí-Obach, R.; **Planas, O.**; Nos, J.; Boix-Garriga, E.; Ruiz-González R.; Nonell, S.; *Photodynamic Therapy.* In Theranostics and Image Guided Drug Delivery; Thanou, A. Ed.; Royal Society of Chemistry: Cambridge, 2017. ISBN: 978-178-2624-66-0. Accepted

- **Planas, O.**; Gallavardin, T.; Nonell, S.; Chapter 4: *Unusual Properties of Asymmetric Porphycenes.* In Handbook of Porphyrin Science, Volume 41; Guilard, R.; Smith, K. M.; Kadish K. M. Eds.; World Scientific, 2016,41, 299-349. ISBN: 978-981-3143-52-4.
- Rodriguez-Amigo, B.; **Planas, O**; Torra, J; Bresolí-Obach, R.; Ruiz-González, R.; Nonell, S.; Chapter 2: *Photosensitisers for Photodynamic Therapy: State of the Art and Perspectives.* In Photodynamic Medicine: From Bench to Clinic; Kostron, H.; Hasan, T., Eds.; Royal Society of Chemistry, 2016, 1, 23-62. ISBN: 978-1-78262-451-6.
- Boix-Garriga, E.; Rodriguez-Amigo, **Planas, O.**; Nonell S.; Chapter 2: *Properties of Singlet Oxygen.* In Singlet Oxygen: Applications in Biosciences and Nanosciences, Volume 1; Flors C..; Nonell, S., Eds. Royal Society of Chemistry, 2016, 1, 23-46. ISBN: 978-1-78262-038 -9.
- **Planas, O.**; Boix-Garriga, E.; Rodriguez-Amigo, B.; Torra, J.; Bresolí-Obach, R.; Flors, C.; Viappiani, C.; Agut, M.; Ruiz-González, R.; Nonell S.; Chapter 9: *Newest approaches to singlet oxygen photosensitisation in biological media.* In Photochemistry: Volume 42; Fasani, E.; Albini, A., Eds.; Photochemistry; Royal Society of Chemistry, 2015, 42, 233-278. ISBN: 978-1-84973-956-6.

Communications in international congresses

- **Planas, O.**; Rodriguez-Amigo, B.; Tabero, A; Lázaro-Carrillo, A.; Mora, M.; Sagristà MªLl.; Villanueva, A.; Agut, M.; Nonell S.; *Porphyrinoid based bio- and nanodevices for theranostic applications.* 9th International Conference on Porphyrins and Phthalocyanines (ICPP-9), Nanjing (China), September 3-8, 2016.
- **Planas, O.**; Hally, C.; Gallavardin, T.; Agut, M.; Nonell S.; *Porphycene-ITCs for photo-theranostic applications.* 16th Congress of the European Society for Photobiology, Aveiro (Italia), August 31 – September 4, 2015.
- **Planas, O.**; Gallavardin, T.; Nonell S.; *Porphycenes for theranostic applications.* 25th IUPAC Symposium on Photochemistry, Bordeaux (France), 13-18 July, 2015.

Additional papers are at different stages of publication.

- **Planas, O.**; Fernández-Llaneza, D.; Nieves, I.; Ruiz-González, R.; Lemp, E.; Zanocco, A.; Nonell, S.; Acid- and *hydrogen*-bonding-induced switching between 22-π and 18-π electron conjugation in 2-aminothiazolo[4,5-c]porphycenes. Manuscript submitted to ***Phys. Chem. Chem. Phys.***
- **Planas, O.**; Feliu, N.; Chakraborty, I.; Nieves, I.; Nonell, S.; Parak, W. Time-dependent photocytotoxicity of Short-Chain PEG protected gold nanoclusters. Manuscript in preparation.

- Chakraborty, I.; **Planas, O.**; Feliu, N.; Nonell, S.; Parak, W. Synthesis, Photophysical Properties and Toxicity of Noble Metal Nanoclusters. Perspective for APL Materials in preparation.

In fulfillment of the regulations of the PhD program in Chemistry and Chemical Engineering of the *Universitat Ramon Llull*, only the papers marked with a * have been included in the thesis (chapter 2).

Given that all of the included papers for the evaluation have several authors, the specific contribution of the PhD candidate Oriol Planas to each publication is detailed below (listed in the order of the text):

1. **Planas, O.**; Gallavardin, T.; Nonell, S.; A novel fluoro-chromogenic click reaction for the labelling of proteins and nanoparticles with near-IR theranostic agents. *Chem. Commun.*, 2015, 51, 5586-5589. DOI: 10.1039/c4cc09070e.

Oriol Planas has participated in the design of the work, helped synthesize the 2-aminothiazolo[4,5-c]porphycenes, prepared the nano- and bioconjugates, characterized their physico-chemical, photophysical and photosensitizing properties, unraveled the ring expansion mechanism, explored the scope of the novel fluoro- and chromogenic reaction, participated in data analysis and discussion, prepared the first draft of the paper and participated in its critical revision and final approval.

2. Zampini, G.; **Planas, O.**; Marmottini, F.; Gulías, O.; Agut, M.; Nonell, S.; Latterini, L. Morphology effects on singlet oxygen production and bacterial photoinactivation efficiency by different silica-Protoporphyrin IX nanocomposites. *RSC Adv.*, 2017, 7, 14422-14429. DOI: 10.1039/ c7ra00784a.

Oriol Planas has participated in the design of the work, characterized the physico-chemical, photophysical and photosensitizing properties of the protoporphyrin IX-silica nanoconjugates, explored the effect of the pore size of the nanomaterials on the singlet oxygen production efficiency and kinetics, assisted in the assessment of the biological activity of the nanoconjugates in microbial samples, participated in data analysis and discussion, participated in the preparation of the first draft of the paper and participated in its critical revision and final approval.

3. **Planas, O.**; Macia, N.; Agut, M.; Nonell, S.; Heyne, B. Distance-Dependent Plasmon-Enhanced Singlet Oxygen Production and Emission for Bacterial Inactivation. *J. Am. Chem. Soc.*, 2016, 138, 2762-2768. DOI: 10.1021/jacs.5b12704.

Oriol Planas has participated in the design and conception of the nanoplatform presented in this paper based on his prior-experience in numerous attempts to achieve the plasmonic enhancement of $^1O_2$. Mr. Planas characterized the physico-chemical, photophysical and photosensitizing properties of the rose bengal-silica/silver nanoconjugates, explored the effect of distance between the PS and the metal core on the $^1O_2$ production efficiency and radiative decay, studied the photocytotoxicity of the nanoconjugates in microbial samples, characterized the enhancement of the $^1O_2$ production and emission in those samples, participated in data analysis and discussion, participated in the preparation of the first draft of the paper and participated in its critical revision and final approval.

1.8. References

(1) Boix-Garriga, E.; Rodríguez-Amigo, B.; Planas, O.; Nonell, S. In *Singlet Oxygen: Applications in Biosciences and Nanosciences*; Nonell, S., Flors, C., Eds.; Royal Society of Chemistry, 2016; pp 23–46.

(2) Walling, C. In *Active Oxygen in Chemistry*; S. Foote, C., Selverstone Valentine, J., Greenberg, A., F. Liebman, J., Eds.; Springer Science+Business Media, Inc., 1995; pp 24–65.

(3) Crounse, J. D.; Nielsen, L. B.; Jørgensen, S.; Kjaergaard, H. G.; Wennberg, P. O. *J. Phys. Chem. Lett.* **2013**, *4* (20), 3513.

(4) Agostinis, P.; Berg, K.; Cengel, K. A.; Foster, T. H.; Girotti, A. W.; Gollnick, S. O.; Hahn, S. M.; Hamblin, M. R.; Juzeniene, A.; Kessel, D.; Korbelik, M.; Moan, J.; Mroz, P.; Nowis, D.; Piette, J.; Wilson, B. C.; Golab, J. *CA. Cancer J. Clin.* **2011**, *61* (4), 250.

(5) Obaid, G.; Broekgaarden, M.; Bulin, A.-L.; Huang, H.-C.; Kuriakose, J.; Liu, J.; Hasan, T. *Nanoscale* **2016**, *8* (25), 12471.

(6) Wainwright, M.; Maisch, T.; Nonell, S.; Plaetzer, K.; Almeida, A.; Tegos, G. P.; Hamblin, M. R. *Lancet Infect. Dis.* **2017**, *17* (2), 49.

(7) Rodríguez-Amigo, B.; Planas, O.; Bresolí-Obach, R.; Torra, J.; Ruiz-González, R.; Nonell, S. In *Photodynamic Mediucine:From Bench to Clinic*; Kostron, H., Hasan, T., Eds.; The Royal Society of Chemistry, 2016; pp 23–62.

(8) DeRosa, M. C.; Crutchley, R. J. *Coord. Chem. Rev.* **2002**, *233–234*, 351.

(9) Kanofsky, J. R. In *Singlet Oxygen: Applications in Biosciences and Nanosciences*; Nonell, S., Flors, C., Eds.; Royal Society of Chemistry, 2016; pp 93–103.

(10) Schweitzer, C.; Schmidt, R. *Chem. Rev.* **2003**, *103* (5), 1685.

(11) Moore, D. E. *Mutat. Res. Mol. Mech. Mutagen.* **1998**, *422* (1), 165.

(12) Foote, C. S.; Chang, Y. C.; Denny, R. W. *J. Am. Chem. Soc.* **1970**, *249* (6), 5218.

(13) Foote, C. S.; Chang, Y. C.; Denny, R. W. *J. Am. Chem. Soc.* **1970**, *92* (17), 5216.

(14) Conn, P. F.; Schalch, W.; Truscott, T. G. *J. Photochem. Photobiol., B* **1991**, *11* (1), 41.

(15) Bohm, F.; Haley, J.; Truscott, T. G.; Schalch, W. *J. Photochem. Photobiol. Biol.* **1993**, *21* (2–3), 219.

(16) Yamakoshi, Y.; Umezawa, N.; Ryu, A.; Arakane, K.; Miyata, N.; Goda, Y.; Masumizu, T.; Nagano, T. *J. Am. Chem. Soc.* **2003**, *125* (42), 12803.

(17) Huang, L.; St. Denis, T. G.; Xuan, Y.; Huang, Y.-Y.; Tanaka, M.; Zadlo, A.; Sarna, T.; Hamblin, M. R. *Free Radic. Biol. Med.* **2012**, *53* (11), 2062.

(18) Kasimova, K. R.; Sadasivam, M.; Landi, G.; Sarna, T.; Hamblin, M. R. *Photochem. Photobiol. Sci.* **2014**, *13* (11), 1541.

(19) Zhang, Y.; Dai, T.; Wang, M.; Vecchio, D.; Chiang, L. Y.; Hamblin, M. R. *Nanomedicine* **2015**, *10* (4), 603.

(20) Wu, X.; Huang, Y.-Y.; Kushida, Y.; Bhayana, B.; Hamblin, M. R. *Free Radic. Biol. Med.* **2016**, *95*, 74.

(21) Nonell, S.; Flors, C. In *Singlet Oxygen: Applications in Biosciences and Nanosciences*; Nonell, S., Flors, C., Eds.; Royal Society of Chemistry, 2016; pp 7–26.

(22) Fresnadillo, D. G.; Lacombe, S. In *Singlet Oxygen: Applications in Biosciences and Nanosciences*; Nonell, S., Flors, C., Eds.; Royal Society of Chemistry, 2016; pp 105–143.

(23) Battersby, A. R. *Nat. Prod. Rep.* **2000**, *17* (6), 507.

(24) Pineiro, M.; Carvalho, A. L.; Pereira, M. M.; Gonsalves, A. M. d'A. R.; Arnaut, L. G.; Formosinho, S. J. *Chem. Eur. J.* **1998**, *4* (11), 2299.

(25) Bonnett, R. *Chem. Soc. Rev.* **1995**, *24* (1), 19.

(26) Ethirajan, M.; Chen, Y.; Joshi, P.; Pandey, R. K. *Chem. Soc. Rev.* **2011**, *40* (1), 340.

(27) Dąbrowski, J. M.; Arnaut, L. G. *Photochem. Photobiol. Sci.* **2015**, *14* (10), 1765.

(28) Ormond, A. B.; Freeman, H. S. *Materials (Basel).* **2013**, *6* (3), 817.

(29) Zheng Huang, M.D. *Technol. Cancer Res. Treat.* **2005**, *4* (3), 283.

(30) Usuda, J.; Kato, H.; Okunaka, T.; Furukawa, K.; Yamada, K.; Suga, Y.; Honda, H.; Nagatsuka, Y.; Ohira, T.; Tsuboi, M.; Hirano, T. *J. Thorac. Oncol.* **2006**, *1* (5), 6.

(31) Josefsen, L. B.; Boyle, R. W. *Met. Based. Drugs* **2007**, *2008*, 1.

(32) Lucky, S. S.; Soo, K. C.; Zhang, Y. *Chem. Rev.* **2015**, *115* (4), 1990.

(33) Wachowska, M.; Muchowicz, A.; Firczuk, M.; Gabrysiak, M.; Winiarska, M.; Wańczyk, M.; Bojarczuk, K.; Golab, J. *Molecules* **2011**, *16* (12), 4140.

(34) Medicines and Healthcare products Regulatory Agency. Public Assessment Report: Alacare 8 mg Medicated Plaster https://www.gov.uk/government/organisations/medicines-and-healthcare-products-regulatory-agency. (10-04-2016)

(35) European Medicines Agency. Summary of product characteristics: Ameluz http://www.ema.europa.eu/ema/. (10-04-2016)

(36) Dolmans, D. E. J. G. J.; Fukumura, D.; Jain, R. K. *Nat Rev Cancer* **2003**, *3* (5), 380.

(37) Castano, A. P.; Demidova, T. N.; Hamblin, M. R. *Photodiagnosis Photodyn. Ther.* **2004**, *1* (4), 279.

(38) Vogel, E.; Köcher, M.; Schmickler, H.; Lex, J. *Angew. Chemie Int. Ed.* **1986**, *25* (3), 257.

(39) Stockert, J. C.; Cañete, M.; Juarranz, A.; Villanueva, A.; Horobin, R. W.; Borrell, J. I.; Teixido, J.; Nonell, S. *Curr. Med. Chem.* **2007**, *14* (9), 997.

(40) Ragàs, X.; Sánchez-García, D.; Ruiz-González, R.; Dai, T.; Agut, M.; Hamblin, M. R.; Nonell, S. *J. Med. Chem.* **2010**, *53* (21), 7796.

(41) García-Díaz, M.; Sánchez-García, D.; Soriano, J.; Sagristà, M. L.; Mora, M.; Villanueva, Á.; Stockert, J. C.; Cañete, M.; Nonell, S. *Med. ChemComm* **2011**, *2* (7), 616.

(42) Ruiz-González, R.; Acedo, P.; Sánchez-García, D.; Nonell, S.; Cañete, M.; Stockert, J. C.; Villanueva, A. *Eur. J. Med. Chem.* **2013**, *63*, 401.

(43) Costa, R. D.; Malig, J.; Brenner, W.; Jux, N.; Guldi, D. M. *Adv. Mater.* **2013**, *25* (18), 2600.

(44) Brenner, W.; Malig, J.; Costa, R. D.; Guldi, D. M.; Jux, N. *Adv. Mater.* **2013**, *25* (16), 2314.

(45) Feihl, S.; Costa, R. D.; Brenner, W.; Margraf, J. T.; Casillas, R.; Langmar, O.; Browa, A.; Shubina, T. E.; Clark, T.; Jux, N.; Guldi, D. M. *Chem. Commun.* **2014**, *50* (77), 11339.

(46) Maeda, D.; Shimakoshi, H.; Abe, M.; Hisaeda, Y. *Dalt. Trans.* **2009**, No. 1, 140.

(47) Oohora, K.; Kihira, Y.; Mizohata, E.; Inoue, T.; Hayashi, T. *J. Am. Chem. Soc.* **2013**, *135* (46), 17282.

(48) Planas, O.; Gallavardin, T.; Nonell, S. *Chem. Commun.* **2015**, *51* (26), 5586.

(49) Rubio, N.; Prat, F.; Bou, N.; Borrell, J. I.; Teixido, J.; Villanueva, A.; Juarranz, A.; Canete, M.; Stockert, J. C.; Nonell, S. *New J. Chem.* **2005**, *29*, (2) 378.

(50) Aramendia, P. F.; Redmond, R. W.; Braslavsky, S. E.; Schaffnerlf, K.; Vogel, E.; Nonell, S. *Photochem. Photobiol.* **1986**, *44* (5), 555.

(51) Braslavsky, S. E.; Müller, M.; Mártire, D. O.; Pörting, S.; Bertolotti, S. G.; Chakravorti, S.; Koç-Weier, G.; Knipp, B.; Schaffner, K. *J. Photochem. Photobiol. B* **1997**, *40* (3), 191.

(52) Polo, L.; Segalla, A.; Bertoloni, G.; Jori, G.; Schaffner, K.; Reddi, E. *J. Photochem. Photobiol. B Biol.* **2000**, *59* (1–3), 152.

(53) Ruiz-González, R.; Agut, M.; Reddi, E.; Nonell, S. *Int. J. Mol. Sci.* **2015**, *16* (11), 27072.

(54) Karrer, S.; Abels, C.; Bäumler, W.; Ebert, A.; Landthaler, M.; Szeimies, R.-M. *J. Invest. Dermatol.* **1996**, *107* (3), 466.

(55) Rosàs, E.; Santomá, P.; Duran-Frigola, M.; Hernández, B.; Llinàs, M. C.; Ruiz-González, R.; Nonell, S.; Sánchez-García, D.; Edelman, E. R.; Balcells, M. *Langmuir* **2013**, *29* (31), 9734.

(56) Planas, O.; Gallavardin, T.; Nonell, S. In *Handbook of Porphyrin Science*; Guilard, R., Smith, K. M., Kadish, K. M., Eds.; World Scientific Publishers, 2016; pp 299–349.

(57) Arad, O.; Rubio, N.; Sanchez-Garcia, D.; Borrell, J. I.; Nonell, S. *J. Porphyrins Phthalocyanines* **2009**, *13* (3), 376.

(58) Duran-Frigola, M.; Tejedor-Estrada, R.; Sánchez-García, D.; Nonell, S. *Phys. Chem. Chem. Phys.* **2011**, *13* (21), 10326.

(59) Planas, O.; Tejedor-Estrada, R.; Nonell, S. *J. Porphyrins Phthalocyanines* **2012**, *16* (5–6), 633.

(60) Vogel, E.; Mueller, M.; Halpern, O.; D. Cross, A. 9-SUBSTITUTED PORPHYCENES. US5610175, 1998.

(61) Okawara, T.; Abe, M.; Shimakoshi, H.; Hisaeda, Y. *Bull. Chem. Soc. Jpn.* **2011**, *84* (7), 718.

(62) Planas, O.; Boix-Garriga, E.; Rodríguez-Amigo, B.; Torra, J.; Bresolí-Obach, R.; Flors, C.; Viappiani, C.; Agut, M.; Ruiz-González, R.; Nonell, S. In *Photochemistry*; Fasani, E., Albini, A., Eds.; Special Periodical Reports; Royal Society of Chemistry, 2015; Vol. 42, pp 233–278.

(63) Zolot, R. S.; Basu, S.; Million, R. P. *Nat. Rev. Drug Discov.* **2013**, *12* (4), 259.

(64) Mew, D.; Wat, C. K.; Towers, G. H.; Levy, J. G. *J. Immunol.* **1983**, *130* (3), 1473.

(65) Mitsunaga, M.; Ogawa, M.; Kosaka, N.; Rosenblum, L. T.; Choyke, P. L.; Kobayashi, H. *Nat. Med.* **2011**, *17* (12), 1685.

(66) Mitsunaga, M.; Nakajima, T.; Sano, K.; Choyke, P. L.; Kobayashi, H. *Bioconjug. Chem.* **2012**, *23* (3), 604.

(67) Spring, B. Q.; Abu-Yousif, A. O.; Palanisami, A.; Rizvi, I.; Zheng, X.; Mai, Z.; Anbil, S.; Sears, R. B.; Mensah, L. B.; Goldschmidt, R.; Erdem, S. S.; Oliva, E.; Hasan, T. *Proc. Natl. Acad. Sci. U. S. A.* **2014**, *111* (10), E933.

(68) Pereira, P. M. R.; Korsak, B.; Sarmento, B.; Schneider, R. J.; Fernandes, R.; Tomé, J. P. C. *Org. Biomol. Chem.* **2015**, *13* (9), 2518.

(69) Bullous, A. J.; Alonso, C. M. A.; Boyle, R. W. *Photochem. Photobiol. Sci.* **2011**, *10* (5), 721.

(70) Cline, G. W.; Hanna, S. B. *J. Am. Chem. Soc.* **1987**, *109* (10), 3087.

(71) Clarke, O. J.; Boyle, R. W. *Chem. Commun.* **1999**, *21*, 2231.

(72) Hudson, R.; Carcenac, M.; Smith, K.; Madden, L.; Clarke, O. J.; Pèlegrin, A.; Greenman, J.; Boyle, R. W. *Br. J. Cancer* **2005**, *92* (8), 1442.

(73) Sutton, J. M.; Clarke, O. J.; Fernandez, N.; Boyle, R. W. *Bioconjug. Chem.* **2002**, *13* (2), 249.

(74) Duan, W.; Smith, K.; Savoie, H.; Greenman, J.; Boyle, R. W. *Org. Biomol. Chem.* **2005**, *3* (13), 2384.

(75) Savellano, M. D.; Hasan, T. *Photochem. Photobiol.* **2003**, *77* (4), 431.

(76) Goff, B. A.; Blake, J.; Bamberg, M. P.; Hasan, T. *Br. J. Cancer* **1996**, *74* (8), 1194.

(77) del Governatore, M.; Hamblin, M. R.; Piccinini, E. E.; Ugolini, G.; Hasan, T. *Br. J. Cancer* **2000**, *82* (1), 56.

(78) Savellano, M. D.; Pogue, B. W.; Hoopes, P. J.; Vitetta, E. S.; Paulsen, K. D. *Cancer Res.* **2005**, *65* (14), 6371.

(79) Abu-Yousif, A. O.; Moor, A. C. E.; Zheng, X.; Savellano, M. D.; Yu, W.; Selbo, P. K.; Hasan, T. *Cancer Lett.* **2012**, *321* (2), 120.

(80) Smith, K.; Malatesti, N.; Cauchon, N.; Hunting, D.; Lecomte, R.; van Lier, J. E.; Greenman, J.; Boyle, R. W. *Immunology* **2010**, *132* (2), 256.

(81) Duska, L. R.; Hamblin, M. R.; Bamberg, M. P.; Hasan, T. *Br. J. Cancer* **1997**, *75* (6), 837.

(82) Palumbo, A.; Hauler, F.; Dziunycz, P.; Schwager, K.; Soltermann, A.; Pretto, F.; Alonso, C.; Hofbauer, G. F.; Boyle, R. W.; Neri, D. *Br. J. Cancer* **2011**, *104* (7), 1106.

(83) Staneloudi, C.; Smith, K. A.; Hudson, R.; Malatesti, N.; Savoie, H.; Boyle, R. W.; Greenman, J. *Immunology* **2007**, *120* (4), 512.

(84) Kuimova, M. K.; Bhatti, M.; Deonarain, M.; Yahioglu, G.; Levitt, J. A.; Stamati, I.; Suhling, K.; Phillips, D. *Photochem. Photobiol. Sci.* **2007**, *6* (9), 933.

(85) Heukers, R.; van Bergen en Henegouwen, P. M. P.; Oliveira, S. *Nanomedicine Nanotechnology, Biol. Med.* **2014**, *10* (7), 1441.

(86) Watanabe, R.; Hanaoka, H.; Sato, K.; Nagaya, T.; Harada, T.; Mitsunaga, M.; Kim, I.; Paik, C. H.; Wu, a. M.; Choyke, P. L.; Kobayashi, H. *J. Nucl. Med.* **2015**, *56* (1), 140.

(87) Sato, K.; Choyke, P. L.; Kobayashi, H. *PLoS One* **2014**, *9* (11), e113276.

(88) Sato, K.; Nagaya, T. *Oncotarget* **2015**, *6* (23), 19747.

(89) Nagaya, T.; Sato, K.; Harada, T.; Nakamura, Y.; Choyke, P. L.; Kobayashi, H. *PLoS One* **2015**, *10* (8), e0136829.

(90) Sato, K.; Nagaya, T.; Choyke, P. L.; Kobayashi, H. *Theranostics* **2015**, *5* (7), 698.

(91) Kishimoto, S.; Bernardo, M.; Saito, K.; Koyasu, S.; Mitchell, J. B.; Choyke, P. L.; Krishna, M. C. *Free Radic. Biol. Med.* **2015**, *85*, 24.

(92) de Boer, E.; Warram, J. M.; Hartmans, E.; Bremer, P. J.; Bijl, B.; Crane, L. M. a.; Nagengast, W. B.; Rosenthal, E. L.; van Dam, G. M. *J. Nucl. Med.* **2014**, *55* (11), 1893.

(93) Sano, K.; Nakajima, T.; Choyke, P. L.; Kobayashi, H. *ACS Nano* **2013**, *7* (1), 717.

(94) Sano, K.; Nakajima, T.; Choyke, P. L.; Kobayashi, H. *Mol. Cancer Ther.* **2014**, *13* (2), 426.

(95) Wang, S.; Fan, W.; Kim, G.; Hah, H. J.; Lee, Y. E.; Kopelman, R.; Ethirajan, M.; Gupta, A.; Goswami, L. N.; Pera, P.; Morgan, J.; Pandey, R. K. *Lasers Surg. Med.* **2011**, *43* (7), 686.

(96) Greish, K. In *Cancer Nanotechnology*; Grobmyer, S. R., Moudgil, B. M., Eds.; Springer Science+Business Media, Inc., 2010; pp 25–37.

(97) Kumar, S.; Aaron, J.; Sokolov, K. *Nat. Protoc.* **2008**, *3* (2), 314.

(98) Soriano, J.; García-Díaz, M.; Mora, M.; Sagrista, M. L.; Nonell, S.; Villanueva, A.; Stockert, J. C.; Canete, M. *Biochim. Biophys. Acta* **2013**, *1830* (10), 4611.

(99) Boix-Garriga, E.; Acedo, P.; Casadó, A.; Villanueva, A.; Stockert, J. C.; Cañete, M.; Mora, M.; Sagristá, M. L.; Nonell, S. *Nanotechnology* **2015**, *26* (36), 365104 (16pp).

(100) Couleaud, P.; Morosini, V.; Frochot, C.; Richeter, S.; Raehm, L.; Durand, J. O. *Nanoscale* **2010**, *2* (7), 1083.

(101) Stuchinskaya, T.; Moreno, M.; Cook, M. J.; Edwards, D. R.; Russell, D. a. *Photochem. Photobiol. Sci.* **2011**, *10* (5), 822.

(102) Stallivieri, A.; Baros, F.; Arnoux, P.; Vanderesse, R.; Barberi-Heyob, M.; Frochot, C. 2016; pp 209–223.

(103) Zampini, G.; Planas, O.; Marmottini, F.; Gulías, O.; Agut, M.; Nonell, S.; Latterini, L. *RSC Adv.* **2017**, *7* (24), 14422.

(104) Hutter, E.; Fendler, J. H. *Adv. Mater.* **2004**, *16* (19), 1685.

(105) Jain, P. K.; El-Sayed, M. A. *Chem. Phys. Lett.* **2010**, *487* (4–6), 153.

(106) Geddes, C. D.; Lakowicz, J. R. *J. Fluoresc.* **2002**, *12* (2), 121.

(107) Zhang, Y. X.; Aslan, K.; Malyn, S. N.; Geddes, C. D. *Chem. Phys. Lett.* **2006**, *427* (4–6), 432.

(108) Aslan, K.; Gryczynski, I.; Malicka, J.; Matveeva, E.; Lakowicz, J. R.; Geddes, C. D. *Curr. Opin. Biotechnol.* **2005**, *16*, 55.

(109) Stiles, P. L.; Dieringer, J. A.; Shah, N. C.; Van Duyne, R. P. *Annu. Rev. Anal. Chem.* **2008**, *1* (1), 601.

(110) Le Ru, E. C.; Etchegoin, P. G. *Annu. Rev. Phys. Chem.* **2012**, *63* (1), 65.

(111) Zhang, Y.; Aslan, K.; Previte, M. J. R.; Geddes, C. D. *Proc. Natl. Acad. Sci. U. S. A.* **2008**, *105* (6), 1798.

(112) Ragàs, X.; Gallardo, A.; Zhang, Y.; Massad, W.; Geddes, C. D.; Nonell, S. *J. Phys. Chem. C* **2011**, *115* (33), 16275.

(113) Toftegaard, R.; Arnbjerg, J.; Daasbjerg, K.; Ogilby, P. R.; Dmitriev, A.; Sutherland, D. S.; Poulsen, L. *Angew. Chem. Int. Ed.* **2008**, *47* (32), 6025.

(114) Khaing Oo, M. K.; Yang, Y.; Hu, Y.; Gomez, M.; Du, H.; Wang, H. *ACS Nano* **2012**, *6* (3), 1939.

(115) Hayden, S. C.; Austin, L. A.; Near, R. D.; Ozturk, R.; El-Sayed, M. A. *J. Photochem. Photobiol. A* **2013**, *269*, 34.

(116) Mooi, S. M.; Heyne, B. *Photochem. Photobiol.* **2013**, *90* (39), 85.

(117) Hu, B.; Cao, X.; Nahan, K.; Caruso, J.; Tang, H.; Zhang, P. *J. Mater. Chem. B* **2014**, *2* (40), 7073.

(118) Anger, P.; Bharadwaj, P.; Novotny, L. *Phys. Rev. Lett.* **2006**, *96* (11), 113002.

(119) Ming, T.; Chen, H.; Jiang, R.; Li, Q.; Wang, J. *J. Phys. Chem. Lett.* **2012**, *3* (2), 191.

(120) Mishra, H.; Mali, B. L.; Karolin, J.; Dragan, A. I.; Geddes, C. D. *Phys. Chem. Chem. Phys.* **2013**, *15* (45), 19538.

(121) Abadeer, N. S.; Brennan, M. R.; Wilson, W. L.; Murphy, C. J. *ACS Nano* **2014**, *8* (8), 8392.

2

Compendium of publications

The compendium of publications is presented in this chapter as follows. First, a novel conjugation strategy for the labelling of biomolecules and nanoparticles based on the isothiocyanate chemistry is presented. In the second paper, the effects of silica nanostructures onto the $^1O_2$ deactivation kinetics is rationalized and finally, all knowledge is applied to the development of plasmonic nanostructures comprised by a silver metallic core protected by silica shells of different thickness.

2.1. **Planas, O.**; Gallavardin, T.; Nonell, S.; A novel fluoro-chromogenic click reaction for the labelling of proteins and nanoparticles with near-IR theranostic agents. *Chem. Commun.*, 2015, 51, 5586-5589. DOI: 10.1039/c4cc09070e.

2.2. Zampini, G.; **Planas, O.**; Marmottini, F.; Gulías, O.; Agut, M.; Nonell, S.; Latterini, L. Morphology effects on singlet oxygen production and bacterial photoinactivation efficiency by different silica-Protoporphyrin IX nanocomposites. *RSC Adv.*, 2017, 7, 14422-14429. DOI: 10.1039/ c7ra00784a.

2.3. **Planas, O.**; Macia, N.; Agut, M.; Nonell, S.; Heyne, B. Distance-Dependent Plasmon-Enhanced Singlet Oxygen Production and Emission for Bacterial Inactivation. *J. Am. Chem. Soc.*, 2016, 138, 2762-2768. DOI: 10.1021/jacs.5b12704.

2.1

Planas, O.; Gallavardin, T.; Nonell, S.; A novel fluoro-chromogenic click reaction for the labelling of proteins and nanoparticles with near-IR theranostic agents. *Chem. Commun.*, 2015, 51, 5586-5589.
DOI: 10.1039/c4cc09070e.

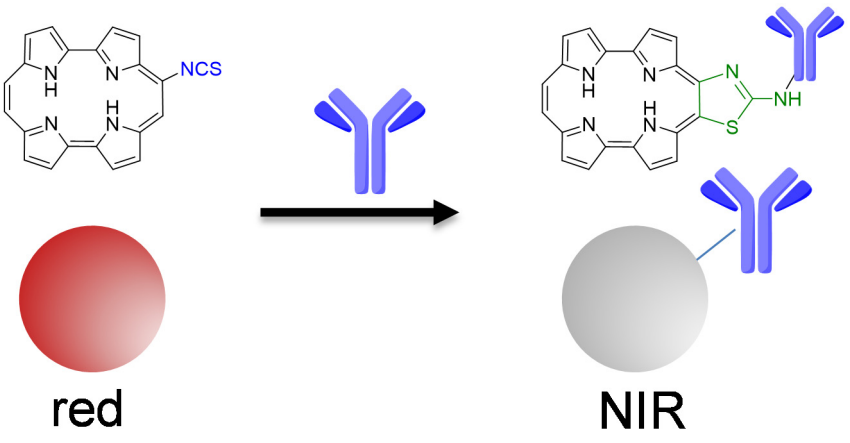

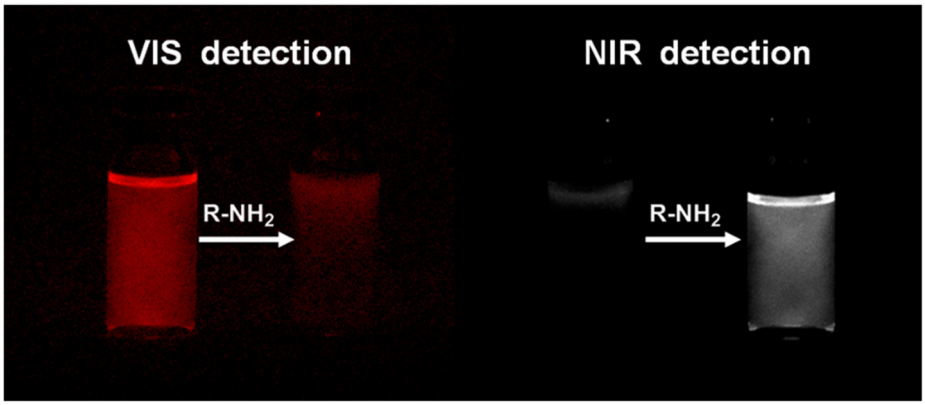

Volume 51 | Number 26 | 4 April 2015 | Pages 5537–5780

ChemComm

Chemical Communications

www.rsc.org/chemcomm

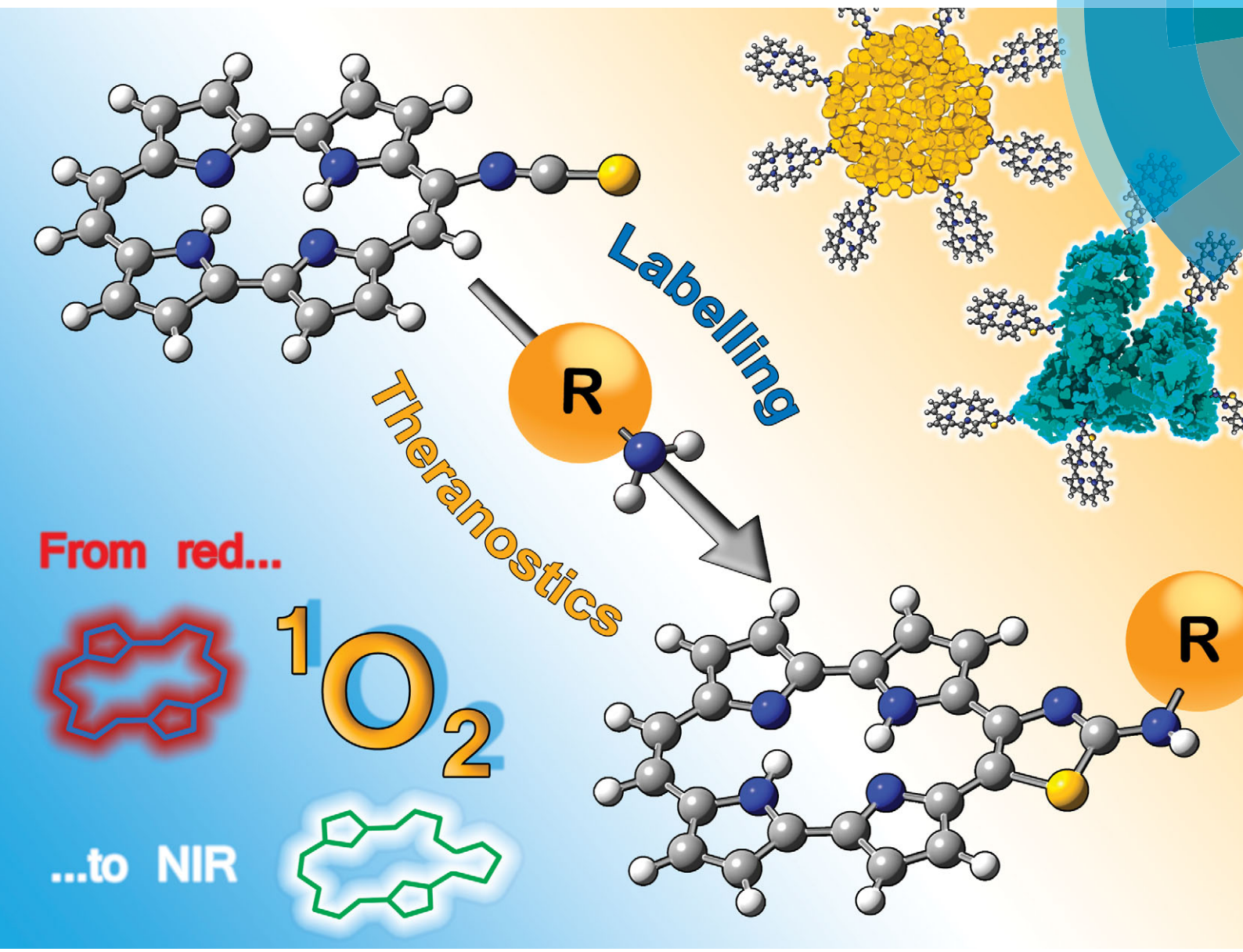

ISSN 1359-7345

ROYAL SOCIETY OF CHEMISTRY

COMMUNICATION

Santi Nonell *et al.*

A novel fluoro-chromogenic click reaction for the labelling of proteins and nanoparticles with near-IR theranostic agents

ChemComm

COMMUNICATION

Cite this: *Chem. Commun.*, 2015, **51**, 5586

Received 13th November 2014,
Accepted 8th December 2014

DOI: 10.1039/c4cc09070e

www.rsc.org/chemcomm

A novel fluoro-chromogenic click reaction for the labelling of proteins and nanoparticles with near-IR theranostic agents†‡

Oriol Planas, Thibault Gallavardin and Santi Nonell*

Reaction of porphycene isothiocyanates with primary and secondary amines leads to the formation of thiazolo[4,5-c]porphycenes, with a substantial shift in the absorption and fluorescence spectra. The conjugates show fluorescence in the near-infrared and are capable of photosensitizing the production of the cytotoxic species singlet oxygen.

Theranostic nanomedicine is an emerging therapeutic strategy that combines a contrast agent and a drug on a single nanoplatform for enhanced diagnosis and treatment of localised diseases.[1a] Of particular interest are photoactivatable theranostic agents that allow simultaneous fluorescence imaging and localised generation of cytotoxic species.[1b,c] Current research efforts are directed to the development of theranostic labels that show absorption and emission in the red and near-infrared spectral range,[2a] as well as strong and selective binding to proteins and nanoparticles.[2b] Several click reactions have been developed to this end, employing reactive groups such as the isothiocyanate (ITC) for conjugation to free amino residues,[2c,d] maleimide for cysteine-reduced thiol groups,[2e,f] and carbodiimide for carboxyl groups.[2g]

A common and severe drawback of current labels is that the optical and fluorescence properties of the conjugates are not too different from those of the unbound probes, which makes it very difficult to differentiate between covalent adducts and non-specific complexes.[2c] The latter pose a serious problem to bioconjugate-based biological assays and therapies as they can be released into the biological milieu, altering their results.

In the domain of fluorescence, the conventional solution to this problem is the development of turn-on labels that increase their fluorescence intensity upon binding.[2h,i] However, since the spectra of the bound and unbound probes are the same and only the intensity changes, good contrast cannot be generally achieved.[2j] A more robust solution would be the use of probes that change their absorption and fluorescence *spectra* upon covalent binding since this would allow to selectively excite and monitor the bound and unbound tags. This concept has been recently demonstrated for the labelling of proteins with pyrilium fluorescent dyes that change their emission from red to blue.[3]

However, to date no single theranostic agent has been reported, which undergoes a similar spectral change upon conjugation. In the course of our ongoing research on photoimmunotherapy[4] we observed marked spectral changes when porphycenes containing a 9-ITC group (9-ITPPos) were reacted with primary and secondary amines (Fig. 1). Porphycenes, discovered by Vogel in 1986,[5a] are porphyrin isomers of lower symmetry and unique properties.[5b–i] Porphycenes are currently being explored as photodynamic therapy agents due to their excellent optical, fluorescent and photosensitising properties.[6]

It is well known that fluorophores containing ITC groups produce thioureas upon clicking to terminal amino residues of

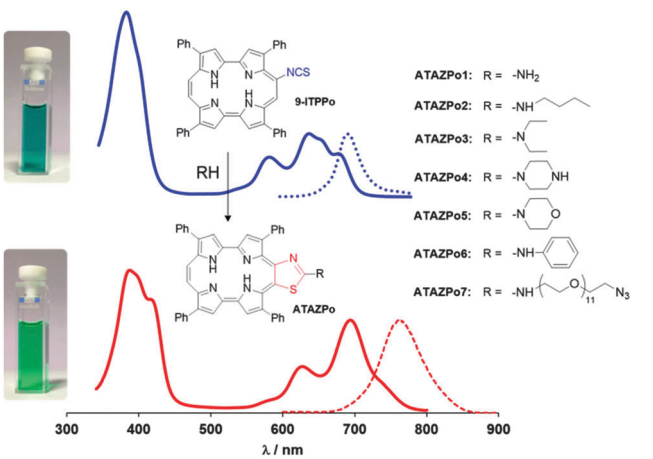

Fig. 1 Structural and absorption (solid line) and fluorescence (dashed line) spectral changes upon reaction of 9ITPPo with primary and secondary amines. The spectra shown correspond to ATAZPo2 in acetone.

Institut Químic de Sarrià, Universitat Ramon Llull, Via Augusta, 390, 08017, Barcelona, Spain. E-mail: santi.nonell@iqs.url.edu

† Dedicated to Professor Juan C. "Tito" Scaiano on the occasion of his 70th birthday.

‡ Electronic supplementary information (ESI) available: Experimental techniques and procedures, characterisation data, and additional results. See DOI: 10.1039/c4cc09070e

biomolecules or amino-functionalised nanoparticles.[2f] An archetypical example of such tags is the widely used fluorescein-ITC;[7] however, unlike the porphycene-ITCs, its spectrum does not appreciably change upon formation of the thiourea bridge.

Isolation of the reaction products of porphycene-ITCs with amines revealed that the underlying cause for the colour change was the spontaneous evolution of the originally-formed thiourea to 2-aminothiazolo[4,5-*c*]porphycene (ATAZPo; Fig. 1 and Schemes S2 and S3, ESI‡), with a concomitant red-shift of its fluorescence spectrum by more than 70 nm. Formation of thiourea and its subsequent cyclisation proceeded almost quantitatively and with high selectivity at room temperature (Table 1), which is a pre-requisite for "click" labelling reactions.[8] An additional benefit of the unexpected evolution of the porphycene-thiourea system is that it prevents the hydrolysis of the conjugates by urease enzymes.[9]

The formed ATAZPos have several relevant chemical, optical and photophysical properties that make them excellent candidates for theranostic applications (Table 2). Firstly, their absorption spectrum is shifted by more than 70 nm relative to that of the precursor 9-ITPPo, which allows their selective excitation even in the presence of any unbound precursor (Fig. S34, ESI‡). Secondly, their fluorescence shifts to the near-IR (Fig. 2), where tissue is most transparent and shows less autofluorescence.[10a] Thirdly, the fluorescence quantum yields are higher than those of the most common near-IR fluorophores, *e.g.*, 0.01 for the IR800 dye[10b] and 0.04 for indocyanine green.[10c] Finally, ATAZPos produce singlet oxygen with high yields, which allows using them also for therapeutic purposes (Fig. S35, ESI‡).[11]

Encouraged by the above results we set out to explore the potential of 9-ITPPo for conjugation to biomolecules and nanoparticles. Bovine serum albumin (BSA) and amino-functionalised gold nanoclusters (AuNCs) were selected for proof-of-concept purposes. In a typical experiment, a stock solution of 9-ITPPo was prepared and mixed with BSA in carbonate buffer (pH 9.2) or with AuNCs in ethanol. The reaction vessels were protected from light and stirred at room temperature. Formation of covalent adducts was unequivocally demonstrated by the changes in absorption and fluorescence spectra (Fig. 3 and Fig. S30, ESI‡) and the conjugates retained their ability to photosensitise the production of singlet oxygen.

Insight into the formation of the thiazole ring was obtained from the study of the reaction kinetics. The time evolution of the absorbance of a mixture of 9-ITPPo and *n*-butylamine was measured in air-equilibrated toluene (Fig. 4). The isothiocyanate group disappeared within minutes with the concomitant formation of thiourea as the only product, as deduced from the observation of isosbestic points in the absorption spectra and the ^{1}H-NMR spectrum (Fig. S33, ESI‡). This intermediate evolved over a period of several hours to the final product ATAZPo. The time-resolved spectra were analysed using the Specfit/32 software from Spectrum Software Associates and could be successfully fitted by a simple two-step consecutive

Table 1 Reaction of 9-ITPPo with selected primary and secondary amines at room temperature

Substrate	Compound	Solvent	Reaction time/h	Yield (%)
Ammonia	ATAZPo1	THF	3	97
n-Butylamine	ATAZPo2	CH_2Cl_2	3	95
Diethylamine	ATAZPo3	CH_2Cl_2	5	95
Piperazine	ATAZPo4	CH_2Cl_2	3	90
Morpholine	ATAZPo5	CH_2Cl_2	3	90
Aniline	ATAZPo6	CH_2Cl_2	24	80
O-(2-aminoethyl)-*O*′-(2-azidoethyl)nonaethyleneglycol	ATAZPo7	CH_2Cl_2	3	85

Table 2 Optical and photophysical properties of 9-ITPPo and ATAZPo derivatives in acetone

Compound	λ_m[a]	ε[b]	λ_F[c]	Φ_F[d]	τ_s[e]	τ_T[f]	Φ_Δ[g]
9-ITPPo	667	2.1×10^4	693	0.07	0.8	35	0.49
ATAZPo1	745	9.3×10^3	750	0.03	0.5	30	0.30
ATAZPo2	743	2.0×10^4	756	0.08	0.6	20	0.27
ATAZPo3	763	1.4×10^4	775	0.05	0.7	50	0.24
ATAZPo4	744	1.8×10^4	764	0.05	0.9	51	0.24
ATAZPo5	740	1.2×10^4	758	0.06	0.9	32	0.30
ATAZPo6	750	1.2×10^4	759	0.04	0.6	35	0.20
ATAZPo7	748	1.7×10^4	768	0.07	0.9	23	0.31

[a] Wavelength of the lowest-energy absorption band (nm). [b] Molar absorption coefficient at λ_m (M^{-1} cm^{-1}). [c] Wavelength of fluorescence (nm). [d] Fluorescence quantum yield. [e] Singlet state lifetime in air (ns). [f] Triplet state lifetime under argon (μs). [g] Singlet oxygen quantum yield.

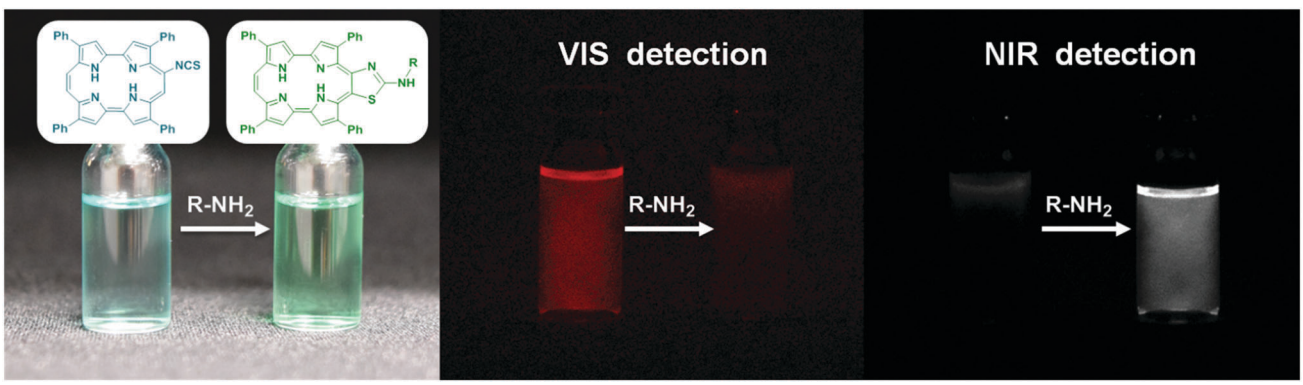

Fig. 2 Solutions of 9-ITPPo and ATAZPo under white light (left) and under UV (365 nm) radiation (middle and right). While 9-ITPPo shows visible red fluorescence, ATAZPo emits mainly in the near-IR (λ_{obs} > 780 nm).

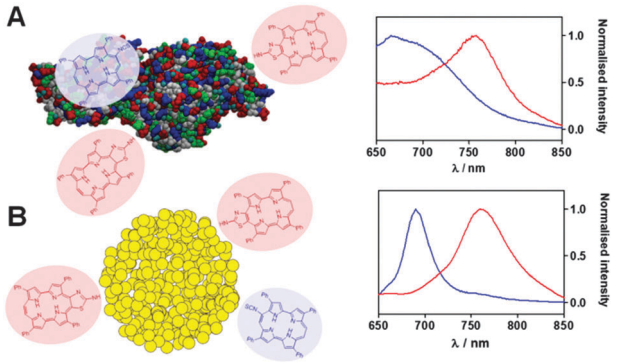

Fig. 3 Fluorescence spectra of unbound 9-ITPPo (blue) and its covalent adduct ATAZPo (red) with BSA (A) and AuNCs (B).

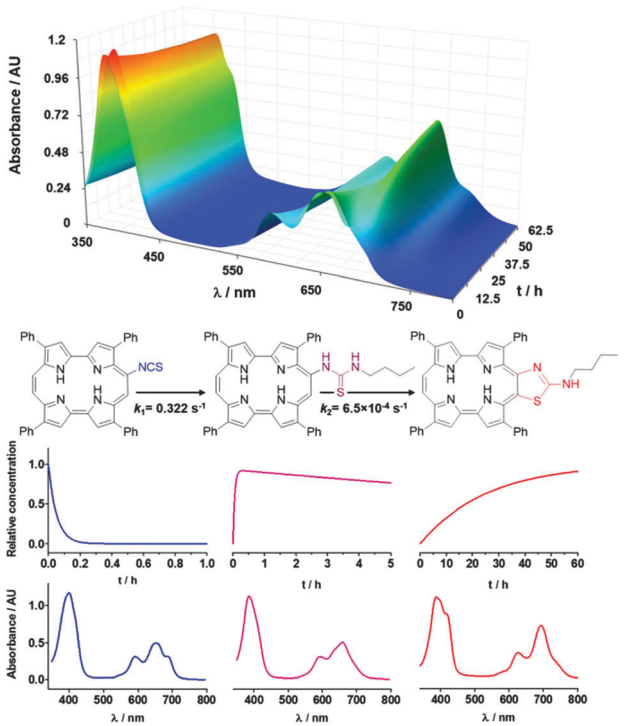

Fig. 4 Top: time evolution of the absorbance of a mixture of 9-ITPPo (15 μM) and *n*-butylamine (3 mM) in toluene. Bottom: structures, concentration evolution and spectral profiles of the reactant, the intermediate and the product (from left to right) achieved through singular value decomposition of the spectral evolution in air.

pseudo-first order kinetic model (9-ITPPo → 9-TUPo → ATAZPo) with rate constants 0.32 s^{-1} and 6.5 × 10^{-4} s^{-1} for the first and second steps, respectively, at room temperature. Flushing the solutions with argon had no measurable effect on the rate constants.

The Specfit software also yielded the spectra of the three species involved. An excellent match was obtained between the recovered and experimental spectra of the 9-ITPPo reactant, the 9-TUPo intermediate, and the ATAZPo product (Fig. 4).

The spontaneous cyclization of 9-TUPo was unexpected on the basis of the known literature for aromatic thioureas. Although thioureas are known to cyclize to the corresponding thiazoles, this is observed only when they either contain a halogen leaving group,[12a,b] or are activated with palladium[12c] or copper,[12d] or in the presence of added oxidants such as bromine or the tribromide anion.[12e–h] None of these factors is present in the porphycenes studied. Moreover, the thioureas of the closely-related porphyrins and phthalocyanines do not spontaneously cyclise to the corresponding thiazole derivatives.[13] Thus, there is something unique in the electronic structure of porphycene that makes the cyclization reaction highly specific for this porphyrin isomer.

Additional insight was obtained by computational modelling studies. Using density functional methodology, we evaluated the molecular orbitals' energy and shape for a series of aromatic thioureas (Fig. 5). The results revealed that their HOMO is localized on the highly nucleophilic sulphur atom of these compounds, while the LUMO is mostly on the aromatic ring. This suggests that cyclisation of the thioureas has a substantial intramolecular sulphur-to-ring charge-transfer character.

In the framework of the frontier molecular orbital theory, the reaction rate can thus be expected to be proportional to the energy gap between the HOMO of the thiourea nucleophile and the LUMO of the electrophile.[14] As would probably be expected, the HOMO–LUMO gap for all porphyrinoids is lower than for the phenyl-thiourea, consistent with the larger size of their aromatic ring, which allows a better electron delocalization. The striking finding was that the HOMO–LUMO gap in 9-TUPo was roughly half that in the related porphyrin and phthalocyanine thioureas. This unique feature of porphycenes sets them apart from the more symmetrical porphyrinoids such as porphyrins and phthalocyanines and stems from their very particular electronic structure.[15] Thus, porphycenes are ideal substrates for the formation of thiazole-fused derivatives, which could be exploited for a variety of purposes, particularly for labelling of biomolecules and nanosystems aimed at imaging and therapeutic applications.

As a further proof for the above mechanism, and in order to explore the scope of the new porphycene chemistry, 9-benzoamide porphycene (9-AmPo) was prepared from 9-amino-2,7,12,17-tetraphenylporphycene (9-ATPPo)[5e] and treated with Lawesson's reagent, which is known to promote the formation of the

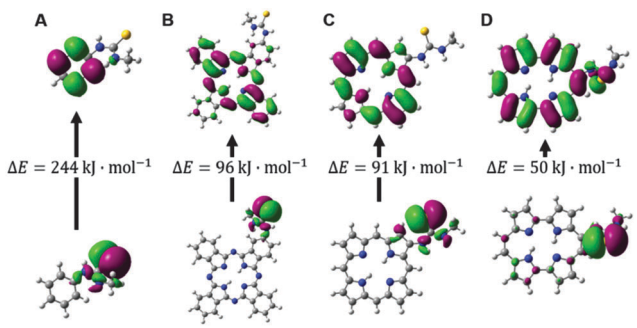

Fig. 5 HOMO–LUMO energy gap ($\Delta E = E_{LUMO} - E_{HOMO}$) of different aromatic thioureas, namely, (A) *N*-methyl-*N*′-phenylthiourea, (B) *N*-methyl-*N*′-(2-phthalocyanine)-thiourea, (C) *N*-methyl-*N*′-(2-porphyrin)-thiourea, and (D) *N*-methyl-*N*′-(9-porphycene)-thiourea.

thioamide functionality.[16] Once again, instead of the expected 9-benzothioamide porphycene, we isolated the corresponding thiazolo[4,5-*c*]porphycene (Scheme S5, Fig. S36 and Table S1, ESI‡). Thus, cyclisation is not restricted to thioureas but can also be realised with thioamides.

In summary, we report a novel specific reaction of porphycenes that allows the formation of thiazole-fused porphycene conjugates with unique absorption, fluorescence and photosensitizing properties. Thus, porphycene-ITCs are novel molecular entities with high potential for imaging and therapeutic applications. Work is currently in progress to explore such applications and shall be reported in due course.

This work has been supported by the Spanish Ministry of Economy and Competitiveness (grants No. CTQ2010-20870-C03-01 and CTQ2013-48767-C3-1-R). O. P. thanks the SUR del DEC de la Generalitat de Catalunya for his predoctoral fellowship (grant No. 2014FI_B 00777).

Notes and references

1 (*a*) T. Lammers, S. Aime, W. E. Hennink, G. Storm and F. Kiessling, *Acc. Chem. Res.*, 2011, **44**, 1029–1038; (*b*) R. Bardhan, S. Lal, A. Joshi and N. Halas, *Acc. Chem. Res.*, 2011, **44**, 936–946; (*c*) J. Xie, S. Lee and X. Chen, *Adv. Drug Delivery Rev.*, 2010, **62**, 1064–1079.

2 (*a*) P. Huang, J. Lin, X. Wang, Z. Wang, C. Zhang, M. He, K. Wang, F. Chen, Z. Li, G. Shen, D. Cui and X. Chen, *Adv. Mater.*, 2012, **24**, 5104–5110; (*b*) A. Nadler and C. Schultz, *Angew. Chem., Int. Ed.*, 2013, **52**, 2408–2410; (*c*) R. Hudson, M. Carcenac, K. Smith, L. Madden, O. J. Clarke, A. Pèlegrin, J. Greenman and R. W. Boyle, *Br. J. Cancer*, 2005, **92**, 1442–1449; (*d*) S. Ohkuma and B. Poole, *Proc. Natl. Acad. Sci. U. S. A.*, 1978, **75**, 3327–3331; (*e*) S. S. Ghosh, P. M. Kao, A. W. McCue and H. L. Chappelle, *Bioconjugate Chem.*, 1990, **1**, 71–76; (*f*) M. Mitsunaga, M. Ogawa, N. Kosaka, L. T. Rosenblum, P. L. Choyke and H. Kobayashi, *Nat. Med.*, 2011, **17**, 1685–1691; (*g*) M. Kobayashi and Y. Chiba, *Anal. Biochem.*, 1994, **219**, 189–194; (*h*) Y. Hori and K. Kikuchi, *Curr. Opin. Chem. Biol.*, 2013, **17**, 644–650; (*i*) S. Mizukami, Y. Hori and K. Kikuchi, *Acc. Chem. Res.*, 2014, **47**, 247–256; (*j*) Q. Yan, S. L. Schwartz, S. Maji, F. Huang, C. Szent-Gyorgyi, D. S. Lidke, K. A. Lidke and M. P. Bruchez, *ChemPhysChem*, 2014, **15**, 687–695.

3 (*a*) B. K. Wetzl, S. M. Yarmoluk, D. B. Craig and O. S. Wolfbeis, *Angew. Chem., Int. Ed.*, 2004, **43**, 5400–5402; (*b*) B. K. Hoefelschweiger, A. Duerkop and O. S. Wolfbeis, *Anal. Biochem.*, 2005, **344**, 122–129.

4 E. Rosàs, P. Santomá, M. Duran-Frigola, B. Hernandez, M. C. Llinàs, R. Ruiz-González, S. Nonell, D. Sánchez-García, E. R. Edelman and M. Balcells, *Langmuir*, 2013, **29**, 9734–9743.

5 (*a*) E. Vogel, M. Kocher, H. Schmickler and J. Lex, *Angew. Chem., Int. Ed.*, 1986, **25**, 257–259; (*b*) P. F. Aramendia, R. W. Redmond, S. Nonell, W. Schuster, S. E. Braslavsky, K. Schaffner and E. Vogel, *Photochem. Photobiol.*, 1986, **44**, 555–559; (*c*) S. E. Braslavsky, M. Müller, D. Mártire, S. Pörting, S. G. Bertolotti, S. Chakravorti, G. Koç-Weier, K. Bernd and K. Schaffner, *J. Photochem. Photobiol., B*, 1997, **40**, 191–198; (*d*) M. Duran-Frigola, R. Tejedor-Estrada, D. Sánchez-García and S. Nonell, *Phys. Chem. Chem. Phys.*, 2011, **13**, 10326–10332; (*e*) O. Planas, R. Tejedor-Estrada and S. Nonell, *J. Porphyrins Phthalocyanines*, 2012, **16**, 633–640; (*f*) H. Shimakoshi, K. Sasaki, Y. Iseki and Y. Hisaeda, *J. Porphyrins Phthalocyanines*, 2012, **16**, 530–536; (*g*) W. Brenner, J. Malig, R. D. Costa, D. M. Guldi and N. Jux, *Adv. Mater.*, 2013, **25**, 2314–2318; (*h*) T. Kumagai, F. Hanke, S. Gawinkowski, J. Sharp, K. Kotsis, J. Waluk, M. Persson and L. Grill, *Nat. Chem.*, 2014, **6**, 41–46; (*i*) T. Okabe, D. Kuzuhara, M. Suzuki, N. Aratani and H. Yamada, *Org. Lett.*, 2014, **16**, 3508–3511.

6 (*a*) C. Richert, J. M. Wessels, M. Muller, M. Kisters, T. Benninghaus and A. E. Goetz, *J. Med. Chem.*, 1994, **37**, 2797–2807; (*b*) J. C. Stockert, M. Cañete, A. Juarranz, A. Villanueva, R. W. Horobin, J. I. Borrell, J. Teixido and S. Nonell, *Curr. Med. Chem.*, 2007, **14**, 997–1026; (*c*) X. Ragàs, D. Sánchez-García, R. Ruiz-González, T. Dai, M. Agut, M. R. Hamblin and S. Nonell, *J. Med. Chem.*, 2010, **53**, 7796–7803; (*d*) M. García-Díaz, D. Sánchez-García, J. Soriano, M. L. Sagristà, M. Mora, A. Villanueva, J. C. Stockert, M. Cañete and S. Nonell, *Med. Chem. Commun.*, 2011, **2**, 616–619; (*e*) R. Ruiz-González, P. Acedo, D. Sánchez-García, S. Nonell, M. Cañete, J. C. Stockert and A. Villanueva, *Eur. J. Med. Chem.*, 2013, **63**, 401–414.

7 (*a*) G. Grunwaldt, S. Haebel and C. Spitz, *J. Photochem. Photobiol., B*, 2002, **67**, 177–186; (*b*) N. Klonis and W. H. Sawyer, *Photochem. Photobiol.*, 2003, **77**, 502–509.

8 (*a*) M. O. Senge and J. C. Brandt, *Photochem. Photobiol.*, 2011, **87**, 1240–1296; (*b*) P. Thirumurugan, D. Matosiuk and K. Jozwiak, *Chem. Rev.*, 2013, **113**, 4905–4979.

9 C. Lopreore and L. D. Byers, *Arch. Biochem. Biophys.*, 1998, **349**, 299–303.

10 (*a*) A. M. Smith, M. C. Mancini and S. Nie, *Nat. Nanotechnol.*, 2009, **4**, 710–711; (*b*) X. Peng, H. Chen, D. R. Draney, W. Volcheck, A. Schutz-Geschwender and D. M. Olive, *Anal. Biochem.*, 2009, **388**, 220–228; (*c*) R. Philip, A. Penzkofer and W. Bäumler, *J. Photochem. Photobiol., A*, 1996, **96**, 137–148.

11 (*a*) S. S. Kelkar and T. M. Reineke, *Bioconjugate Chem.*, 2011, **22**, 1879–1903; (*b*) T. Lammers, S. Aime, W. E. Hennink, G. Storm and F. Kiessling, *Acc. Chem. Res.*, 2011, **44**, 1029–1038.

12 (*a*) R. Wang, W. Yang, L. Yue, W. Pan and H. Zeng, *Synlett*, 2012, 1643–1648; (*b*) S. K. Rout, S. Guin, J. Nath and B. K. Patel, *Green Chem.*, 2012, **14**, 2491–2498; (*c*) H.-Y. Thu, W.-Y. Yu and C.-M. Che, *J. Am. Chem. Soc.*, 2006, **128**, 9048–9049; (*d*) Y.-J. Guo, R.-Y. Tang, P. Zhong and J.-H. Li, *Tetrahedron Lett.*, 2010, **51**, 649–652; (*e*) A. D. Jordan, C. Luo and A. B. Reitz, *J. Org. Chem.*, 2003, **68**, 8693–8696; (*f*) Z.-G. Le, J.-P. Xu, H.-Y. Rao and M. Ying, *J. Heterocycl. Chem.*, 2006, **43**, 1123–1124; (*g*) R. B. Sparks, P. Polam, W. Zhu, M. L. Crawley, A. Takvorian, E. McLaughlin, M. Wei, P. J. Ala, L. Gonneville, N. Taylor, Y. Li, R. Wynn, T. C. Burn, P. C. C. Liu and A. P. Combs, *Bioorg. Med. Chem. Lett.*, 2007, **17**, 736–740; (*h*) K. Inamoto, C. Hasegawa, J. Kawasaki, K. Hiroya and T. Doi, *Adv. Synth. Catal.*, 2010, **352**, 2643–2655.

13 (*a*) J. M. Sutton, O. J. Clarke, N. Fernandez and R. W. Boyle, *Bioconjugate Chem.*, 2002, **13**, 249–263; (*b*) R. P. Hammer, C. V. Owens, S. Hwang, C. M. Sayes and S. A. Soper, *Bioconjugate Chem.*, 2002, **13**, 1244–1252; (*c*) W. Duan, K. Smith, H. Savoie, J. Greenman and R. W. Boyle, *Org. Biomol. Chem.*, 2005, **3**, 2384–2386.

14 (*a*) E. V. Anslyn and D. A. Dougherty, *Modern Physical Organic Chemistry*, University Science Books, Sausalito, 2006, p. 562; (*b*) L.-G. Zhuo, W. Liao and Z.-X. Yu, *Asian J. Org. Chem.*, 2012, **1**, 336–345.

15 J. Waluk, M. Muller, P. Swiderek, M. Kocher, E. Vogel, G. Hohlneicher and J. Michl, *J. Am. Chem. Soc.*, 1991, **113**, 5511–5527.

16 T. Ozturk, E. Ertas and O. Mert, *Chem. Rev.*, 2007, **107**, 5210–5278.

Electronic Supplementary Material (ESI) for ChemComm.

Supporting information

A novel fluoro-chromogenic click reaction for the labelling of proteins and nanoparticles with near-IR theranostic agents

*Oriol Planas, Thibault Gallavardin and Santi Nonell**

Table of contents:

1. Instrumentation and materials.

1. 1 Techniques for the identification of compounds

^{1}H and ^{13}C-NMR spectra were recorded on a Varian 400-MR spectrometer working at 400 MHz for ^{1}H or 100.6 MHz for ^{13}C. All NMR data were obtained in $CDCl_3$. Chemical shifts are reported in parts per million (ppm, δ) and are referenced to the residual signal of the solvent. Coupling constants are reported in Hertz (Hz). Spectral splitting patterns are designated as s (singlet), d (doublet), t (triplet), q (quartet), m (complex multiplet).

HPLC-MS analysis was carried out in an Agilent 1260 infinity Series chromatograph equipped with photodiode array detector (200–600 nm) and coupled to an Agilent 6130 quadrupole LC/MS. Separation was achieved using a Discovery® C18 (15m x 4.6 mm, 5µm particle size) column and an ACN:MeOH 85:15 mixture at 1.0 mL/min flow rate. The DAD detector was set at 400 nm matching the Soret band of porphycenes. API-ES positive ionization mode at 80V cone voltage was used. Fragmentations were scanned from 500 to 2500 m/z. Peaks were identified by their characteristic MS fragmentations.

1.2 Techniques for the characterisation of nanostructures

The size and morphology of tetraethylenglycol alkyl-thiol stabilized gold nanoclusters were determined by means of transmission electron microscopy (TEM). For TEM examination a single drop (15 µL) of the EtOH solution of the nanostructures was placed onto a copper grid coated with a carbon film. The grid was left to dry in air at room temperature. TEM analysis were carried out in a JEOL 2010F microscope, working at 200 kV. The particle size distribution was evaluated from several micrographs by means of an automatic image analyser software.

1.3 Spectroscopic techniques

The photophysical properties of porphycene derivatives were measured in spectroscopic grade acetone.

Absorption spectra were recorded on a Varian Cary 6000i dual-beam UV/Vis spectrophotometer. Fluorescence emission spectra were recorded on a Jobin Yvon-Spex Fluoromax-4 spectrofluorometer. Fluorescence quantum yields (Φ_F) were determined by comparison of the area under the emission curves for solutions of 9-ITPPo and 9-amide porphycene derivatives in acetone with TPP in toluene (Φ_F=0,11)[1] or ATAZPos and TAZPos in acetone with ICG in DMSO (Φ_F=0,12)[2] respectively. The absorbance of both sample and reference solutions were below 0.05 in order to prevent inner filter effects and matched at the excitation wavelength. Emission intensities were corrected for the refractive index of the solvent.

Fluorescence decays were recorded with a time-correlated single photon counting system (Fluotime200, PicoQuant GmbH, Berlin, Germany) equipped with a red sensitive photomultiplier. Excitation was achieved by means of a 375 nm picosecond diode laser working at 10 MHz repetition rate and the photon counting frequency was kept below 1%. Fluorescence lifetimes were determined using PicoQuant *FluoFit 4.6* data analysis software.

The specific $^1O_2$ near-infrared phosphorescence kinetics were detected by means of a customized PicoQuant Fluotime 200 system described in detail elsewhere.[3] The time-resolved emission signals were fitted by Eq. (1):

$$S_t = S_0 \times \frac{\tau_\Delta}{\tau_\Delta - \tau_T}\left(e^{-t/\tau_\Delta} - e^{-t/\tau_T}\right) \qquad \text{Eq. (1)}$$

where S_0 is proportional to Φ_Δ, τ_Δ is the $^1O_2$ lifetime and τ_T is the lifetime of the photosensitizer's triplet state. The Φ_Δ values were determined by comparing S_0 for 9-ITPPo, ATAZPos and TAZPos and a reference photosensitize, TPP (Φ_Δ=0,63).[4]

Triplet lifetimes of the argon fluxed samples were monitored with a home-built nanosecond flash photolysis setup using a Q-switched Nd:YAG laser (Surelite I-10, Continuum) for excitation at 355 nm and a Xe lamp (PTI, 75 W) for probing the transient absorption with right-angle geometry. The analysing beam passed through a dual grating monochromator (mod. 101, PTI) and was detected by a Hamamatsu R928 photomultiplier. The signal was fed to a Lecroy WaveSurfer 454 oscilloscope for digitizing and averaging (typically 10 shots) and finally transferred to a PC computer for data storage and analysis. Kinetic analysis of the individual transients decays afforded the values of τ_T.

1.4 Computational methods

Geometry optimizations of ground states were performed using the DFT method with B3LYP functional at 6-31G(d) level of theory. Gaussian 09 software was used for all calculations[5].

2. Experimental section

9-amino-2,7,12,17-tetraphenylporphycene (9-ATPPo) was prepared in agreement with previously described synthetic procedures.[6] This compound was used as starting reagent for the synthesis of the novel porphycene derivatives described below (Scheme S1).

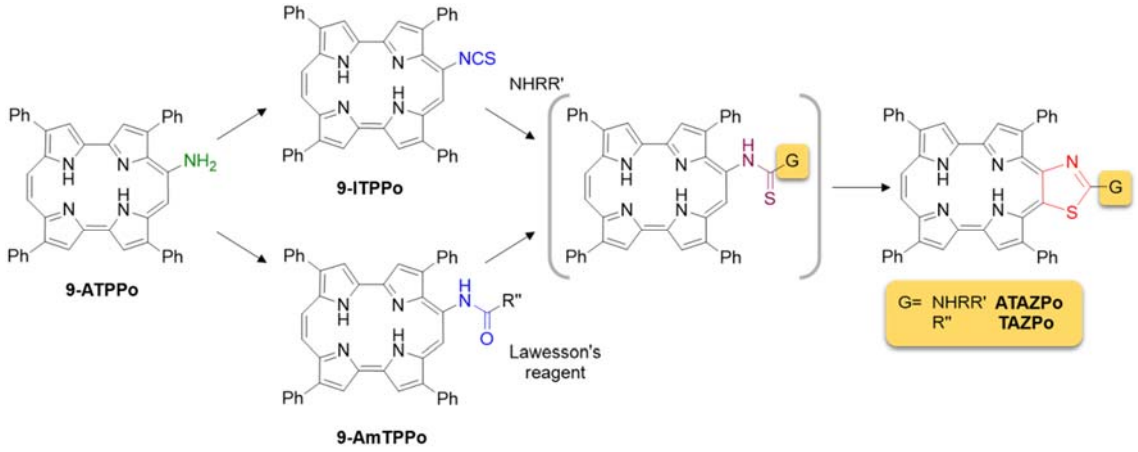

Scheme S1: General synthetic scheme for the preparation of thiazolo[4,5-c]porphycenes

2.1. Synthesis of 9-isothiocyanate-2,7,12,17-tetraphenylporphycene

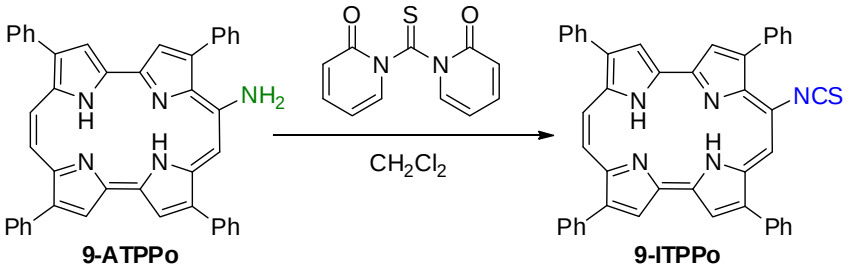

Scheme S2: Synthesis of 9-isothiocyanate-2,7,12,17-tetraphenylporphycene

To a solution of 9-ATPPo (50 mg, $7.5.10^{-2}$ mmol) in CH_2Cl_2 (10 mL) was added 1,1′-thiocarbonyldi-2(1H)-pyridone (53 mg, 3 eq, 0.23 mmol). The mixture was stirred 16h at room temperature. The solvent was evaporated and the mixture was purified by chromatography with silica column eluting with CH_2Cl_2. The product was then crystallized, by dissolving it in toluene (5 mL) and pouring it in acetonitrile (50 mL), to provide a green product (38 mg, $5.6.10^{-2}$ mmol, 75 %). ^{1}H NMR (400 MHz, $CDCl_3$) δ 9.70 – 9.61 (ABq, 2H, J_{AB} = 11.1 Hz), 9.55 (s, 1H), 9.43 (s, 1H), 9.39 (s, 2H), 9.30 (s, 1H), 8.29 – 8.19 (m, 6H), 8.08 – 8.00 (m, 2H), 7.88 – 7.59 (m, 12H), 3.77 (s, 1H), 3.29 (s, 1H). ^{13}C NMR (100 MHz, $CDCl_3$) δ 145.47, 145.15, 144.79, 143.64, 143.08, 142.96, 139.93, 138.03, 137.42, 136.14, 135.75, 135.18, 134.83, 134.03, 133.52, 131.54, 131.51, 131.48, 130.91, 129.47, 129.29, 129.26, 128.73, 128.41, 128.22, 127.94, 127.30, 124.14, 124.07, 118.27, 115.57, 115.16, 114.83. MS (API-ES) Calculated for $C_{45}H_{30}N_5S$ [$(M+H)^+$]: 672.22. Found: *m/z*=672.2. Retention time: 21.49 min.

UV/Vis λ_{max}/nm (ε/$M^{-1}\cdot cm^{-1}$): 399 ($8.8\cdot10^4$), 540 ($4.25\cdot10^3$), 584 ($1.95\cdot10^4$), 643 ($3.0\cdot10^4$), 656 ($2.85\cdot10^4$), 667 ($2.1\cdot10^4$).

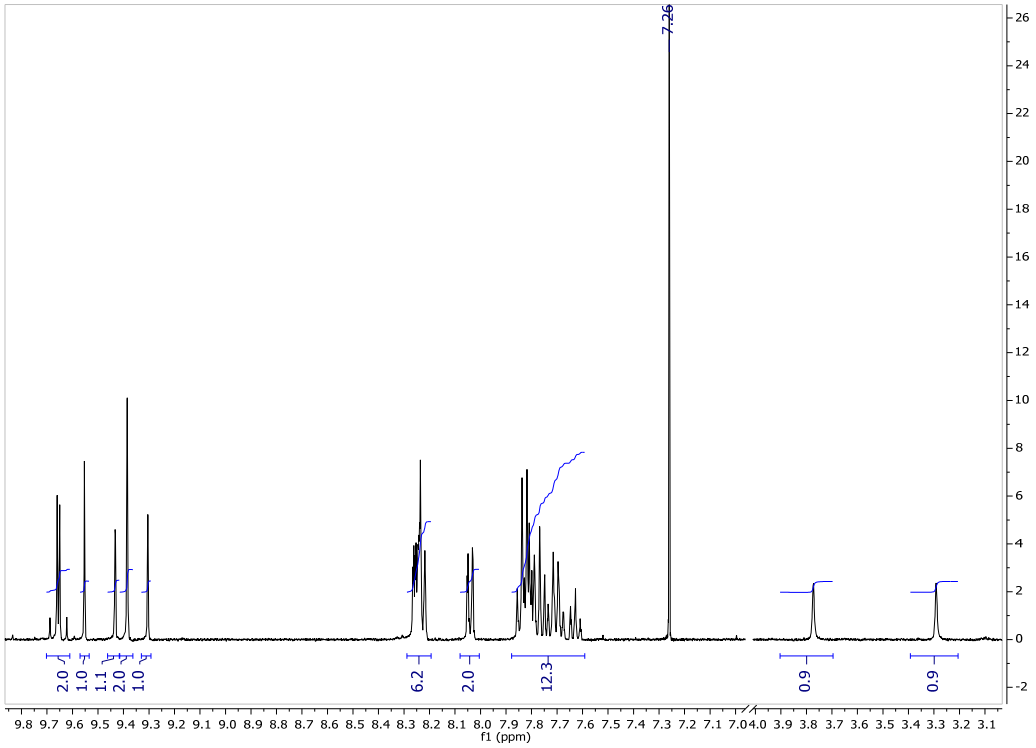

Figure S1: ^{1}H-NMR spectra of 9-ITPPo

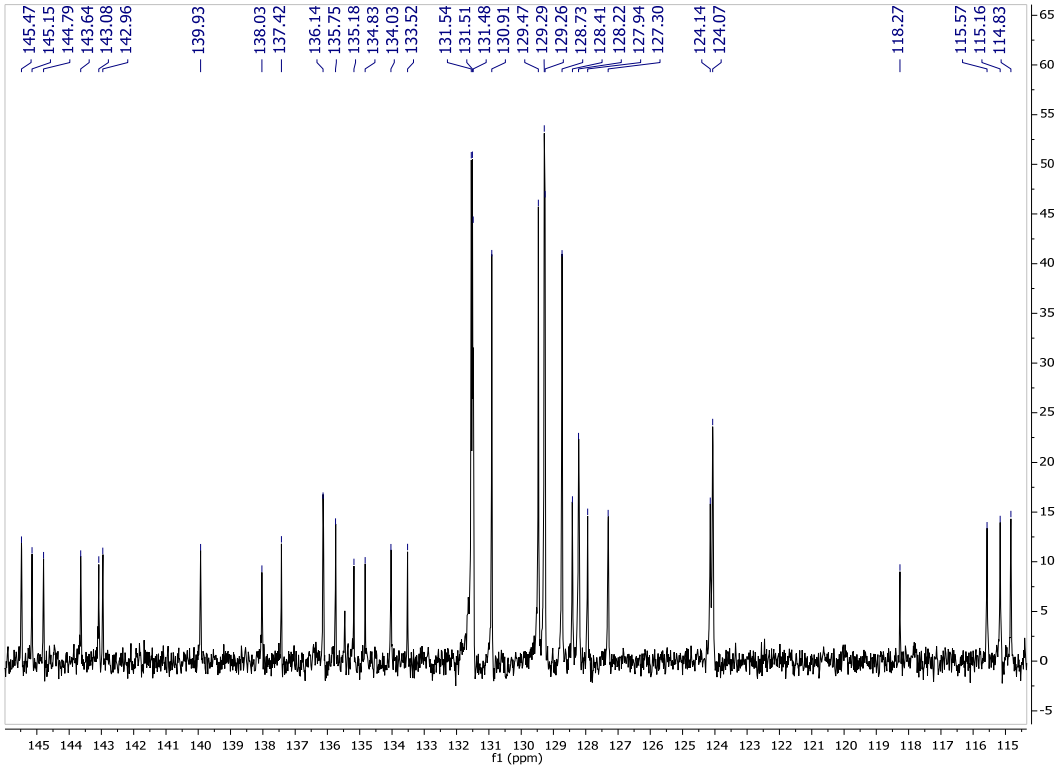

Figure S2: ^{13}C-NMR spectra of 9-ITPPo

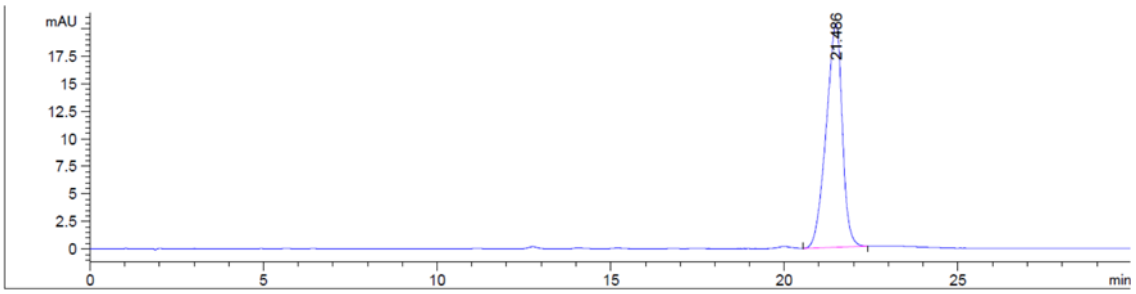

Figure S3: Chromatogram of 9-ITPPo using UV/Vis detection at 400 nm.

2. 2. Synthesis of 2-aminothiazolo[4,5-c]tetraphenylporphycenes

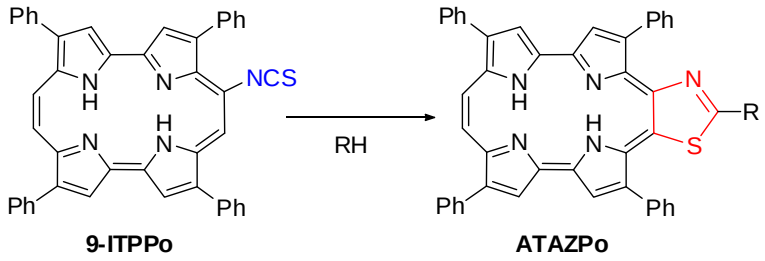

9-ITPPo **ATAZPo**

ATAZPo1: R = -NH_2

ATAZPo2: R = -NH

ATAZPo3: R = -N

ATAZPo4: R = -N NH

ATAZPo5: R = -N O

ATAZPo6: R = -NH

ATAZPo7: R = -NH O 11 N_3

Scheme S3: Synthesis of 2-aminothiazole-fused tetraphenylporphycene derivatives

Synthesis of ATAZPo1

To a solution of 9-isothiocyanate-2,7,12,17-tetraphenylporphycene (9-ITPPo, 5 mg, 7.10^{-3} mmol) in THF (0.5 mL) was added a large excess of ammonium hydroxide 30% (1 mL, 7 mmol). The mixture was stirred 3h at room temperature. Then, water was added and the product was extracted with CH_2Cl_2, the organic layer was dried with anhydrous Na_2SO_4 and evaporated to provide a green product (5mg, 97%). ^{1}H NMR (400 MHz, $CDCl_3$) δ 9.61 (d, J = 11.1 Hz, 1H), 9.49 (d, J = 11.1 Hz, 1H), 9.41 (s, 1H), 9.39 (s, 1H), 9.36 (s, 2H), 8.30 – 8.23 (m, 4H), 8.04 (m, 2H), 7.98 – 7.92 (m, 2H), 7.81 – 7.59 (m, 11H), 7.54 – 7.47 (m, 1H), 6.08 (s, 1H), 5.48 (s, 1H). ^{13}C NMR (100 MHz, $CDCl_3$) δ 165.17, 145.25, 144.74, 143.73, 143.17, 143.10, 143.08, 142.64, 142.28, 141.10, 140.26, 137.78, 136.98, 136.65, 136.33, 135.19, 134.39, 134.11, 131.48, 131.42, 131.38, 131.36, 130.98, 130.95, 130.63, 129.98, 129.40, 129.23, 129.21, 129.14, 129.09, 129.01, 128.70, 128.04, 127.88, 127.82, 127.71, 127.63, 126.37, 125.23, 123.64, 123.59, 123.16, 115.93, 112.2. MS (API-ES) Calculated for $C_{45}H_{30}N_6S$ [$(M+H)^+$]: 687.23. Found: m/z=687.2 Retention time: 7.15 min.

UV/Vis λ_{max}/nm (ε/$M^{-1}\cdot cm^{-1}$): 390 ($1.01\cdot10^5$), 412 ($8.28\cdot10^4$), 583 ($6.1\cdot10^3$), 627 ($2.9\cdot10^4$), 685 ($6.5\cdot10^4$), 745 ($9.3\cdot10^3$).

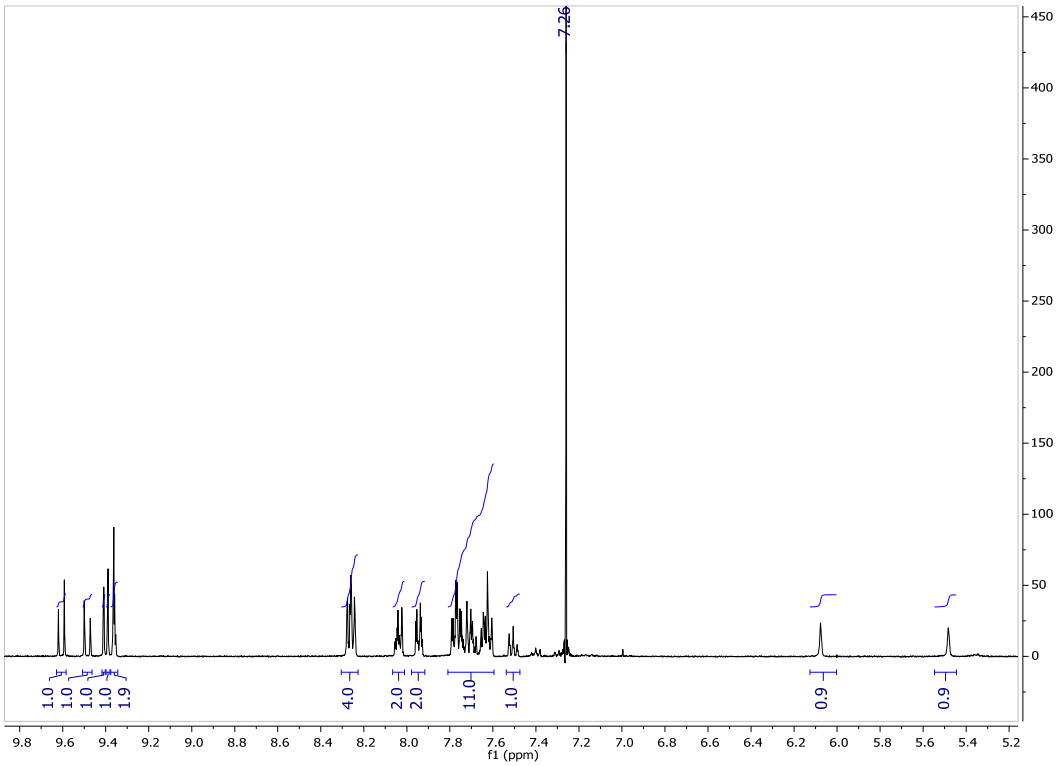

Figure S4: ^{1}H-NMR spectra of ATAZPo1

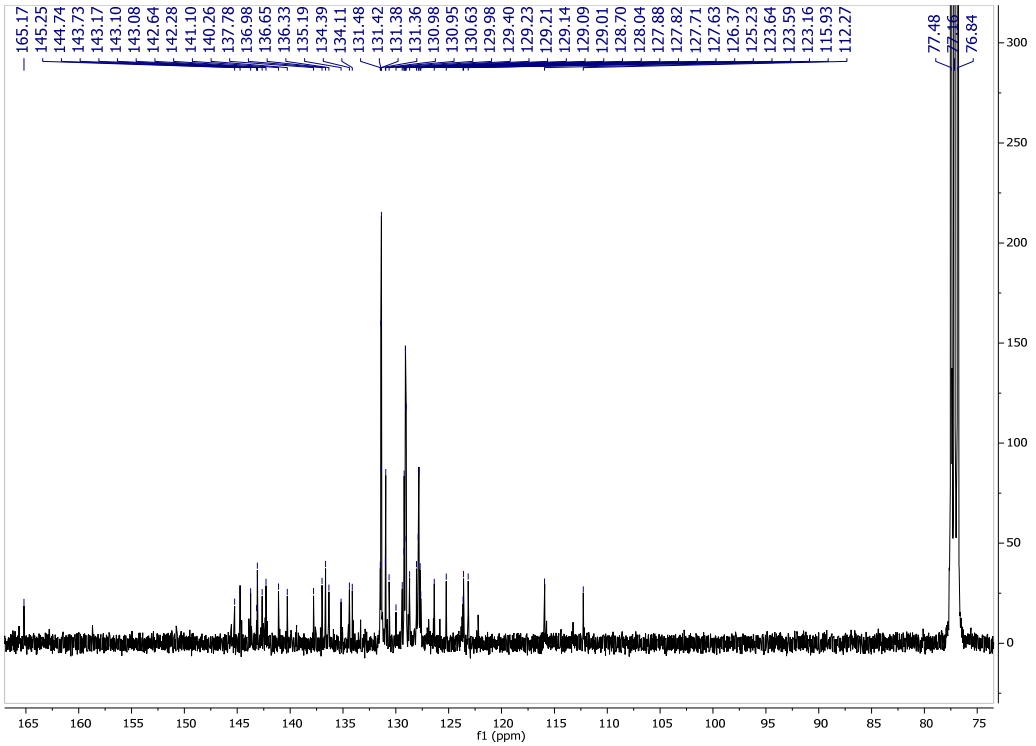

Figure S5: ^{13}C-NMR spectra of ATAZPo1

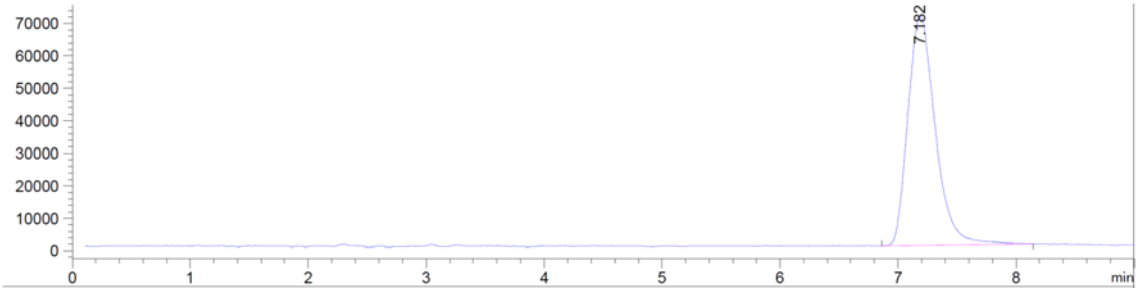

Figure S6: Chromatogram of ATAZPo1 using UV/Vis detection at 400 nm.

Synthesis of ATAZPo2

To a solution of 9-ITPPo (3 mg, 4.10^{-3} mmol) in CH_2Cl_2 (2 mL) was added *n*-butylamine (50 µL, 0.6 mmol, 150 eq). The mixture was stirred 3h at room temperature. Then, water was added and the product was extracted with CH_2Cl_2, the organic layer was dried with anhydrous Na_2SO_4 and evaporated to provide a green product (3 mg, 95%). ^{1}H NMR (400 MHz, $CDCl_3$) δ 9.63 (d, *J* = 11.1 Hz, 1H), 9.54 (d, *J* = 11.1 Hz, 1H), 9.43 (s, 2H), 9.41 (s, 1H), 9.38 (s, 1H), 8.27 (m, 4H), 8.08 (m, 2H), 7.97 – 7.92 (m, 2H), 7.81 – 7.69 (m, 7H), 7.67 – 7.60 (m, 4H), 7.51 (m, 1H), 5.92 (s, 1H), 5.31 (s, 1H), 5.11 (s, 1H), 3.23 (m, 2H), 1.42 – 1.32 (m, 4H), 0.95 (t, *J* = 7.3 Hz, 3H). ^{13}C NMR (100 MHz, $CDCl_3$) δ 164.05, 145.04, 144.09, 143.89, 143.42, 142.76, 142.65, 142.58, 140.65, 139.62, 137.75, 136.84, 136.56, 136.52, 135.72, 134.42, 133.87, 131.42, 131.37, 131.12, 130.90, 129.31, 129.10, 129.04, 128.74, 128.04, 127.94, 127.80, 127.75, 126.60, 125.58, 123.64, 123.47, 123.22, 115.74, 112.80, 77.48, 77.16, 76.84, 44.51, 31.87, 20.14, 14.01. MS (API-ES) Calculated for $C_{45}H_{30}N_6S$ [$(M+H)^+$]: 743.29. Found: *m*/*z*=743.2. Retention time: 14.50 min.

UV/Vis λ_{max}/nm (ε/$M^{-1}\cdot cm^{-1}$): 394 ($1.06\cdot10^5$), 414 ($8.6\cdot10^4$), 584 ($1.0\cdot10^4$), 632 ($3.4\cdot10^4$), 699 ($6.8\cdot10^4$), 743 ($2.0\cdot10^4$).

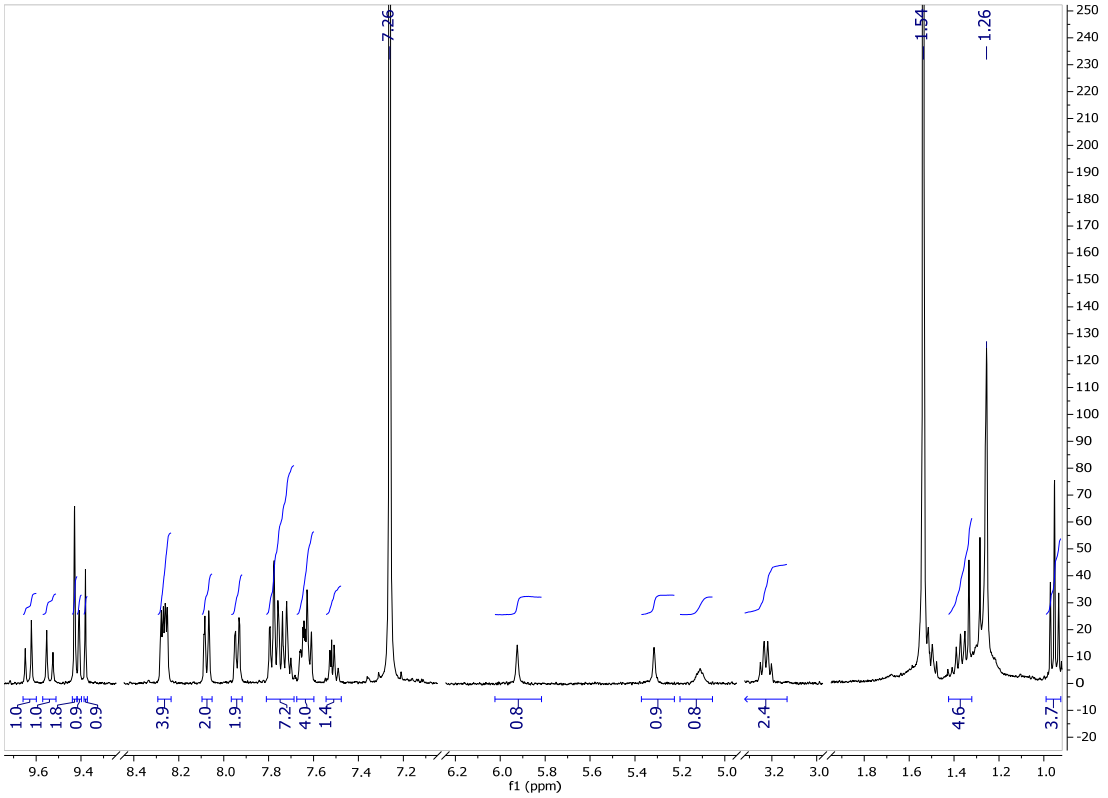

Figure S7: [1]H-NMR spectra of ATAZPo2

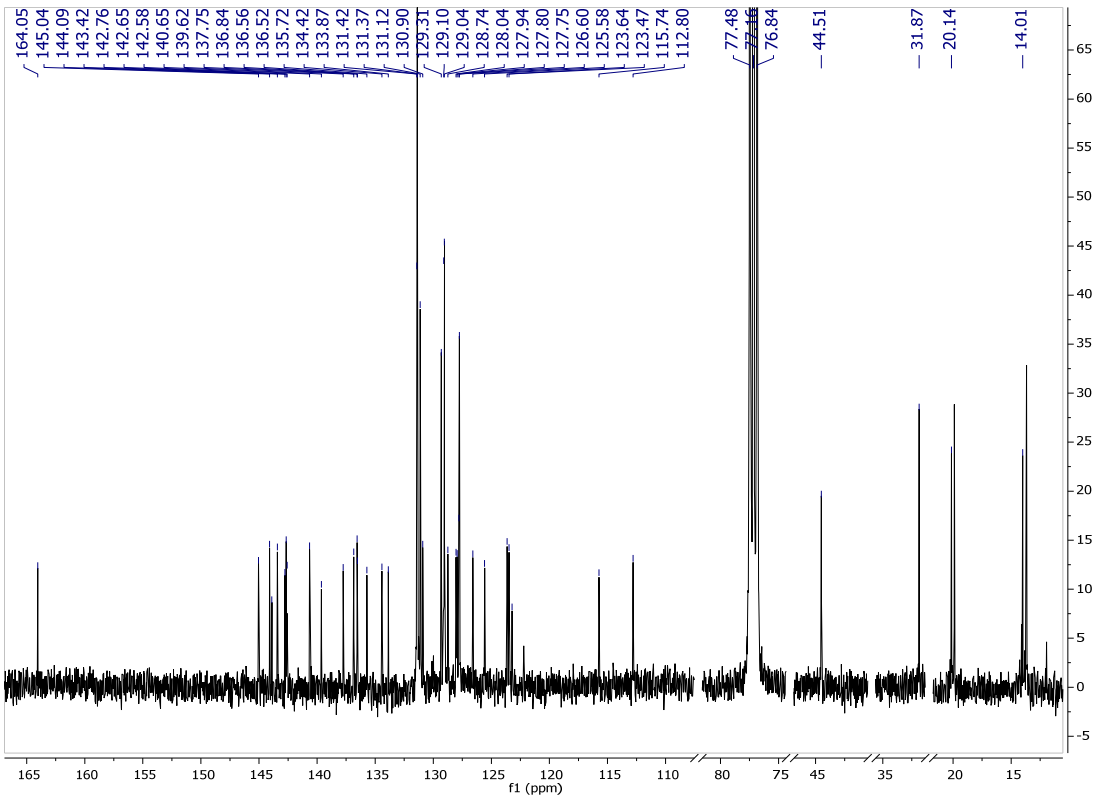

Figure S8: [13]C-NMR spectra of ATAZPo2

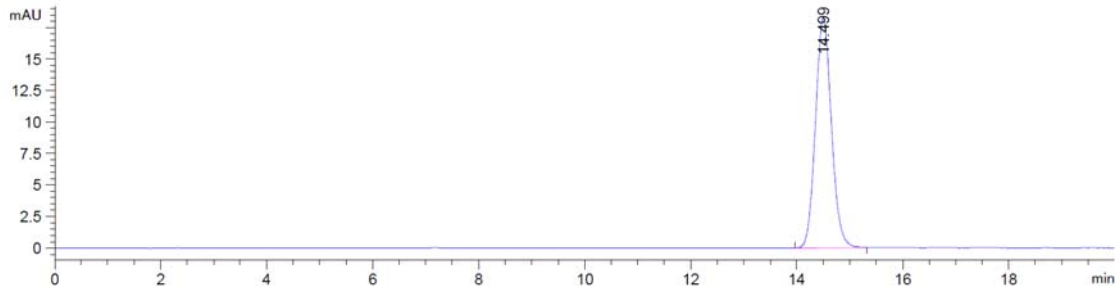

Figure S9: Chromatogram of ATAZPo2 using UV/Vis detection at 400 nm.

Synthesis of ATAZPo3

To a solution of 9-ITPPo (3 mg, 4.10^{-3} mmol) in CH_2Cl_2 (2 mL) was added diethylamine (4 µL, 0.04 mmol, 10 eq). The mixture was stirred 5h at room temperature. Then, water was added and the product was extracted with CH_2Cl_2, the organic layer was dried with anhydrous Na_2SO_4 and evaporated to provide a green product (3 mg, 95%). ^{1}H NMR (400 MHz, $CDCl_3$) δ 9.61 (d, *J* = 11.1 Hz, 1H), 9.49 (d, *J* = 11.1 Hz, 1H), 9.41 (d, *J* = 1.0 Hz, 1H), 9.39 (s, 1H), 9.37-9.36 (s, 2H), 8.28-8.24 (m, 4H), 8.04-8.02 (m, 2H), 7.98 – 7.92 (m, 2H), 7.81 – 7.59 (m, 12H), 7.56 – 7.48 (m, 2H), 6.09 (s, 1H), 5.49 (s, 1H), 3.36 (q, *J* = 7.2 Hz, 4H), 1.13 (t, *J* = 7.1 Hz, 6H). ^{13}C NMR (100 MHz, $CDCl_3$) 165.01, 145.10, 144.59, 143.59, 143.59, 142.95, 142.93, 140.92, 140.92, 137.61, 136.82, 136.48, 136.18, 135.03, 134.25, 133.96, 131.25, 131.19, 130.77, 130.48, 129.04, 128.92, 128.84, 128.54, 127.88, 127.71, 127.65, 127.54, 126.20, 125.06, 123.44, 115.77, 112.11, 52.78, 29.69. MS (API-ES) Calculated for $C_{45}H_{30}N_6S$ $[(M+H)^+]$: 743.29. Found: *m*/*z*=743.2. Retention time: 20.03 min.

UV/Vis λ_{max}/nm ($\varepsilon/M^{-1}\cdot cm^{-1}$): 387 ($9.6\cdot10^4$), 405 ($8.7\cdot10^4$), 424 ($8.7\cdot10^4$), 583 ($8.3\cdot10^3$), 632 ($1.2\cdot10^4$), 702 ($6.4\cdot10^4$), 763 ($1.4\cdot10^4$).

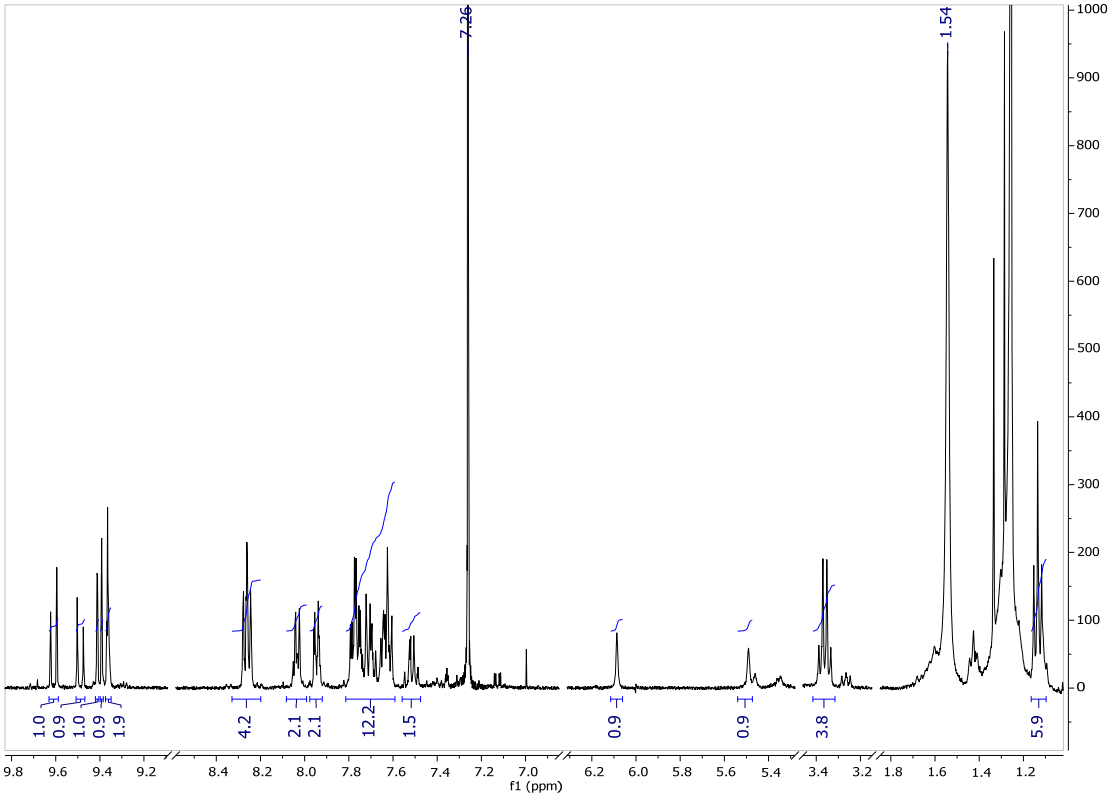

Figure S10: ^{1}H-NMR spectra of ATAZPo3

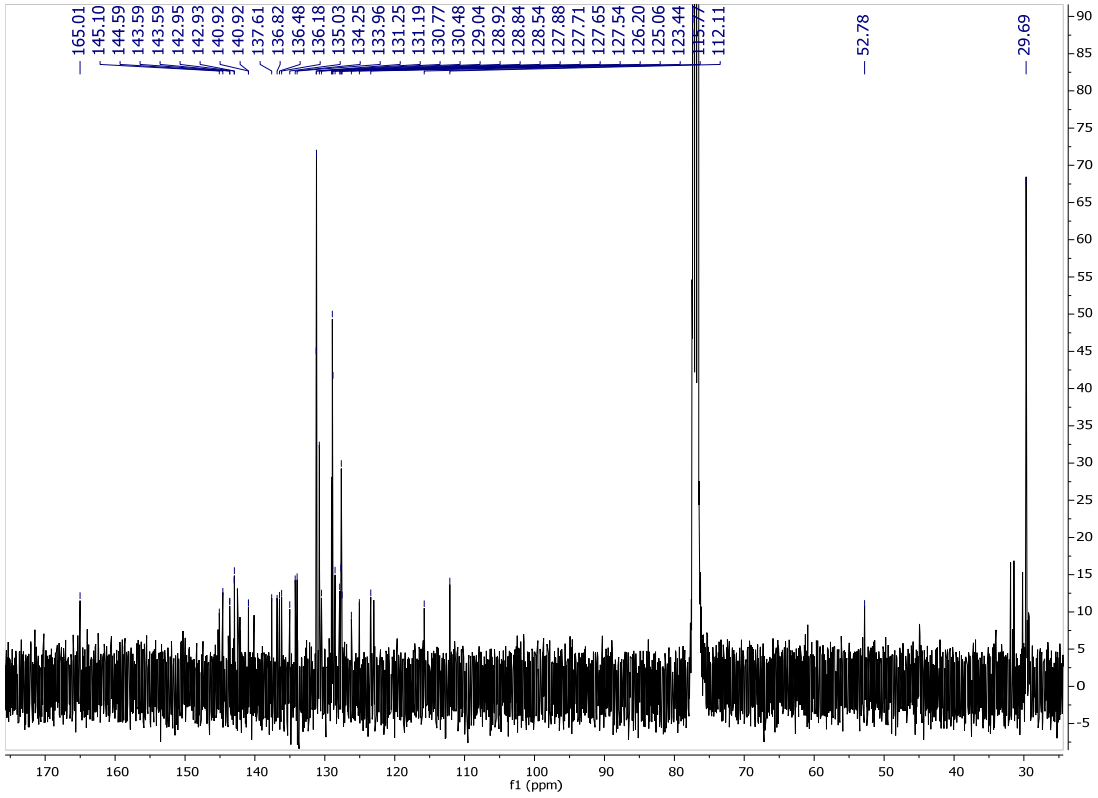

Figure S11: ^{13}C-NMR spectra of ATAZPo3

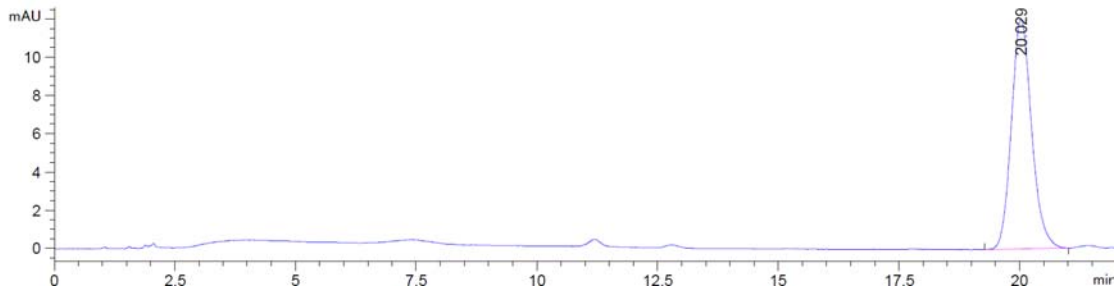

Figure S12: Chromatogram of ATAZPo3 using UV/Vis detection at 400 nm.

Synthesis of ATAZPo4

To a solution of 9-ITPPo (5 mg, $7.5.10^{-3}$ mmol) in CH_2Cl_2 (2 mL) was added piperazine (20 mg, 0.2 mmol, 30 eq). The mixture was stirred 3h at room temperature. Then, water was added and the product was extracted with CH_2Cl_2, the organic layer was dried with anhydrous Na_2SO_4 and evaporated, the product was purified by chromatography with silica column eluting with cyclohexane:toluene gradient starting from v:v=3:1 to v:v=0:1 to provide a green product (4 mg, 90%). The NMR spectrum shows two conformers at room temperature. ^{1}H NMR (400 MHz, $CDCl_3$) δ 9.61 (d, J = 11.2, 1H), 9.51 (d, J = 11.1, 1H), 9.43 – 9.36 (m, 4H), 8.26 (m, 4H), 8.04 (m, 2H), 7.96 (m, 2H), 7.84 – 7.60 (m, 11H), 7.49 (m, 1H), 5.94 (s, 1H), 5.33 (s, 1H), 3.47 – 3.29 (m, 4H), 2.95 – 2.89 (m, 1H), 2.78 (m, 2H), 2.62 (m, 2H). ^{13}C NMR (100 MHz, $CDCl_3$) δ 165.67, 165.46, 144.86, 144.13, 143.00, 142.89, 142.41, 142.23, 139.41, 136.64, 136.38, 135.91, 135.83, 134.56, 133.63, 133.60, 131.24, 131.20, 131.16, 130.84, 130.77, 129.14, 128.93, 128.88, 128.63, 127.81, 127.69, 126.15, 123.61, 123.13, 112.67, 50.86, 48.88, 45.79, 45.55. MS (API-ES) Calculated for $C_{49}H_{38}N_7S$ $[(M+H)^+]$: 755.94, $[(M+3H_2O+2H)^+]$:783.96. Found: *m*/*z*=784.2. Retention time: 5.74 min.

UV/Vis λ_{max}/nm (ε/$M^{-1}\cdot cm^{-1}$): 392 ($1.05\cdot10^5$), 398 ($1.07\cdot10^5$), 420 ($8.9\cdot10^4$), 583 ($7.0\cdot10^3$), 625 ($3.6\cdot10^4$), 688 ($6.8\cdot10^4$), 744 ($1.8\cdot10^4$).

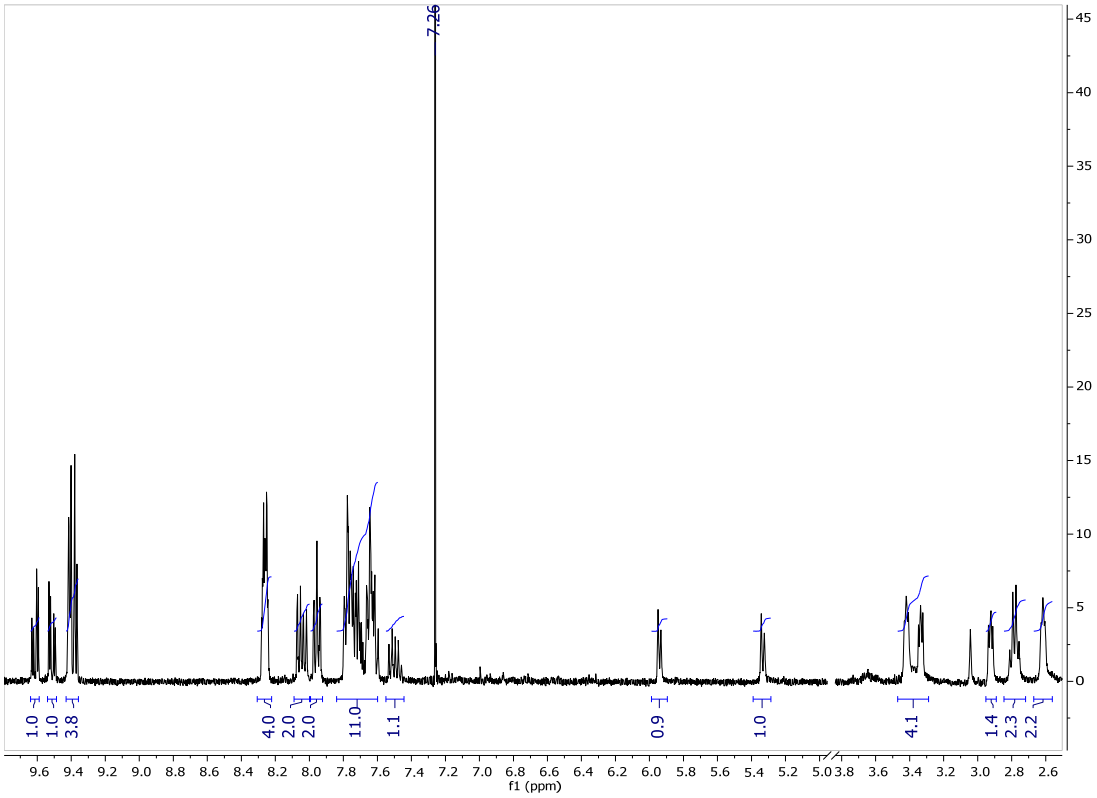

Figure S13: [1]H-NMR spectra of ATAZPo4

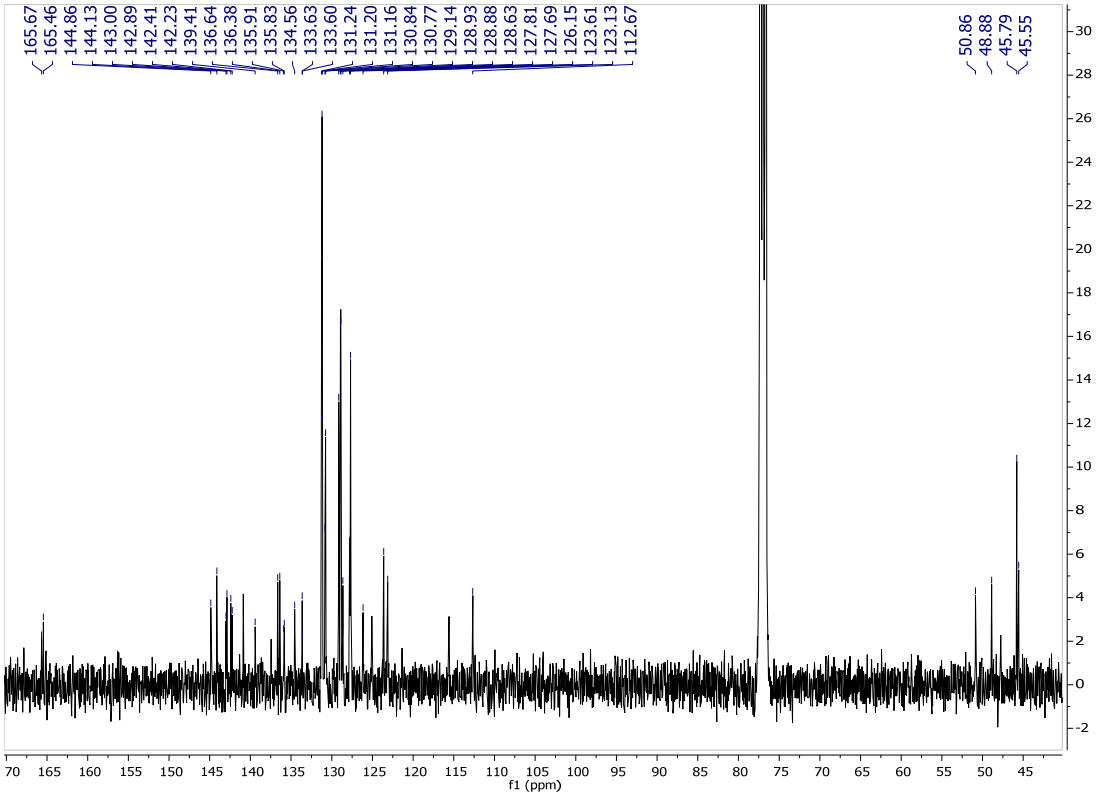

Figure S14: [13]C-NMR spectra of ATAZPo4

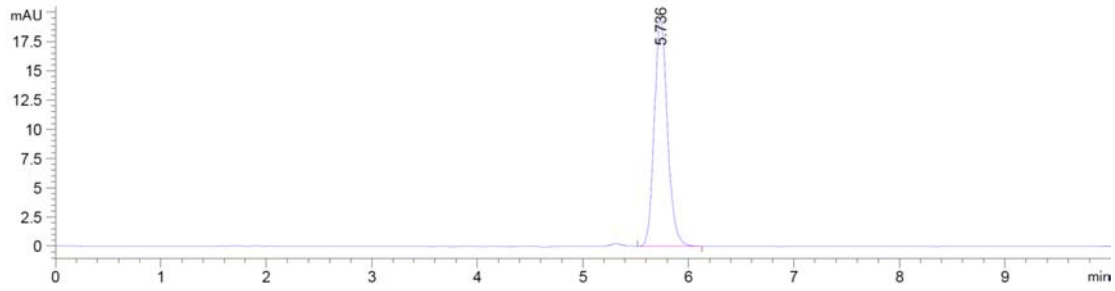

Figure S15: Chromatogram of ATAZPo4 using UV/Vis detection at 400 nm.

Synthesis of ATAZPo5

To a solution of 9-ITPPo (5 mg, $7.5.10^{-3}$ mmol) in CH_2Cl_2 (2 mL) was added morpholine (20 mg, 0.2 mmol, 30 eq). The mixture was stirred 3h at room temperature. Then, water was added and the product was extracted with CH_2Cl_2, the organic layer was dried with anhydrous Na_2SO_4 and evaporated, the product was purified by chromatography with silica column eluting with cyclohexane:toluene gradient starting from v:v=3:1 to v:v=0:1 to provide a green product (4 mg, 90%). ^{1}H NMR (400 MHz, $CDCl_3$) 9.62 (d, J = 11.1 Hz, 1H), 9.53 (d, J = 11.1 Hz, 1H), 9.44 – 9.40 (m, 2H), 9.40 (s, 1H), 9.38 (s, 1H), 8.32 – 8.17 (m, 4H), 8.09 – 7.99 (m, 2H), 7.99 – 7.92 (m, 2H), 7.86 – 7.57 (m, 11H), 7.49 (m, 1H), 5.90 (s, 1H), 5.28 (s, 1H), 3.76 (t, J = 4.9 Hz, 4H), 3.36 (t, J = 4.9 Hz, 4H). ^{13}C NMR (100 MHz, $CDCl_3$) δ 165.51, 145.02, 144.33, 143.59, 143.12, 142.97, 142.26, 140.92, 139.25, 137.39, 136.57, 136.33, 136.09, 134.78, 133.43, 131.24, 131.20, 131.17, 130.78, 129.17, 128.94, 128.89, 128.68, 127.83, 127.77, 127.70, 126.19, 125.19, 123.67, 123.23, 115.60, 112.86, 66.33, 47.90. MS (API-ES) Calculated for $C_{49}H_{37}N_6OS$ [$(M+H)^+$]: 757.27, Found: m/z=757.2. Retention time: 14.74 min.

UV/Vis λ_{max}/nm ($\varepsilon/M^{-1}\cdot cm^{-1}$): 386 ($5.7\cdot10^4$), 398 ($5.8\cdot10^4$), 414 ($5.2\cdot10^4$), 583 ($4.7\cdot10^3$), 624 ($2.0\cdot10^4$), 688 ($3.7\cdot10^4$), 740 ($1.2\cdot10^4$).

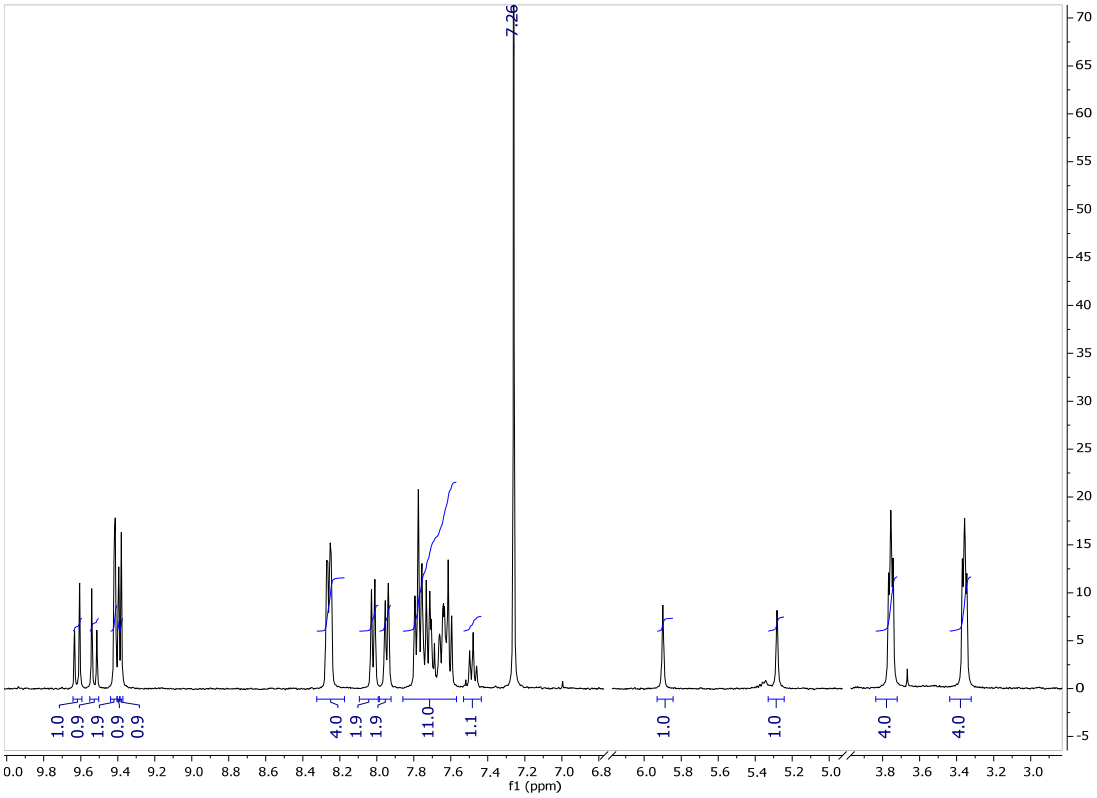

Figure S16: [1]H-NMR spectra of ATAZPo5

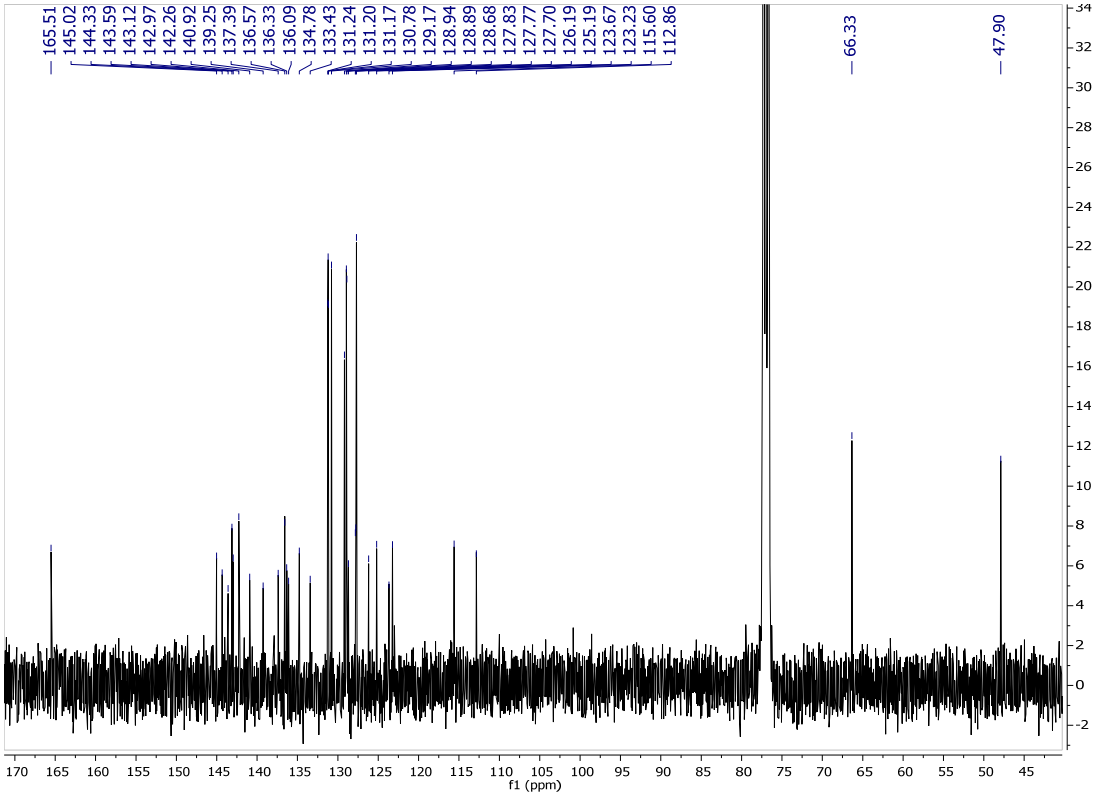

Figure S17: [13]C-NMR spectra of ATAZPo5

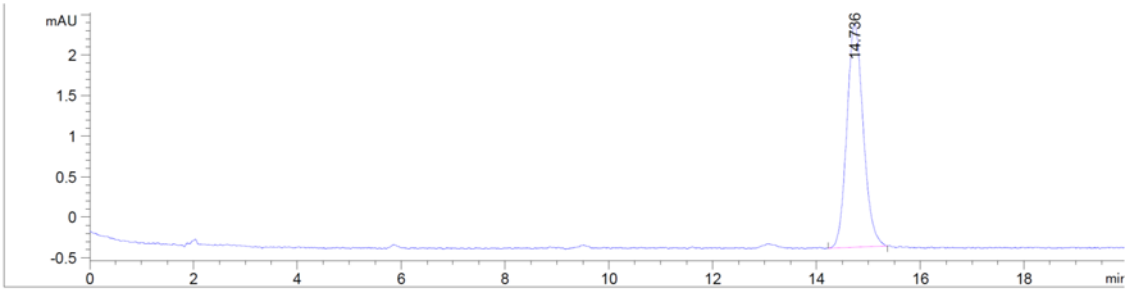

Figure S18: Chromatogram of ATAZPo5 using UV/Vis detection at 400 nm.

Synthesis of ATAZPo6

To a solution of 9-ITPPo (1 mg, $1.5 \cdot 10^{-3}$ mmol) in CH_2Cl_2 (2 mL) was added aniline (5µl, 0.04 mmol, 30 eq). The mixture was stirred 24h at room temperature. Then, water was added and the product was extracted with CH_2Cl_2, the organic layer was dried with anhydrous Na_2SO_4 and evaporated, the product was purified by chromatography with silica column eluting with cyclohexane:toluene gradient starting from v:v=3:1 to v:v=0:1 to provide a green product (0.8 mg, 80%).^{1}H NMR (400 MHz, $CDCl_3$) δ 9.62 (d, J = 11.0 Hz, 1H), 9.54 (d, J = 11.1 Hz, 1H), 9.42 (m, 2H), 9.41 (m, 1H), 9.39 (m, 1H), 8.29 – 8.24 (m, 4H), 8.15 (m, 2H), 7.99 (m, 2H), 7.81 – 7.69 (m, 11H), 7.66 (m, 2H), 7.59 (m, 1H), 7.53 (m, 3H), 5.99 (s, 1H), 5.32 (m, 2H). MS (API-ES) Calculated for $C_{51}H_{34}N_6S$ [$(M+H)^+$]: 762.92, Found: m/z=762.9. Retention time: 14.42 min.

UV/Vis λ_{max}/nm ($\varepsilon/M^{-1} \cdot cm^{-1}$): 386 ($7.6 \cdot 10^4$), 418 ($7.4 \cdot 10^4$), 586 ($9.0 \cdot 10^3$), 633 ($2.7 \cdot 10^4$), 692 ($5.5 \cdot 10^4$), 750 ($1.2 \cdot 10^4$).

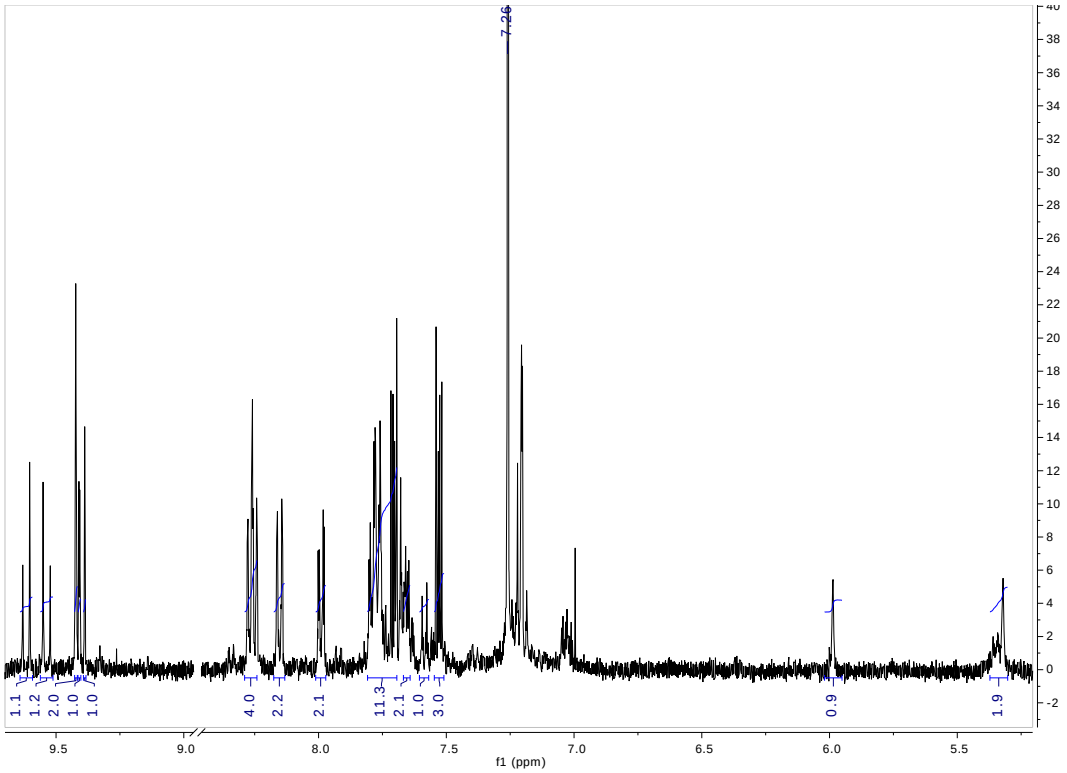

Figure S19: ^{1}H-NMR spectra of ATAZPo6

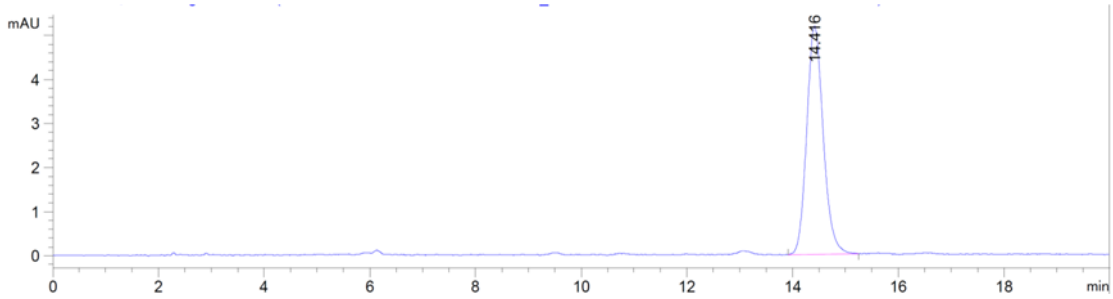

Figure S20: Chromatogram of ATAZPo6 using UV/Vis detection at 400 nm.

Synthesis of ATAZPo7

To a solution of 9-ITPPo (5 mg, $7.5.10^{-3}$ mmol) in dichloromethane (2 mL) was added O-(2-aminoethyl)-O′-(2-azidoethyl)nonaethylene glycol (NH_2-PEG-N_3, 9 mg, $1.5.10^{-2}$ mmol, 2 eq). The mixture was stirred 3h at room temperature. Then, water was added and the product was extracted with CH_2Cl_2, the organic layer was dried with anhydrous Na_2SO_4 and evaporated, the product was purified by chromatography with silica column eluting with cyclohexane:toluene gradient starting from v:v=3:1 to v:v=0:1 to provide a green product (6 mg, 85%). ^{1}H NMR (400 MHz, $CDCl_3$) δ 9.63 (d, J = 11.1 Hz, 1H), 9.53 (d, J = 11.1 Hz, 1H), 9.42 (d, J = 0.8 Hz, 2H), 9.40 (d, J = 1.2 Hz, 1H), 9.37 (s, 1H), 8.26 (m, 4H), 8.07 – 8.00 (m, 2H), 7.96 – 7.91 (m,

2H), 7.81 – 7.57 (m, 11H), 7.52 – 7.46 (m, 1H), 6.34 (s, 1H), 5.90 (s, 1H), 5.32 (s, 1H), 4.11 (s, 2H), 3.66 – 3.51 (m, 44H), 3.41 – 3.31 (m, 4H). ^{13}C NMR (100 MHz, $CDCl_3$) δ 173.26, 163.85, 143.93, 143.74, 143.06, 142.59, 142.56, 140.84, 139.28, 137.64, 136.68, 136.41, 136.17, 135.75, 134.23, 133.66, 132.13, 132.03, 131.94, 131.92, 131.25, 131.20, 130.86, 129.13, 128.94, 128.88, 128.53, 127.92, 127.77, 127.63, 127.58, 126.26, 125.38, 123.51, 123.20, 115.48, 70.48, 70.46, 70.44, 70.43, 62.13, 50.62. MS (API-ES) Calculated for $C_{69}H_{77}N_9O_{11}S$ [$(M+H)^+$]: 1240.55, $C_{69}H_{77}N_9O_{11}SNa$ [$(M+Na)^+$]: 1262.54, Found: *m/z*=1240.4, 1262.4. Retention time: 8.15 min.

UV/Vis λ_{max}/nm ($\varepsilon/M^{-1}\cdot cm^{-1}$): 388 ($1.0\cdot10^5$), 415 ($8.4\cdot10^4$), 586 ($7.8\cdot10^3$), 628 ($3.2\cdot10^4$), 693 ($6.6\cdot10^4$), 748 ($1.7\cdot10^4$).

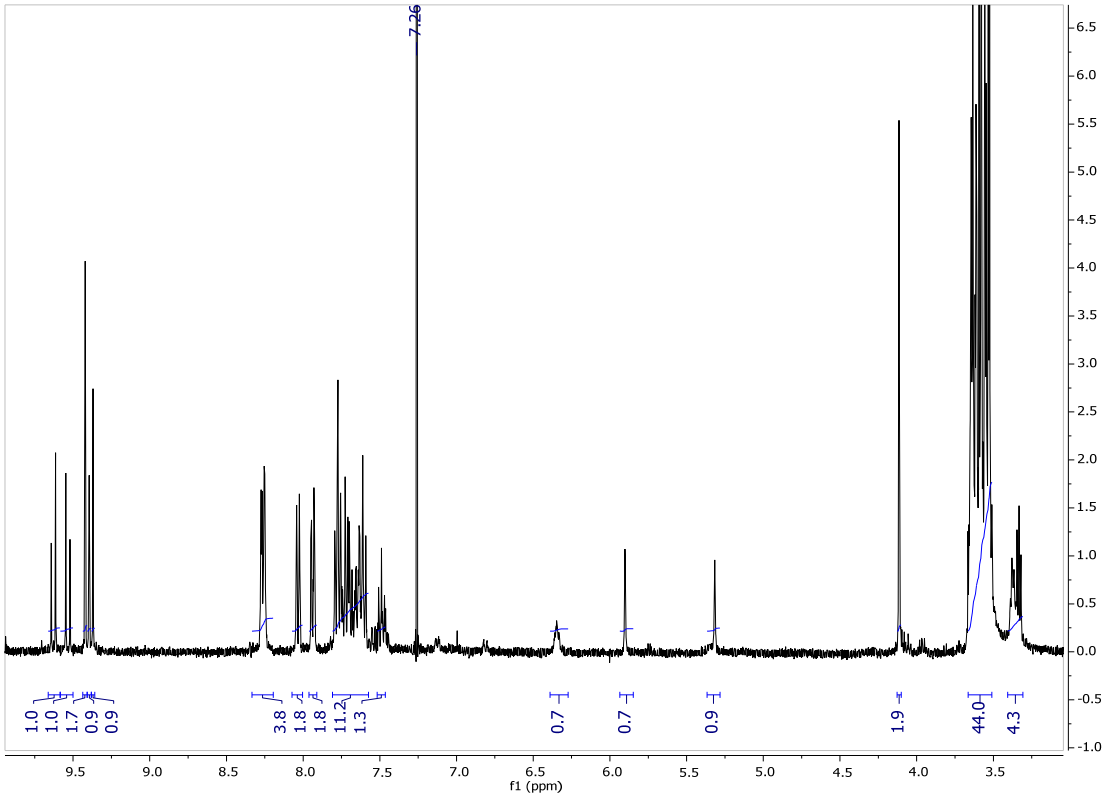

Figure S21: ^{1}H-NMR spectra of ATAZPo7

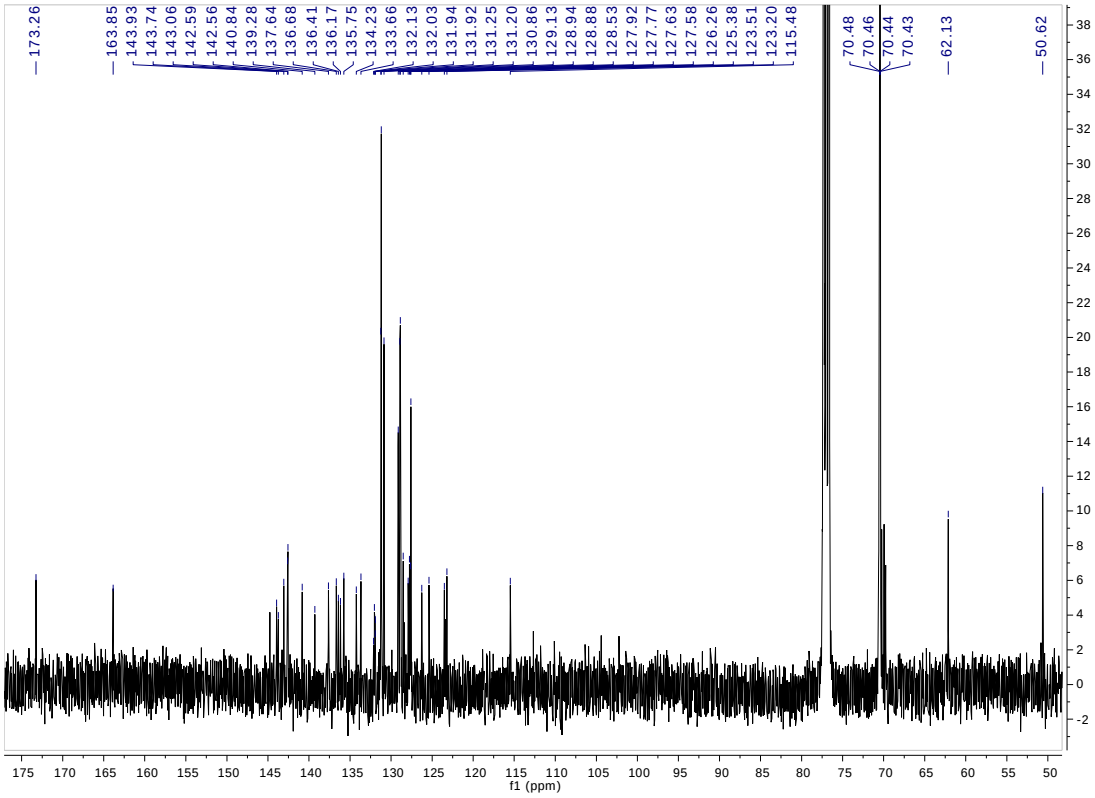

Figure S22: ^{13}C-NMR spectra of ATAZPo7

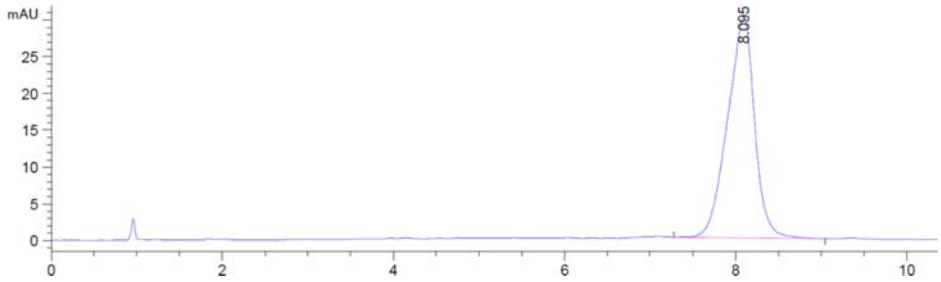

Figure S23: Chromatogram of ATAZPo7 using UV/Vis detection at 400 nm.

.

2. 3. Synthesis of 9-benzamido-2,7,12,17-tetraphenylporphycene

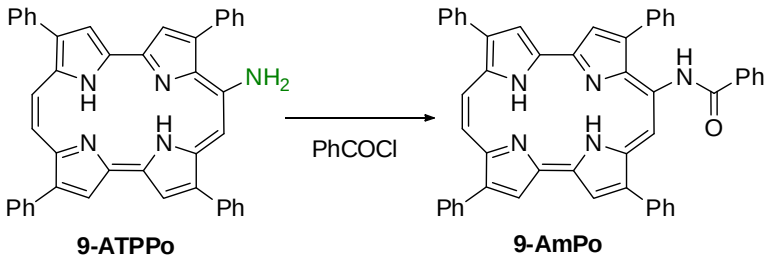

Scheme S4: Synthesis of 9-benzamido-2,7,12,17-tetraphenylporphycene (9-AmPo)

To a solution of 9-ATPPo (3 mg, $4.8 \cdot 10^{-3}$ mmol) in 5 mL of THF were added 2 µl of benzoyl chloride ($1.2 \cdot 10^{-2}$ mmol, 2.5 eq) and $4.8 \cdot 10^{-3}$ mmol of pyridine (1 eq). The mixture was stirred for 2 h. Then, water was added and the pH was adjusted to 12 with NaOH. The product was extracted with CH_2Cl_2, the organic layer was dried with anhydrous Na_2SO_4 and evaporated. Finally the product was purified by thin layer silica chromatography eluting with CH_2Cl_2 to provide a blue-greenish product (2.5 mg, 80%). ^{1}H NMR (400 MHz, $CDCl_3$) δ 10.52 (s, 1H), 9.85 (d, *J* = 11.2 Hz, 1H), 9.78 (d, *J* = 11.2 Hz, 1H), 9.65 (s, 1H), 9.61 (s, 1H), 9.55 (s, 1H), 9.52 (s, 1H), 9.45 (s, 1H), 8.48 (d, *J* = 7.5 Hz, 2H), 8.30 (ddd, *J* = 10.5, 8.1, 1.4 Hz, 4H), 8.19 – 8.12 (m, 1H), 8.00 – 7.92 (m, 2H), 7.81 (ddd, *J* = 12.7, 7.6, 5.4 Hz, 6H), 7.71 – 7.64 (m, 3H), 7.60 – 7.50 (m, 5H), 7.42 (dt, *J* = 16.8, 7.7 Hz, 5H), 4.76 (s, 1H), 4.39 (s, 1H). ^{13}C NMR (100 MHz, $CDCl_3$) 166.07, 145.59, 145.17, 144.54, 143.77, 142.23, 141.02, 140.85, 136.41, 136.31, 135.84, 134.77, 134.65, 134.11, 133.84, 131.62, 131.39, 131.33, 130.11, 129.17, 129.02, 128.99, 128.38, 127.91, 127.84, 127.77, 127.11, 127.00, 126.07, 124.06, 123.82, 123.51, 115.50, 114.09, 113.24. MS (API-ES) Calculated for $C_{51}H_{35}N_5O$ $[(M+H)^+]$: 734.87, $C_{102}H_{74}N_{10}O_2$ $[(2M+H)^+]$: 1468.7, Found: *m*/*z*=734.2, 1468.4. Retention time: 8.15 min.

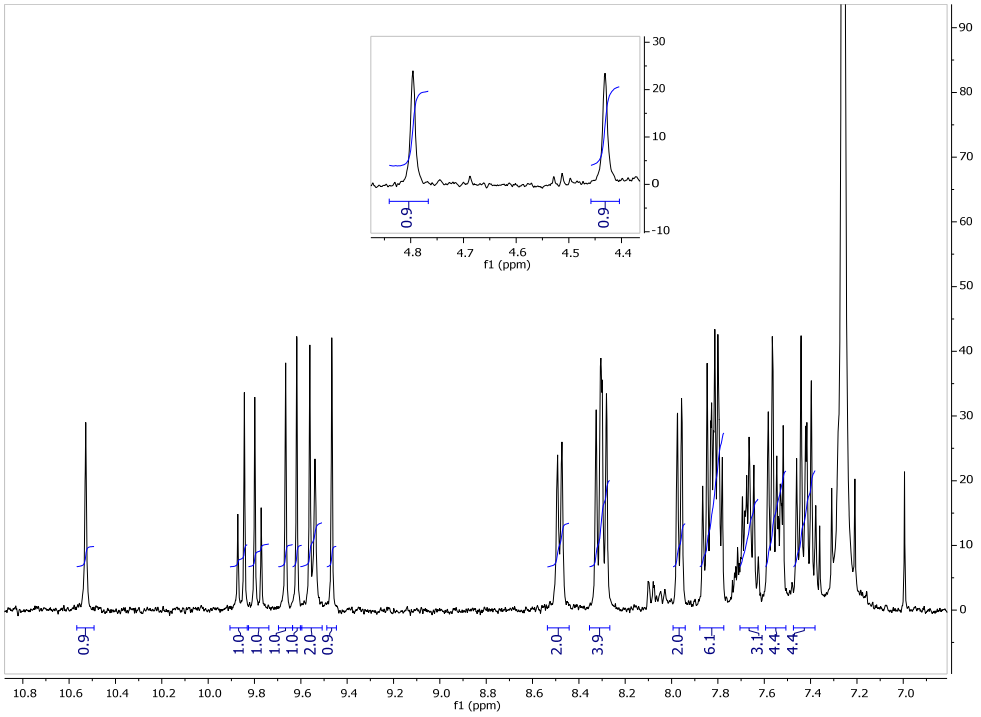

Figure S24: ^{1}H-NMR spectra of 9-AmPo

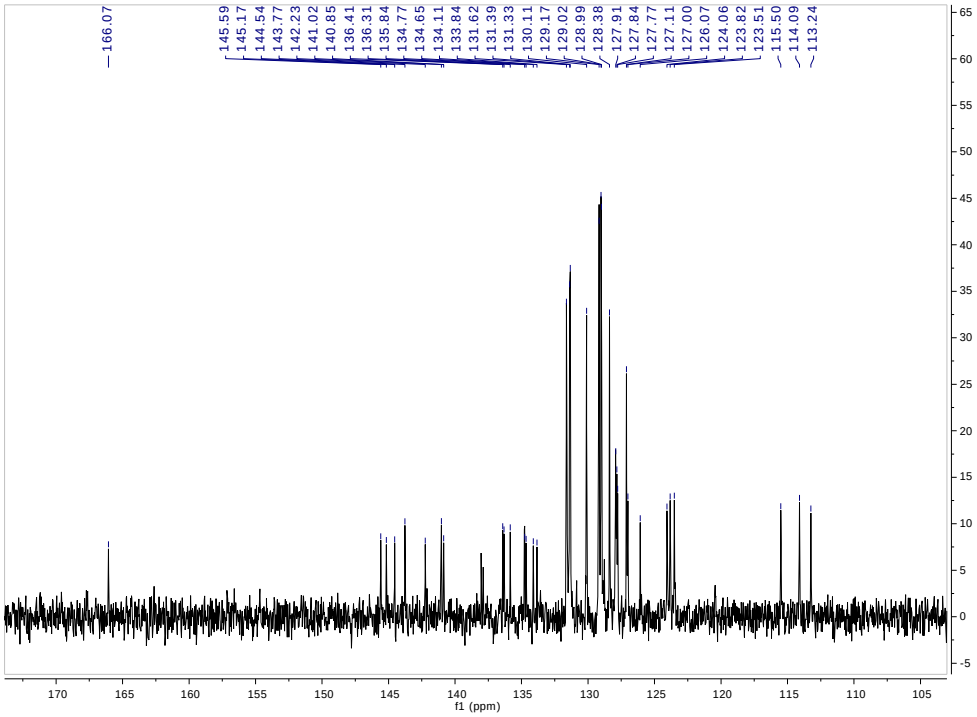

Figure S25: ^{13}C-NMR spectra of 9-AmPo

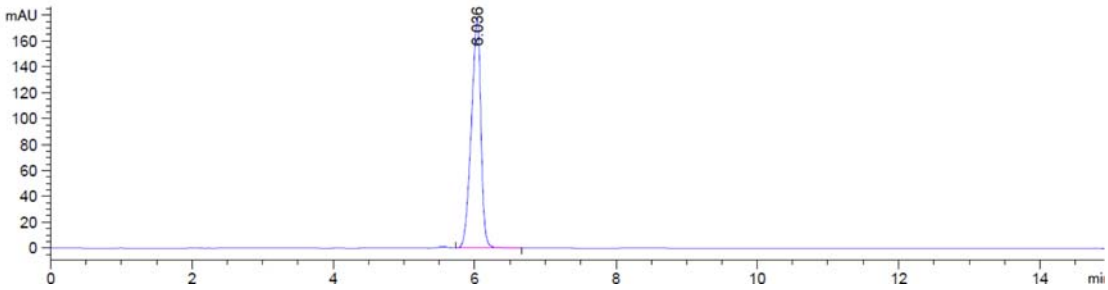

Figure S26: Chromatogram of 9-AmPo using UV/Vis detection at 400 nm.

2.4 Synthesis of 2-phenylthiazolo[4,5-c]tetraphenylporphycene

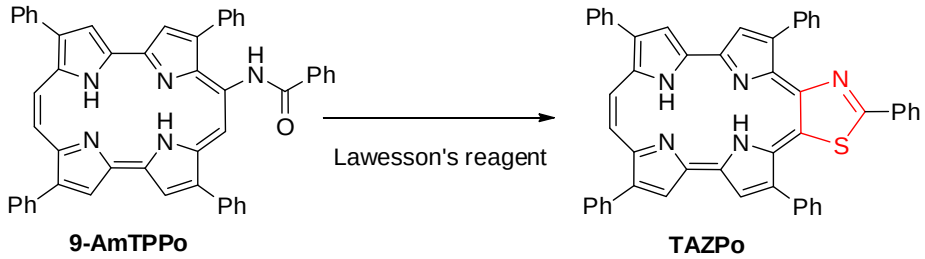

Scheme S5: Synthesis of of 2-phenylthiazolo[4,5-c]tetraphenylporphycene (TAZPo)

To a solution of 9-AmPo (3 mg, $4.0 \cdot 10^{-3}$ mmol) in 0.4 mL of toluene were added 4 mg of the Lawesson's reagent ($1.0 \cdot 10^{-2}$ mmol, 2.5 eq). The mixture was stirred and heated at 120 ºC using microwaves for 1.5 h. Then, the solvent was reduced under reduced pressure and the crude was purified by thin layer silica chromatography eluting with toluene to provide a blue-greenish

product (2.5 mg, 81%). ^{1}H NMR (400 MHz, $CDCl_3$) δ 9.51 (s, 2H), 9.43 (d, J = 1.0 Hz, 1H), 9.38 (s, 1H), 9.36 (d, J = 1.0 Hz, 1H), 9.35 (s, 1H), 8.21 – 8.17 (m, 4H), 8.09 – 8.04 (m, 2H), 7.94 (m, 3H), 7.76 – 7.69 (m, 8H), 7.68 – 7.64 (m, 4H), 7.62 – 7.57 (m, 4H), 5.99 (s, 1H), 5.32 (s, 1H). ^{13}C NMR (100 MHz, $CDCl_3$) 174.32, 144.81, 144.71, 142.56, 141.83, 140.54, 138.98, 137.42, 137.39, 136.89, 136.06, 135.98, 133.81, 132.14, 131.18, 131.07, 130.50, 129.45, 129.00, 128.77, 128.07, 127.87, 127.68, 127.09, 126.50, 126.24, 124.29, 123.78, 115.04, 114.72, 114.66. MS (API-ES) Calculated for $C_{51}H_{34}N_5S$ $[(M+H)^+]$: 748.9, $C_{102}H_{67}N_{10}S_2$ $[(2M+H)^+]$: 1496.8, Found: *m*/*z*=748.2, 1496.4. Retention time: 3.37 min.

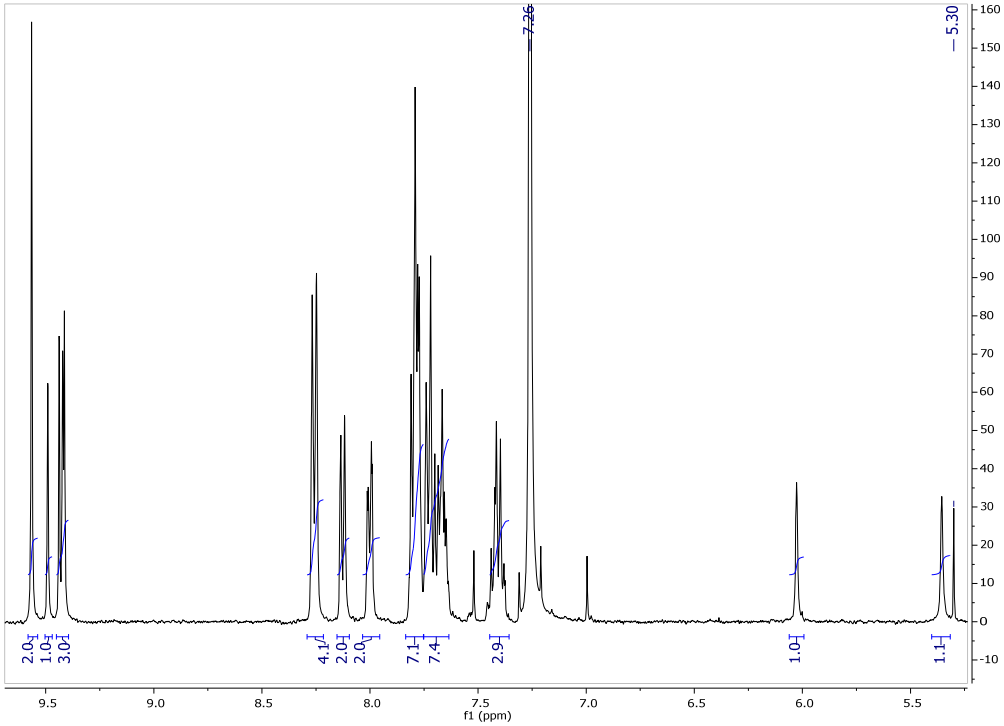

Figure S27: ^{1}H-NMR spectra of TAZPo.

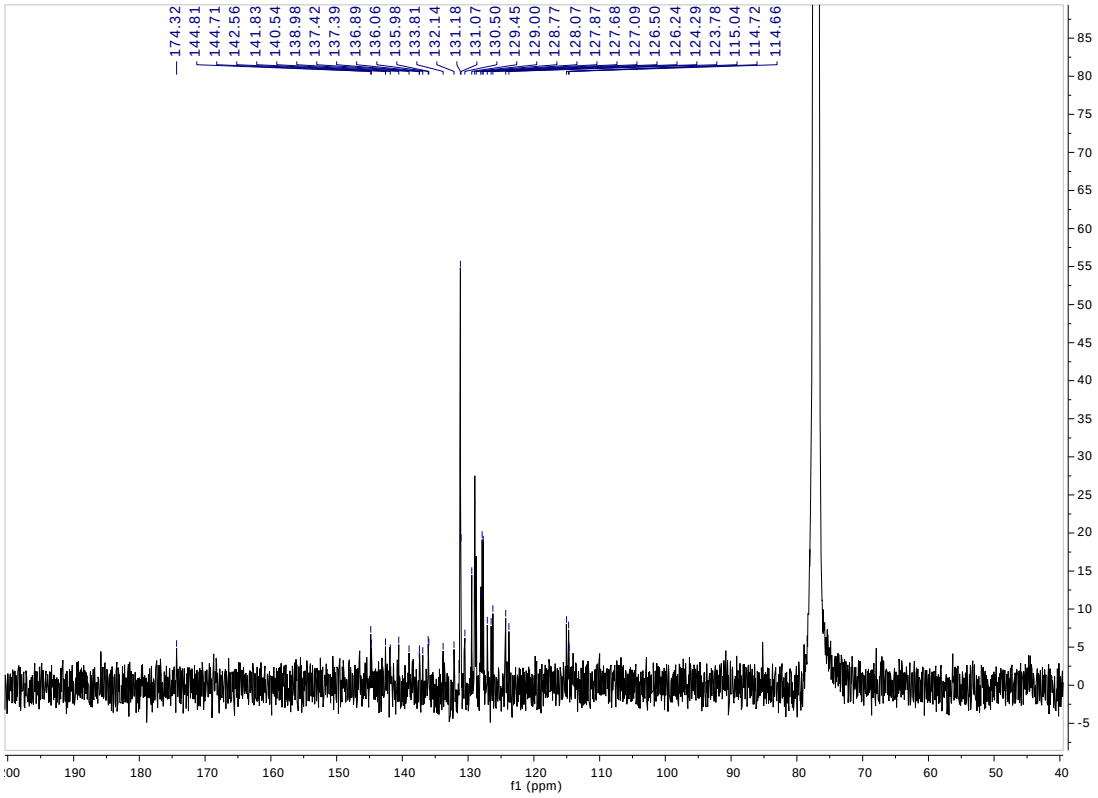

Figure S28: ^{13}C-NMR spectra of TAZPo

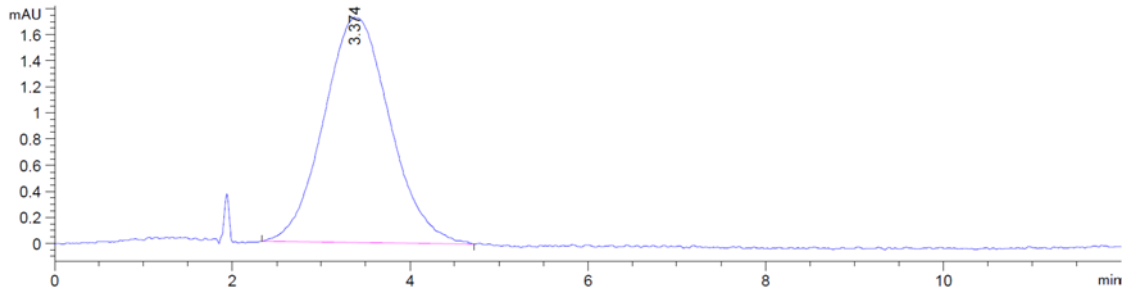

Figure S29: Chromatogram of TAZPo using UV/Vis detection at 400 nm.

2.5 Synthesis of tetraethylenglycol alkyl-thiol stabilized gold nanoclusters

This synthesis was adapted from previously described synthesis of tri- and hexaethylenglycol alky-thiol stabilized gold nanoclusters with some modifications.[7] Briefly, 30 mg of 23-mercapto-3,6,9,12-tetraoxatricosan-1-ol (90 µmol) and 3.3 mg of 1-amino-3,6,9,12-tetraoxatricosane-23-thiol (10 µmol) were mixed with 10 mg of tetracloroauric acid trihydrate (30 µmol) in 7.0 mL of MeOH. 0.6 mL of a freshly prepared solution of $NaBH_4$ (1.3 M) was added at an input speed of 4.8 mL/h under stirring. The mixture was stirred at room temperature during 2.5 h and then the solvent was removed under reduced pressure. Next, the remaining crude was dispersed in 15 mL of a 2:1 water:ethanol mixture and purified by dialysis twice (10h, 900 mL). The aqueous solution was basified using a 0.1 M solution of KOH and extracted

several times with $CHCl_3$. The organic layers were dried over anhydrous Na_2SO_4 and the solvent was removed under reduced pressure. Finally, the brownish solid powder was suspended in 20 mL of absolute EtOH.

2.6 Labelling procedure of gold nanoclusters

100 μL of 9-ITPPo (100 μM) in toluene were gently added to 2 mL of AuNCs (2.9 μM) in ethanol. The mixture was stirred at room temperature for 24 h and several absorption spectra were recorded at different times (Figure S30). After the reaction completion, the solvent removed under reduced pressure. Next, the greenish powder was redispersed in water and purified by successive water dialysis.

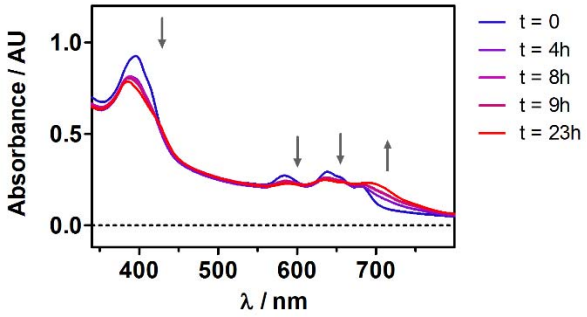

Figure S30: Time evolution of the absorption spectra of 9-ITPPo upon binding to AuNCs.

2.7 Labelling procedure of bovine serum albumin

20 μL of 9-ITPPo (16 mM) were added to a stirred solution of bovine serum albumin (BSA, 5 mg, 0.08 μmol) in a sodium bicarbonate/sodium carbonate buffer (250 mL, pH 9.4). The reaction vessel was protected from light and stirred for 36 h at room temperature. The bioconjugate was purified using the acetone precipitation method previously reported by Hamblin *et al.*[8]. Briefly, the crude bioconjugate preparations were diluted with 1.5 mL of bicarbonate/carbonate buffer and 20 mL of acetone at 4 ºC were slowly added. After 5 h, the green suspension was centrifuged at 4000*g* and washed several times with acetone until colourless supernatant. Then, the pellet was redissolved in 20 mL of PBS and exhaustively dialyzed against 1 L of PBS for 3 days in order to remove all traces of acetone.

3. Additional results

3.1 TEM examination of AuNCs

For size determination, a single drop (15 μL) of the EtOH solution of the gold nanoclusters was placed onto a copper grid coated with a carbon film. The grid was left to dry in air at room temperature. TEM analysis was carried out in a JEOL 2010F microscope working at 200 kV. The particle size distribution of the gold nanoclusters was evaluated from several micrographs by means of an automatic image analyser software (Figure S31).

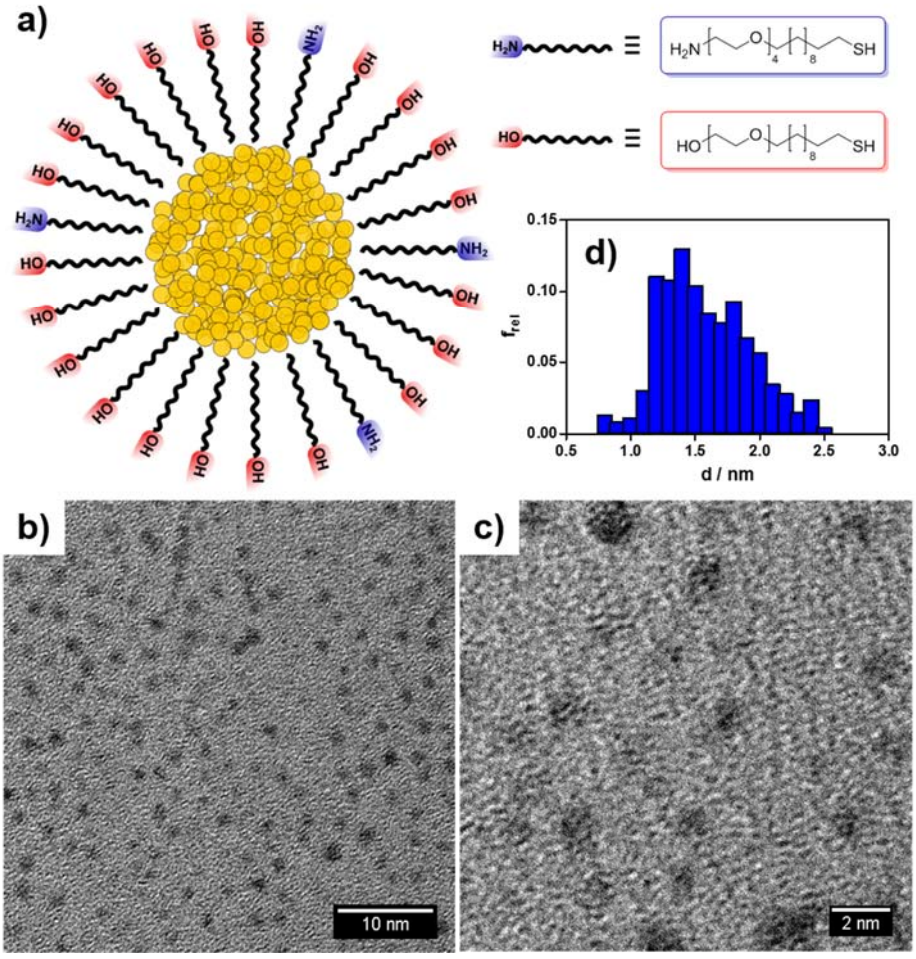

Figure S31: a) Schematic representation of tetraethylenglycol alkyl-thiol stabilized gold nanoclusters (TEG-AuNCs). b) TEG-AuNCs micrography at 120000X. c) TEG-AuNCs micrography at 500000X and d) particle size distribution.

3.2 Time evolution of the absorption spectra of 9-ITPPo upon reaction with *n*-butylamine

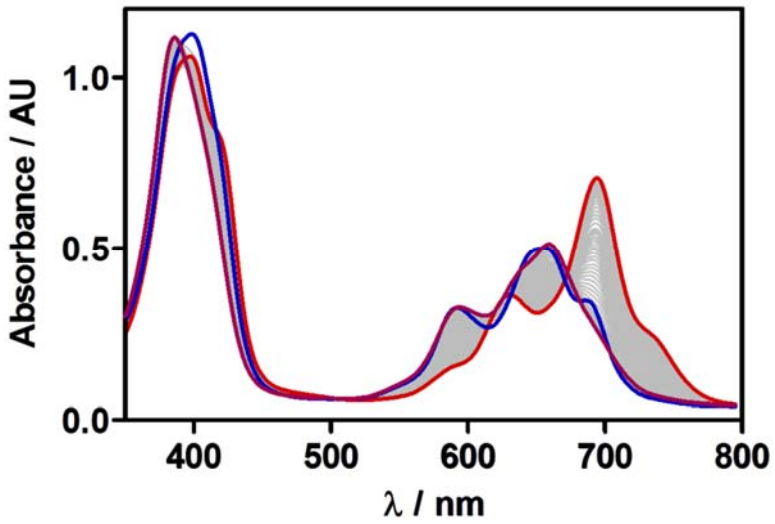

Figure S32: Time evolution of the absorption spectra of a mixture of 9-ITPPo (0.015 mM) and ***n***-butylamine (3 mM) in toluene. The blue line corresponds to the absorption spectra at time 0 (previous to the addition of *N*-butylamine), the green line, the absorption of the intermediate (namely, 9-TUPo) and the red line, the absorption spectra of the sample 60 h later.

3.3 ^{1}H-NMR evolution of 9-ITPPo upon reaction with *n*-butylamine

The evolution of the reaction between 9-ITPPo and *n*-butylamine was characterised by means on ^{1}H-NMR spectroscopy. ^{1}H-NMR spectra were recorded at different steps: **A)** ^{1}H-NMR of 9-ITPPo in $CDCl_3$ prior to the addition of *n*-butylamine, **B)** 10 minutes after the addition of *n*-butylamine and **C)** 24 h after the addition (Figure S33).

A) ^{1}H NMR (400 MHz, $CDCl_3$) δ 9.70 – 9.61 (ABq, 2H, J_{AB} = 11.1 Hz), 9.55 (s, 1H), 9.43 (s, 1H), 9.39 (s, 2H), 9.30 (s, 1H), 8.29 – 8.19 (m, 6H), 8.08 – 8.00 (m, 2H), 7.88 – 7.59 (m, 12H).

B) ^{1}H NMR (400 MHz, $CDCl_3$) δ 9.81 (s, 1H), 9.69 (d, J = 11 Hz, 1H), 9.61 (d, J = 11 Hz, 1H), 9.41 (m, 4H), 8.25 (t, J = 7.3 Hz, 4H), 8.06 (d, J = 7.5 Hz, 2H), 7.91 (m, 1H), 7.85 – 7.63 (m, 11H).

C) ^{1}H NMR (400 MHz, $CDCl_3$) δ 9.63 (d, J = 11.1 Hz, 1H), 9.54 (d, J = 11.1 Hz, 1H), 9.43 (s, 2H), 9.41 (s, 1H), 9.38 (s, 1H), 8.27 (m, 4H), 8.08 (m, 2H), 7.97 – 7.92 (m, 2H), 7.81 – 7.69 (m, 7H), 7.67 – 7.60 (m, 4H), 7.51 (m, 1H).

^{1}H chemical shifts and integrals of **B)** are consistent with the formation of the 9-thiourea derivative.

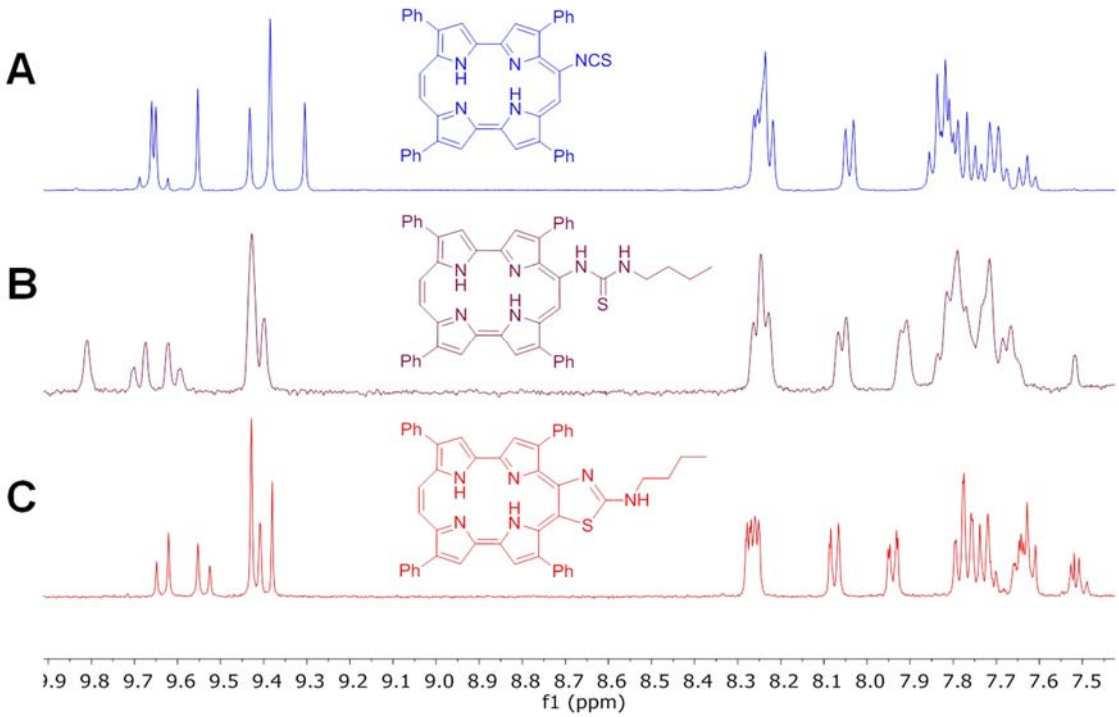

Figure S33: ^{1}H-NMR of a mixture of 9-ITPPo and *n*-butylamine in $CDCl_3$. Spectra were recorded at different time intervals: A) 1H-NMR of 9-ITPPo in $CDCl_3$ prior to the addition of *n*-butylamine, B) 10 minutes after the addition of *n*-butylamine and C) 24 h after the addition.

3.3 Absorption spectrum of ATAZPo derivatives

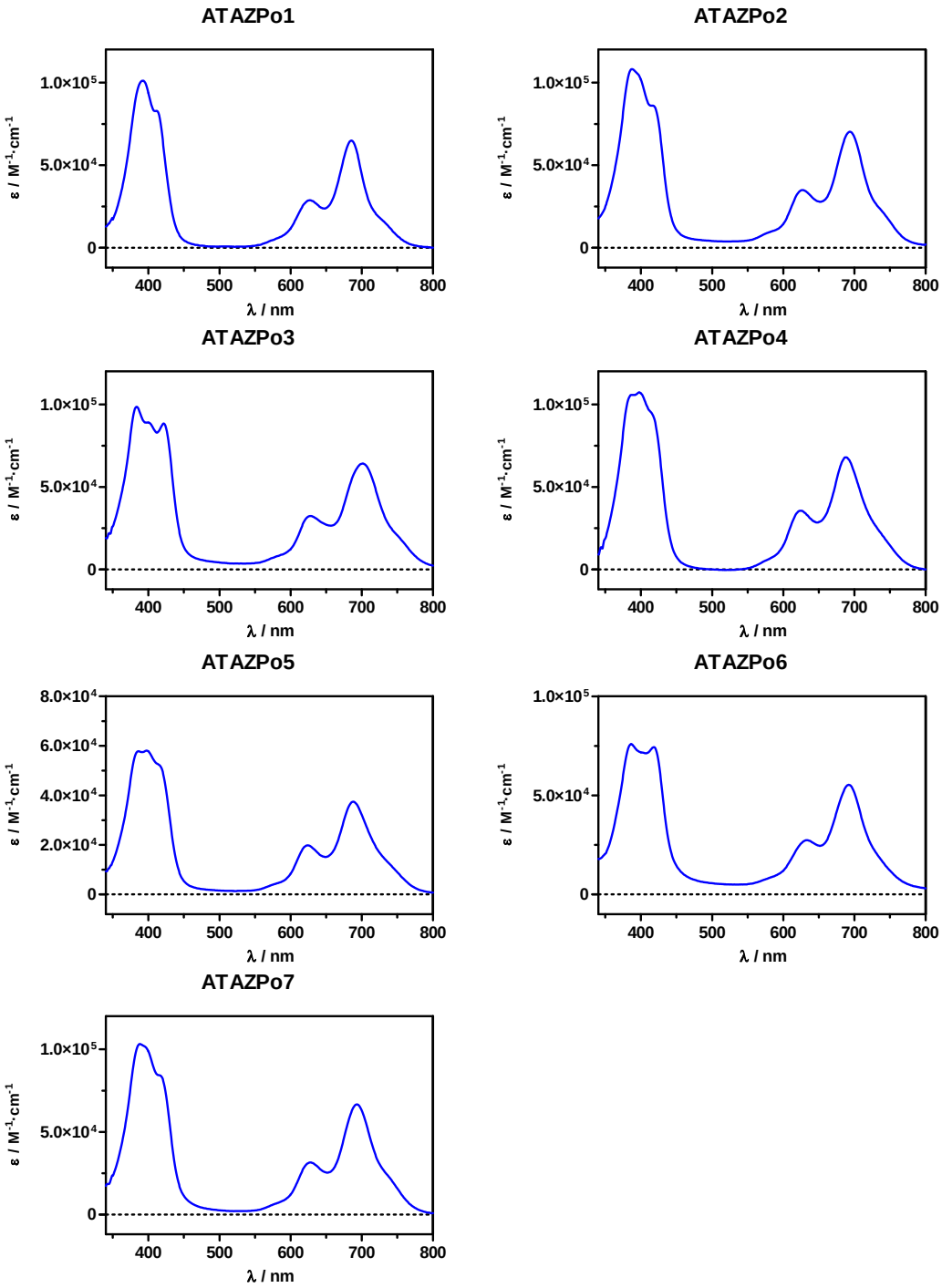

Figure S34: Absorption spectrum of ATAZPo derivatives in acetone

3.3 Phosphorescence decays at 1275 nm for 9-ITPPo and ATAZPo2

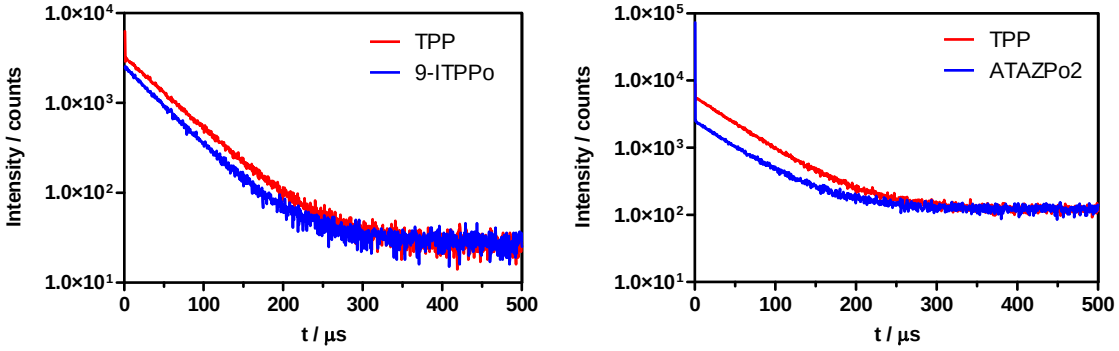

Figure S35: Phosphorescence decays at 1275 nm upon excitation at 355 nm of 9-ITPPo and ATAZPo2 in acetone. The decays of an optically matched solution of TPP are shown for comparison.

3.4 Optical properties of 9-benzamido porphycene and 2-phenylthiazolo[4,5-c] 2,7,12,17-tetraphenylporphycene.

Similarly to ATAZPos, both the absorption and emission spectra of TAZPo is red shifted with respect to its corresponding 9-AmPo precursor (Figure S36 and Table S1). The most relevant property of this new porphycene derivative is an unprecedented 2-fold enhancement of its photosensitising properties which makes it an even better candidate for photodynamic therapy.

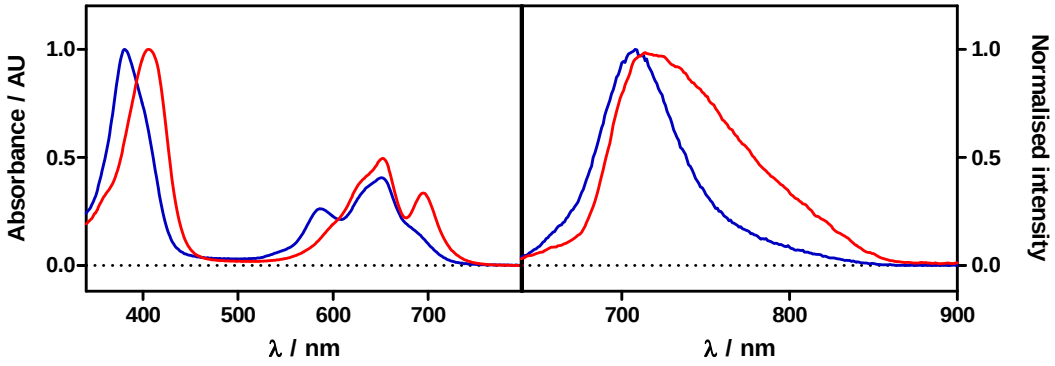

Figure S36: Absorption and fluorescence spectra of 9-AmPo (blue line) and its TAZPo derivative (red line).

Table S1. Optical properties of 9-AmPo and its TAZPo derivative in acetone.

Compound	λ_m[a]	λ_F[b]	Φ_F[c]	τ_S[d]	τ_T[e]	Φ_Δ[f]
9-AmPo	696	708	0.05	1	60	0.14
TAZPo	700	720	0.03	<0.2	20	0.31

[a] Wavelength of the lowest-energy absorption band (nm); [b] Wavelength of fluorescence (nm); [c] Fluorescence quantum yield; [d] Singlet state lifetime in air (ns); [e] Triplet state lifetime in argon (μs); [f] Singlet oxygen quantum yield.

4. References

1. P. G. Seybold and M. Gouterman, *J. Mol. Spectrosc.*, 1969, **31**, 1–13.

2. A. M. Brouwer, *Pure Appl. Chem.*, 2011, **83**, 2213–2228.

3. A. Jiménez-Banzo, X. Ragàs, P. Kapusta and S. Nonell, *Photochem. Photobiol. Sci.*, 2008, **7**, 1003–1010.

4. F. Wilkinson, W. P. Helman and A. B. Ross, *J. Phys. Chem. Ref. Data*, 1993, **22**, 113.

5. Gaussian 09, Revision D.03, M. J. Frisch, G. W. Trucks, H. B. Schlegel, G. E. Scuseria, M. A. Robb, J. R. Cheeseman, G. Scalmani, V. Barone, B. Mennucci, G. A. Petersson, H. Nakatsuji, M. Caricato, X. Li, H. P. Hratchian, A. F. Izmaylov, J. Bloino, G. Zheng, J. L. Sonnenberg, M. Hada, M. Ehara, K. Toyota, R. Fukuda, J. Hasegawa, M. Ishida, T. Nakajima, Y. Honda, O. Kitao, H. Nakai, T. Vreven, J. A. Montgomery, Jr., J. E. Peralta, F. Ogliaro, M. Bearpark, J. J. Heyd, E. Brothers, K. N. Kudin, V. N. Staroverov, R. Kobayashi, J. Normand, K. Raghavachari, A. Rendell, J. C. Burant, S. S. Iyengar, J. Tomasi, M. Cossi, N. Rega, J. M. Millam, M. Klene, J. E. Knox, J. B. Cross, V. Bakken, C. Adamo, J. Jaramillo, R. Gomperts, R. E. Stratmann, O. Yazyev, A. J. Austin, R. Cammi, C. Pomelli, J. W. Ochterski, R. L. Martin, K. Morokuma, V. G. Zakrzewski, G. A. Voth, P. Salvador, J. J. Dannenberg, S. Dapprich, A. D. Daniels, Ö. Farkas, J. B. Foresman, J. V. Ortiz, J. Cioslowski, and D. J. Fox, Gaussian, Inc., Wallingford CT, 2009.

6. O. Arad, N. Rubio, D. Sanchez-Garcia, J. I. Borrell and S. Nonell, *J. Porphyr. Phthalocyanines*, 2009, **13**, 376–381.

7. A. G. Barrientos, J. M. de la Fuente, T. C. Rojas, A. Fernández and S. Penadés, *Chemistry*, 2003, **9**, 1909–1921.

8. M. R. Hamblin, J. L. Miller and B. Ortel, *Photochem. Photobiol.*, 2000, **72**, 533–540.

2.2

Zampini, G.; **Planas, O.**; Marmottini, F.; Gulías, O.; Agut, M.; Nonell, S.; Latterini, L. Morphology effects on singlet oxygen production and bacterial photoinactivation efficiency by different silica-Protoporphyrin IX nanocomposites. *RSC Adv.*, 2017, 7, 14422-14429.
DOI: 10.1039/ c7ra00784a.

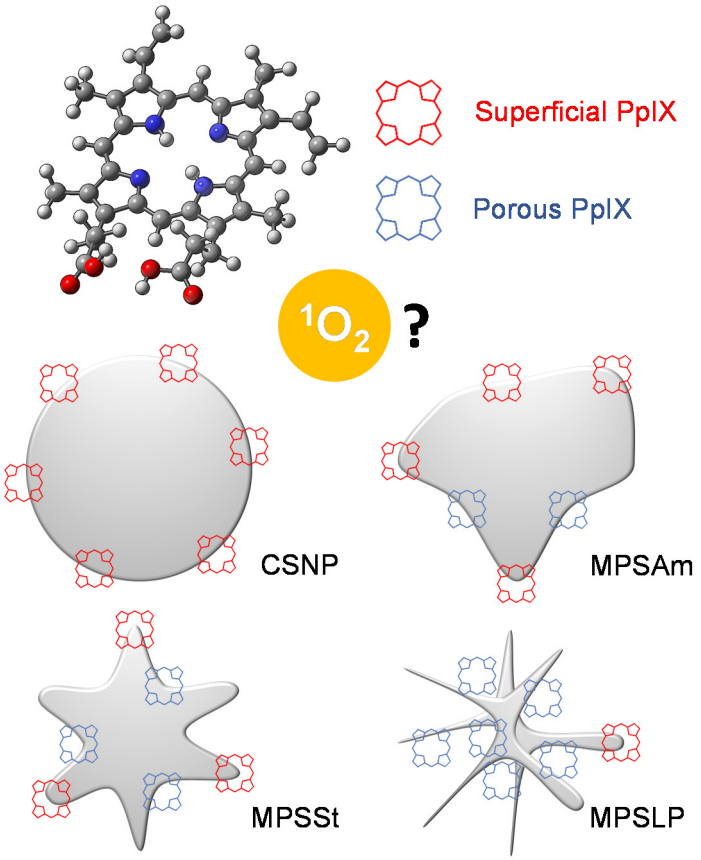

RSC Advances

PAPER

Cite this: *RSC Adv.*, 2017, **7**, 14422

Morphology effects on singlet oxygen production and bacterial photoinactivation efficiency by different silica-protoporphyrin IX nanocomposites†

G. Zampini,[ab] O. Planas,[b] F. Marmottini,[a] O. Gulías,[b] M. Agut,[b] S. Nonell*[b] and L. Latterini*[a]

Received 18th January 2017
Accepted 21st February 2017

DOI: 10.1039/c7ra00784a

rsc.li/rsc-advances

Different silica-protoporphyrin IX (PpIX) nanocomposites have been synthesized to evaluate the dependence of singlet oxygen production and bacterial inactivation efficiency on the morphology of the nanomaterials. Modulation of the synthetic procedure allowed obtaining silica nanoparticles with different porosity which were characterized by TEM and spectroscopic analysis after PpIX adsorption. Time-resolved phosphorescence measurements on the different nanoporous samples revealed that the porosity of the nanoparticles plays a pivotal role on the singlet oxygen production and release from the nanoparticles. Thus, apart from the expected decay of singlet oxygen outside the silica matrix, a second component has been observed for the porous materials, attributed to the decay of singlet oxygen inside the pores. The relative efficiency of singlet oxygen production resulted to be higher for the sample with the greatest pores volume. The capability of the nanocomposites to inactivate bacteria was tested *in vitro* on *Staphylococcus aureus* strain. Interestingly, the efficiency for singlet oxygen production of the nanocomposites and their bacterial inactivation efficiency followed a different trend, indicating that the relative position of the photosensitizer and the superficial properties of the particles affect the antibacterial activity of the overall system.

Introduction

Antimicrobial photodynamic therapy (aPDT) is based on the use of a photosensitizer (PS), able to generate reactive oxygen species (ROS) through irradiation at specific wavelengths.[1] It represents an effective treatment against antibiotic-resistant bacteria as ROS generated by PDT mechanism induce several damages on different levels of the cell,[2,3] thus bacteria will not be easily able to develop resistance.[4]

Particular interest has been focused on singlet oxygen ($^1O_2$), which is conveniently produced by energy transfer between the excited triplet state of a PS and molecular oxygen, normally present in the surrounding environment.[1]

The increase in $^1O_2$ production efficiency is a crucial goal to achieve for an effective application of photodynamic systems. Hydrophobic natural PSs, such as protoporphyrin IX (PpIX), are potentially very promising but the extreme low solubility in physiological medium precludes their direct application in aPDT;[5] indeed PpIX singlet excited states intersystem cross into triplet states with high quantum yields ($\Phi_T = 0.63 \pm 0.04$),[6] and the long-lived triplet states are quenched efficiently by molecular oxygen to generate $^1O_2$ with a reported quantum yield values (Φ_Δ) of 0.77 in CCl_4 and 0.60 in aqueous/TX100 solution.[7] However, the formation of ground-state dimers and aggregates is responsible for the lowering of $^1O_2$ quantum yield, experimentally demonstrated by the reduction in Φ_Δ value for increasing concentration of porphyrins in water, or with the increase in the ionic strength of the solution by the addition of NaCl.[8]

In the last decades, several micro and nano-heterogeneous systems, in particular silica-based nanomaterials, have been studied and developed[9] to overcome the solubility and the stability problems of the PS;[10] the increasing interest for this kind of nanomaterials arises from the huge benefits related to the great stability of a silica structure, conjugated with the versatility of the particle surface.[11] Indeed, very often they are used as a vehicle-system,[12–15] firstly because the solid and inorganic structure of the matrix acts as a protective barrier against species that can destroy or limit the activity of PSs,[16–19] and secondly the limitations due to the lability or the insolubility of these molecules may be overcome.[18,20]

The interactions between the photosensitizers and silica nanovectors have been recently investigated, with the aim to identify the most promising system for PDT. Different systems have been reported, wherein the non-covalent and covalent

[a]*Department of Chemistry, Biology and Biotechnology, University of Perugia, Via Elce di Sotto, 8, 06123 Perugia, Italy. E-mail: loredana.latterini@unipg.it*

[b]*Institut Químic de Sarrià, Universitat Ramon Llull, Via Augusta 390, Barcelona 08017, Spain. E-mail: santi.nonell@iqs.url.edu*

† Electronic supplementary information (ESI) available. See DOI: 10.1039/c7ra00784a

encapsulation of PpIX in both compact and mesoporous silica nanoparticles have been analyzed.[21,22]

Rossi and coworkers demonstrated that the covalent linkage of PpIX within the silica network allowed a significant improvement of the ability to produce singlet oxygen, obtaining a value of singlet oxygen quantum yield up to 0.9.[7]

The synthetic approaches derived from the pioneering work of Prasad and Kopelman groups[23,24] are based on the encapsulation of PpIX inside the core of silica nanoparticles, which were tested in PDT experiments both *in vitro* and *in vivo*.[25,26] Vivero-Escoto *et al.* anchored PpIX to silica nanoparticles through the use of stimuli-responsive groups, in order to achieve the self-regulated delivery of the PS triggered by the biological system itself.[27]

Most of the strategies relay on the modulation of the interaction between PpIX and silica and on synthetic steps to tune such interactions. Limited studies have been presented to relate the morphology of silica nanoparticles to PDT performances; a detailed investigation on how the matrix nanostructures affect PpIX photophysical behavior and singlet oxygen production is concealing. However, the possibility to use the silica mesostructures to tune the chemical and photophysical behavior of PpIX represents an important simplification on the preparation procedures and possible scale-up. To achieve an improvement in smart nanomaterial development, it would be extremely important to connect the photophysical behavior to the photodynamic action of PS-loaded nanomaterials in physiological conditions. The anchoring on a solid nanosupport[28,29] can inevitably modify not only the photophysics and the efficiency of a PS, but also the superficial properties of the materials, thus inducing eventual variations in the interactions with biological samples, such as bacteria.

Therefore, in this work, PpIX loaded on silica nanoparticles with different morphology have been analyzed through a systematic characterization of the ground, singlet and triplet excited states, evaluating how the morphology of the carrier affects the photophysical and photosensitizing pathways of the PS. Direct measurements of $^1O_2$ luminescence have been performed and the correlation to bacterial inactivation has been investigated to assess the influence of the physical–chemical properties of the nanocomposites to their antimicrobial behavior.

Experimental section

Materials

Protoporphyrin IX (PpIX, >97%) was obtained in diacid form from Frontier Scientific and used without further purification. Tetraethylorthosilicate (TEOS, 98%), (3-aminopropyl) triethoxysilane (APTES, ≥98%), hexadecyltrimethylammonium bromide (CTAB, 95%), hexadecyltrimethylammonium *p*-toluensulfonate (CTATos), triethanolamine ($TEAH_3$, >98%), mesitylene (98%), Pluronic F-127 ($EO_{106}PO_{60}EO_{106}$), hydrochloridric acid (HCl, 37%) and ammonium hydroxide solution (NH_4OH, 28.0–30.0% NH_3 basis), were all purchased from Sigma-Aldrich and used as received. Nanopure water (≤15.0 MΩ) from a Millipore Milli-Q gradient system, ethanol (96%) and methanol (anhydrous, 99.8%) from Sigma-Aldrich and *N*,*N*-dimethylformamide (DMF, ≥99%) from Acros Organics were used as solvents. *Staphylococcus aureus* CECT 239 were obtained from the Spanish Type Culture Collection (CECT).

Synthetic procedures

Compact silica nanoparticles (CSNP). 56 mL of ethanol, 4 mL of water and 1.6 mL of ammonium hydroxide solution were mixed in a flask equipped with a magnetic bar. After few minutes, 2.4 mL of TEOS was quickly added to the mixture under vigorous magnetic stirring. After 24 hours the suspension was centrifuged (3000*g*, 30 minutes) and the powder obtained was washed several times with ethanol and dried in air at room temperature.[30]

Mesoporous silica nanoparticles (MPSAm). 2.98 g of CTAB and 2.02 g of Pluronic F-127 were added to 30 mL of HCl solution (pH 0.5) under magnetic stirring; after 20 minutes 3.5 g of TEOS was added and the mixture was kept under magnetic stirring overnight. The gel formation occurred after the addition of 3.03 g of ammonium hydroxide solution (NH_4OH 30%), and the system was aged for 24 hours at room temperature and then dried in air at 60 °C for 24 hours. Finally, solid samples were heated at 600 °C for 3 hours to completely remove the surfactant.[31]

"Stellate" mesoporous silica nanoparticles (MPSSt). A mixture of 762.8 mg of hexadecyltrimethylammonium *p*-toluensulfonate, 97 μL of triethanolamine and 41 mL of water was stirred for 1 hour at 80 °C. Then 6.3 mL of TEOS was quickly added and the mixture was further stirred at 80 °C for 2 hours.

The as-synthesized MPSSt were filtered and washed several times with water and ethanol. The removal of the surfactant was obtained through solvent extraction in a boiling acidic methanol for 6 hours. The extracted particles were washed several times with ethanol and then dried in air.[32]

"Larger pore" mesoporous silica nanoparticles (MPSLP). A mixture of 620 mg of hexadecyltrimethylammonium *p*-toluenesulfonate, 100 μL of triethanolamine, 7.8 mL of mesitylene and 32.5 mL of water was stirred at 80 °C. After 1 hour, 7.8 mL of TEOS were quickly added and the mixture was stirred at 80 °C for 2 additional hours.

The MPSLP thus obtained were centrifuged at 3000*g* for 15 minutes and washed several time with ethanol, followed by acidic extraction in methanol for at least 6 hours. The extracted particles were washed several time with ethanol and then dried in air.

APTES functionalization. CSNP, MPSAm, MPSSt and MPSLP colloids were functionalized with APTES in order to graft amino terminal groups on the surface of the particle.

In a typical synthesis procedure, a weighted amount of silica nanoparticles was suspended in ethanol and sonicated for 5 minutes to yield a final concentration of 5 mg mL^{-1}. Then APTES (2 μL mL^{-1}) was added and the mixture was stirred overnight at room temperature. The APTES-to-silica ratio was kept constant for all samples.

The amino-functionalized silica nanoparticles were obtained after centrifugation at 3000*g* for 20 minutes, followed by several washes with ethanol. Finally, the solids were dried under air at room temperature.

PpIX loading onto CSNP, MPSAm, MPSSt, MPSLP. PpIX anchorage was achieved by an acid–base reaction between the carboxylic acids of PpIX and the free amino groups on the silica surface. A fresh solution of PpIX in its acid form was prepared in DMF immediately before use. Then, a weighted amount of amino-functionalized silica nanoparticles was added to obtain a final concentration of 2 mg mL^{-1} for CSNP and 5 mg mL^{-1} for MPSAm, MPSSt and MPSLP. To obtain PpIX-CSNP, PpIX-MPSAm, PpIX-MPSSt and PpIX-MPSLP, respectively. Each system was kept under magnetic stirring and stored in the dark for 24 hours.

Each silica suspension was then centrifuged at 3000*g* for 20 minutes; the collected solid was washed twice with DMF and once with ethanol, and finally dried under air.

The concentration of PpIX on the silica surface was evaluated from the difference between the PpIX solution absorbance before (starting solution) and after (supernatant) the anchoring procedure (eqn S1†).

Physicochemical characterization of the nanoparticles

Size and morphology of all silica samples was investigated by a Philips 208 transmission electron microscope (TEM) operating at 80 kV. A small drop of the suspensions of amino-functionalized nanoparticles in ethanol was deposited on a 300 square mesh copper grid pre-coated with a Formvar film and evaporated under air at room temperature. The particle size distribution was evaluated from several micrographs by means of the image analyser software ImageJ (Rasband, W.S., ImageJ, U. S. National Institutes of Health, Bethesda, Maryland, USA, http://imagej.nih.gov/ij/, 1997–2016). The zeta potential in aqueous suspensions was measured by a Nano-ZS Zetasizer (Malvern Instrument Ltd.). The samples were extensively sonicated prior to the measurements to ensure a complete dispersion of the nanoparticles.

Nitrogen adsorption–desorption isotherms at 77 K were determined using a computer controlled Micromeritics (Norcross, GA, USA) ASAP 2010 apparatus. Prior to adsorption measurements, samples were outgassed at room temperature overnight. The specific surface area was determined by the Brunauer, Emmett and Teller (B.E.T.) technique;[33] mesopore volume was analysed by the BJH method.[34]

Spectroscopic techniques

All spectroscopic measurements were carried out in spectroscopic grade DMF using a nanoparticle concentration of 2 mg mL^{-1} for all samples and after extensive sonication. Samples were sonicated before the measurements to ensure complete dispersion of the nanoparticles.

Absorption spectra were recorded on a Varian Cary 8454 UV/Vis Diode Array and on a Varian Cary 6000i dual-beam spectrophotometers. Fluorescence emission spectra were recorded on a Jobin Yvon-Spex Fluoromax-4 spectrofluorometer. Time-resolved fluorescence emission decays were measured by use of PicoQuant Fluotime 200 time-correlated single photon counting system equipped with a red sensitive photomultiplier. Excitation was achieved using a 375 nm picosecond diode laser working at 10 MHz. Fluorescence lifetimes were determined using FluoFit 4.6.5 analysis software from PicoQuant. The specific $^1O_2$ near-infrared phosphorescence decays at 1270 nm were recorded by means of a customized PicoQuant Fluotime 200 system described in detail elsewhere.[35] Briefly, a 532 nm diode-pumped Nd:YAG laser (FTSS355-Q, Crystal Laser) working at 1 KHz repetition rate was used for excitation. Laser emission was filtered by a 1064 rugate notch filter (Edmund Optics) and an uncoated SKG-5 filter (CVI Laser Corportation) placed at the exit port of the laser to remove any residual component of its fundamental emission in the near-infrared. Sample luminescence was filtered by a 1100 long-pass filter (Edmund optics) and a narrow bandpass filter at 1270 nm (bk-1270-70-B, bk Interfernzoptik) to isolate the $^1O_2$ emission. Photons emitted from the sample were detected using a TE-cooled near-IR sensitive photomultiplier tube assembly (H9170–45, Hamamatsu Photonics) and counted with a multichannel scaler (NanoHarp 250, PicoQuant GmbH). Time resolved-emission decays were fitted using non-linear regression function of Graph Pad Prism to recover the $^1O_2$ and triplet lifetimes (τ_Δ and τ_T, respectively). The quantum yield of $^1O_2$ production was derived from the amplitude of the signals.

Transient absorption experiments were carried out using a home-built nanosecond laser flash photolysis system. The second harmonic (532 nm) of a Continuum Surelite I-10 Nd:YAG laser (5 ns pulse width, 7.5 mJ per pulse) was directed to the sample and a 75 W short arc Xe lamp (USHIO) was used for probing the transient absorption in a right-angle geometry. Changes in the sample absorbance at different observation wavelengths were discriminated using a PTI 101 monochromator and detected using a Hamamatsu R928 photomultiplier. The signal was fed to a Lecroy WaveSurfer 454 oscilloscope for digitizing and averaging (typically 10 shot) and finally transferred to a PC computer for data storage and analysis. The energy of the laser pulsed was measured with a RJ 7610 energy meter from Laser Precision Corp. The system was controlled by a house-developed LKS software (LabView, National Instruments).

Bacterial inactivation tests

Microbial strains and growth conditions. Bacteria pre-inoculation was performed by adding the culture cells in sterile tryptic soy broth (TSB) and letting them grow overnight at 37 °C. Then stock inoculum suspension was prepared by diluting 100 μL of bacteria preinoculus in 10 mL of TSB. The suspension was kept in incubation at 37 °C until the OD reached a value of 0.4 at 620 nm (equivalent to *ca.* 10^8 colony-forming units), then centrifuged at 3000*g* for 10 minutes, and the pellet obtained was washed once with sterilized PBS.

Photodynamic inactivation procedure. A weighted amount of dye-doped silica nanoparticles (PpIX-CSNP, PpIX-MPSAm, PpIX-MPSSt or PpIX-MPSLP) was added to the cell suspension in PBS in order to obtain a final concentration of 2 mg mL^{-1}. The as-prepared system was incubated at 37 °C for 15 minutes, then 0.3 mL were placed in 96-well plates, and illuminated from the top by several blue-emitting lamps (420 nm, irradiance 10

mW cm^{-2}, LZC-420, Luzchem) for different irradiation times. Serially 10 times-dilution were performed, and each well was seeded on tryptic soy agar in 4 replicas, and incubated at 37 °C overnight. Colony-forming units (CFU) were counted to calculate the survival fractions. A similar protocol was applied for the dark control, with the exception of the irradiation procedure.

Results and discussion

Silica nanoparticles morphology and superficial properties

Fig. 1 shows the TEM images of the amino-functionalized nanostructures. Rapid inspection of the different contrast TEM images reveals that the prepared nanoparticles present four different types of morphologies: compact regular silica nanoparticles (CSNP, A), amorphous mesoporous silica nanoparticles (MPSAm, B), stellate mesoporous silica nanoparticles (MPSSt, C) and large-pore mesoporous silica nanoparticles (MPSLP, D). The mean diameter obtained for CSNP, MPSSt and MPSLP (see ESI, Fig. S1–S3†), was respectively 117 nm (σ = 7.1 nm), 83 nm (σ = 8.8 nm) and 94 nm (σ = 8.8 nm). It was not possible to accurately evaluate the size distribution for MPSAm due to the irregular nature of its structure, however nanostructures having tens of nm dimensions can be observed.

The control of nanoparticle's dimensions was achieved by the tight regulation of reactant's concentrations and synthetic conditions; the differential morphology of the silica nanoparticles is the result of templated synthetic strategies used for the sample preparation. In particular, CSNP were synthesized following the Stöber procedure with minor changes in the relative quantity of water, ethanol and ammonia, to achieve a good monodisperse size distribution for CSNP sample.[30] The different pore shapes and morphologies for samples B, C and D (Fig. 1), were achieved by using different templating agents. Pluronic F127 yielded highly curved cage-like pores[36] with small diameter,[31] as in the case of MPSAm. Instead, the cationic surfactant cetyltrimethylammonium (CTA^+) associated to tosilate (Tos^-), a counterion with strong affinity to the polar head of the surfactant,[32] led to the formation of a star-shaped ("stellate") structure for MPSSt. Finally, the addition of mesitylene, a swelling agent, to the reaction mixture caused an increase in the dimensions of the pores[37] without modifying their star shape (MPSLP). The achieved morphologies were not altered by amino-functionalization.

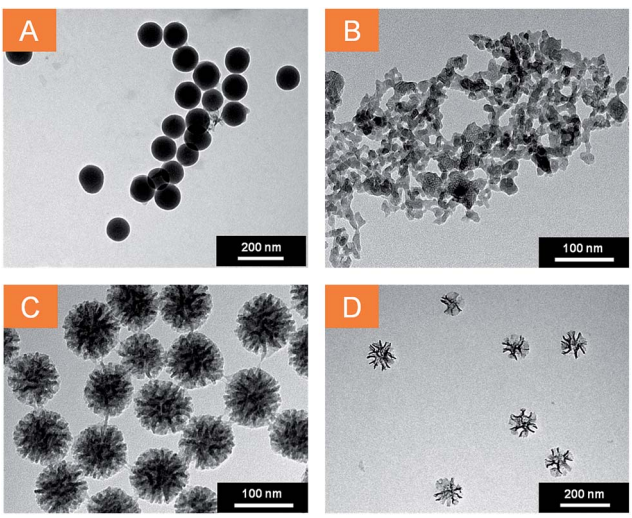

Fig. 1 TEM images of silica nanoparticles. (A) CSNP scale bar: 200 nm, (B) MPSAm scale bar: 100 nm, (C) MPSSt scale bar: 100 nm, (D) MPSLP scale bar: 200 nm.

The surface area data of the nanosystems as well as zeta potential values in aqueous suspensions are summarized in Table S1.†

The adsorption and desorption isotherms of all the silica samples presented similar profiles, reflecting a mesoporous structure for all the samples; BET analysis of the data evidences that the surface area increases in the order CSNP, MPSAm, MPSSt and MPSLP, in agreement with the TEM findings. The evaluation of mesopore volume and mesopore size distribution was performed by BJH analysis of the adsorption and desorption data. The mesopore volume calculated from adsorption data for pores of dimensions between 20 Å and 400 Å is reported in Table S1 and in Fig. S5† the mesopore size distribution curves are showed. It is of interest to note that in the case of CSNP sample the calculated mesopore volume is 0.13 $cm^3\ g^{-1}$ while the values obtained for others samples are included in the range 0.44–0.52 $cm^3\ g^{-1}$. The pore size distribution curves put in evidence that, differently from the other samples, a wide maximum occur around a pore diameter of 100 Å in the case of MPSSt sample.

At the same time, a clear trend of the final zeta-potential values going from CSNP to MPSLP can be observed, which correlates with the surface area and pore-structuring of the nanomaterials. As porosity is increased, the zeta-potential diminishes. It is known that bare silica nanoparticles are generally negatively charged in water because of the presence of partly ionized silanol groups, whereas surface functionalization with terminal amino groups increases the value of the zeta potential.[38,39] The results suggest that the pore size plays a fundamental role on the zeta potential values. This observation can be rationalized considering that APTES grafting has been carried out keeping constant the ratio of silica and APTES concentrations for all samples. The larger are the pores, the higher is the exposed surface (inner and outer the pores). Moreover, the samples bearing larger pores have a higher surface concentration of silanol moieties, resulting in lower zeta potentials. As a result, the surface of the nanoparticles with larger structures is on average, less covered by positively charged amino groups in the nanoparticles with larger pores, yielding to a more negative zeta potential value. Accordingly, for CSNP, in which no pores are present, the most positive zeta potential value is obtained.

Silica–PpIX conjugates

PpIX was electrostatically attached onto the different amino-functionalized silica nanostructures suspended in DMF by acid–base reaction of its carboxylic acid groups with the nanoparticle amino groups, and the samples PpIX-CSNP, PpIX-MPSAm, PpIX-MPSSt and PpIX-MPSLP were obtained. The concentration of PpIX ($nmol_{PpIX}/mg_{silica}$) on the different silica samples was quantified through spectrophotometric measurements and is given in

Table S1.† The concentration is the highest for CSNPs, and roughly equal for all mesoporous nanomaterials, independent of the pore size. Conjugation of PpIX did not modify the zeta potentials to a great extent (Table S1†).

Photophysical properties of silica–PpIX conjugates

To evaluate the effect of the silica matrix on the photophysical behavior of PpIX, each sample was re-suspended in DMF and their absorption and fluorescence spectra were recorded. The scattering corrected absorption spectra of PpIX-loaded nanoconstructs are shown in Fig. 2a. For all samples, the classical shape of PpIX absorption is observed, with an intense Soret band centered at 406 nm and several Q bands in the visible range. However, an additional band at 675 nm, attributed to aggregated species[40–42] can be detected for all samples, albeit with different intensities.

Fluorescence spectra (Fig. 2b) likewise show the typical shape of PpIX but a new band at 680 nm is observed, whose relative intensity varies from sample to sample. Porphyrins have a strong tendency to aggregate and dimers are known to show red-shifted fluorescence relative to monomers, while higher-order aggregates are non-fluorescent.[41] The observed spectra are consistent with the presence of both fluorescent dimers and non-fluorescent higher-order aggregates. Thus, PpIX-MPSLP displays the highest fluorescence intensity while PpIX-CNSP shows the lowest, despite their respective PpIX loading show the opposite trend (Table S1†). This indicates that PpIX is most aggregated in CNSP, consistent with its lowest specific surface.

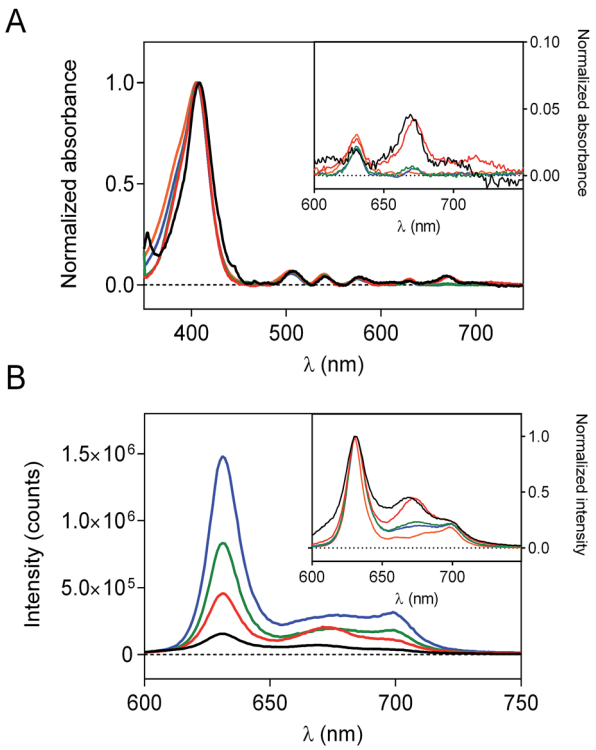

Fig. 2 (A) Normalized absorption spectra of different silica nanoconjugate suspensions (black line PpIX-CSNP, red line PpIX-MPSAm, green line PpIX-MPSSt and blue line PpIX-MPSLP) in concentration of 2 mg mL^{-1} in DMF. Inset: magnification between 650–700 nm. (B) Overlaid fluorescence emission spectra (λ_{exc} = 532 nm); normalized fluorescence emission spectra, including PpIX emission in DMF, is shown as an inset for comparison purposes.

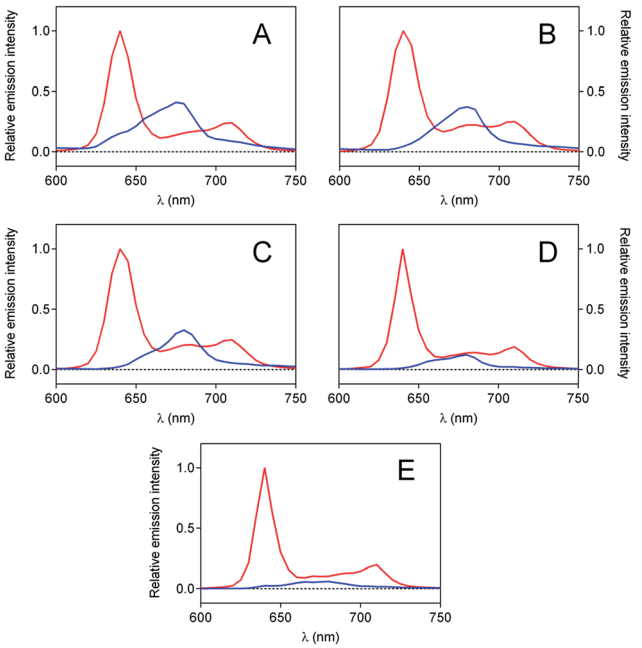

Fig. 3 Time-resolved fluorescence spectra of (A) PpIX-CSNP, (B) PpIX-MPSAm, (C) PpIX-MPSSt, (D) PpIX-MPSLP,and (E) PpIX following the excitation at 532 nm. 14 ns component is indicated with a red line and 5 ns in blue.

The aggregation phenomenon was further confirmed by time-resolved fluorescence spectroscopy (Fig. 3). For each suspension, two contributions to the fluorescence decay were detected: a long-lived component of 14 ns, with the spectral features of monomeric PpIX in DMF,[43] and a shorter-lived component of about 5 ns, attributed to the fluorescent dimers.[44]

Further analysis was conducted to characterize the photophysical behavior of PpIX triplet state, both conjugated and unconjugated to silica, in air and in argon-saturated solution (Fig. S6 and Table S2†). All transient absorption signals could be satisfactorily fitted with a monoexponential decay function. In air-saturated samples, a triplet lifetime of about 0.4 μs was found for all the samples. However, when oxygen was removed from the suspensions through extensive argon bubbling, large differences were observed between all samples with a clear trend: the larger the pore, the longer the triplet lifetime becomes, suggesting that porous silica nanoparticles protect PpIX from self-quenching.[45]

Singlet oxygen measurements

Kinetic studies. Time-resolved phosphorescence signals at 1270 nm for both free PpIX and PpIX-CSNP conjugates in DMF (Fig. 4) could be fitted using the classic rise and decay biexponential model (eqn (1)),[35] where τ_Δ is the singlet oxygen lifetime and τ_T the triplet lifetime.

$$S_t = S_0 \times \frac{\tau_\Delta}{\tau_\Delta - \tau_T} \times \left(e^{-t/\tau_\Delta} - e^{-t/\tau_T}\right) \quad (1)$$

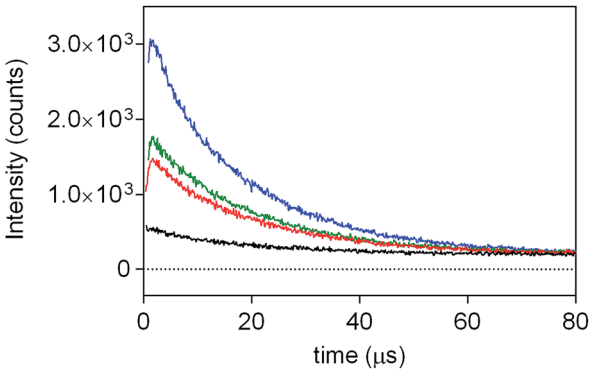

Fig. 4 Time-resolved $^1O_2$ phosphorescence spectra of PpIX-CSNP (black line), PpIX-MPSAm (red line), PpIX-MPSSt (green line) and PpIX-MPSLP (blue line) acquired at 1270 nm with an excitation wavelength of 532 nm.

In contrast, singlet oxygen luminescence signals from mesoporous nanomaterials required the introduction of an additional decay component to adequately reproduce the experimental traces (eqn (2)).

$$S_t = S_{0,1} \times \frac{\tau_{\Delta 1}}{\tau_{\Delta 1} - \tau_{T1}} \times e^{-t/\tau_{\Delta 1}} + S_{0,2} \times \frac{\tau_{\Delta 2}}{\tau_{\Delta 2} - \tau_{T2}} \times e^{-t/\tau_{\Delta 2}} - \left(S_{0,1} \times \frac{\tau_{\Delta 1}}{\tau_{\Delta 1} - \tau_T} + S_{0,2} \times \frac{\tau_{\Delta 2}}{\tau_{\Delta 2} - \tau_T} \right) \times e^{-t/\tau_T} \quad (2)$$

Results from fittings are summarized in Table 1. PpIX and PpIX-CSNP showed a growth lifetime of 0.4 and 0.5 μs and a decay lifetime of 22 and 20 μs, respectively. These lifetimes match those observed for molecular PS in DMF.[46] In mesoporous nanomaterials, a similar rise lifetime was observed (0.3–0.5 μs) along with two decay components of 3 μs and 19–20 μs. In order to assign the observed lifetimes, phosphorescence decays were also recorded under oxygen-saturated conditions. A clear shortening of the rise component was observed while the decay components remained almost unaffected (Fig. S7 and Table S3†). Taken together with the results of the transient absorption experiments, these data indicate that the rise component corresponds to the formation of $^1O_2$ from the triplet state of PpIX and the decay components to the decay of $^1O_2$.

In order to explain these results, it is worth recalling that while in compact nanoparticles only the external surface is available for anchoring the PS, the porosity of the mesoporous nanoparticles may enable the localization of PpIX both on the external surface and inside the silica pores. It can therefore be proposed that two populations of $^1O_2$ might exist; one formed at the silica–solvent interface and able to escape and relax in the outer bulk solvent and another that decays inside the silica pores. The external $^1O_2$ population decays therefore with a lifetime of 20 μs, as in the case of PpIX-CSNP. The inner-$^1O_2$ population, trapped in the silica structures, shows a much faster decay, probably due to a combination of three different effects: (i) an increase in the collision frequency of $^1O_2$ with the walls of the pores,[47] (ii) quenching of $^1O_2$ by free amino groups deriving from APTES functionalization,[48,49] or (iii) quenching by OH groups of the surface silanols and of strongly hydrogen-bonded water molecules remaining from the nanoparticle preparation procedure.[50]

Table 1 Fitting parameters obtained from the analysis of time-resolved phosphorescence signals at 1270 nm for different silica–PpIX suspensions in air-saturated conditions at 2 mg mL^{-1} of silica

Conjugate	$S_{0,1}$/cnts	$S_{0,2}$/cnts	τ_T/μs	$\tau_{\Delta 1}$/μs	$\tau_{\Delta 2}$/μs
PpIX	N/A	—	0.4	22	—
PpIX-CSNP	341	—	0.5	19.9	—
PpIX-MPSAm	1291 (95%)	71 (5%)	0.4	19.5	3.0
PpIX-MPSSt	1515 (92%)	125 (8%)	0.3	19.5	3.0
PpIX-MPSLP	2584 (76%)	792 (24%)	0.5	19.2	3.1

This interpretation was confirmed by a second series of experiments in which PpIX-MPSLP was re-suspended in D_2O. It is well known that OD groups, produced by isotopic exchange of the trapped water molecules and surface silanols with D_2O, are far worse quenchers of $^1O_2$ than OH groups.[51] One would therefore expect that the $^1O_2$ lifetime inside the pores would now be closer to that in the external bulk solvent. Consistent with this expectation, the phosphorescence decay could be satisfactorily fitted by a biexponential model with a 3 μs rise time and 53 μs for the single decay component (Fig. S8†). One can notice that the determined $^1O_2$ decay time value (53 μs) is slightly shorter than the reported lifetime of $^1O_2$ in D_2O, (67 μs),[52] indicating that silica still exerts some quenching effect.

Singlet oxygen production efficiency. From the fitted initial amplitude of the $^1O_2$ signal (S_0), it is possible to estimate the relative singlet oxygen production quantum yield (Φ_Δ), which indicates the ability of a system to sensitize $^1O_2$ with respect to a reference. Given that PpIX-CSNP was the sample with the lowest $^1O_2$ production, it has been taken as a reference. For the mesoporous samples, Φ_Δ was evaluated according to eqn (3) where $k_{R,DMF}$ and k_{R,H_2O} are the radiative rate constants for $^1O_2$ in DMF and H_2O (0.63 s^{-1} and 0.209 s^{-1}, respectively).[51] This correction is necessary to account for the fact that the probability of radiative decay is higher in DMF than in H_2O.

$$\text{Relative } \Phi_\Delta = \frac{\Phi_\Delta^{\text{mesoporous}}}{\Phi_\Delta^{\text{CSNP}}} = \frac{S_{0,1}^{\text{mesoporous}} + \frac{k_{R,DMF}}{k_{R,H_2O}} S_{0,2}^{\text{mesoporous}}}{S_0^{\text{CSNP}}} \quad (3)$$

As shown in Table 2, the mesoporous materials have a higher efficiency in the photosensitization of $^1O_2$. In particular, PpIX-MPSAm, PpIX-MPSSt and PpIX-MPSLP display a relative efficiency about 4.4, 5.5 and 14.6 times higher than PpIX-CSNP, respectively, with PpIX-MPSLP presenting the highest value. However, in the mesoporous materials, the two populations of $^1O_2$ molecules, kinetically detected (Table 1), might show different effectiveness to photoinactivate bacteria. The relative contribution of the two populations can be estimated from the amplitude of the components corrected for the radiative rate constants as detailed in eqn (4) and is also given in Table 2.

Table 2 Singlet oxygen production efficiency of silica nanomaterials related to PpIX-CSNP. All samples were measured using the same silica concentration (2 mg mL^{-1})

Sample	Loading nmol$_{PpIX}$/mg$_{silica}$	Relative $^1O_2$ efficiency (% outer population)
PpIX-CSNP	1.01	1 (100%)
PpIX-MPSAm	0.74	4.4 (86%)
PpIX-MPSSt	0.60	5.5 (81%)
PpIX-MPSLP	0.64	14.6 (52%)

$$\text{Outer } {}^1O_2\ (\%) = \frac{S_{0,1}^{\text{mesoporous}}}{S_{0,1}^{\text{mesoporous}} + \frac{k_{R,DMF}}{k_{R,H_2O}} S_{0,2}^{\text{mesoporous}}} \times 100 \quad (4)$$

Bacterial inactivation

The photoinduced antibacterial property of PpIX-doped silica nanoparticles was tested to correlate this activity with the morphology and $^1O_2$ production capacity. *Staphylococcus aureus* was chosen as a model Gram positive bacteria, and the concentration of all silica samples was kept constant (see Table S4 in the ESI†) to properly compare the efficiency in bacterial killing.

As expected, neither bare silica nanoparticles nor any of the PpIX–silica conjugates showed any remarkable dark toxicity towards *S. aureus* (Fig. 5). Moreover, bare silica nanoparticles, with no PpIX adsorbed, were non-toxic even at the highest light doses tested (12 J cm^{-2}).

The efficacy of bacterial photoinactivation varied dramatically for the different PpIX-loaded samples, highlighting the importance of the nanoparticle structure. PpIX-MPSAm, which has an undefined geometry and irregular structure, does not develop any photo-induced antibacterial activities; indeed for this sample a decrease in bacterial population comparable to the one measured in the dark, has been observed. Thus, this material was not considered worth of further scrutiny.

Among the samples with well-defined nanostructures, the highest reduction in the survival of *S. aureus* was achieved upon irradiation of PpIX-CSNP; the result can be quite surprising since this nanomaterial shows the lowest $^1O_2$ production efficacy (Table 2). A possible explanation for such apparent contradiction is that its positive zeta potential enables the closest proximity to the bacteria, thereby facilitating the delivery of $^1O_2$ and/or PpIX to the bacteria.[53–55]

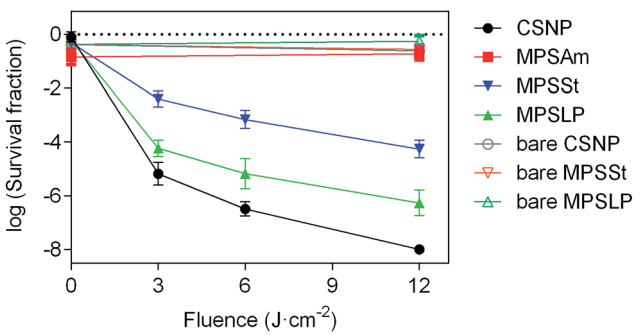

Fig. 5 Survival curves of *S. aureus* incubated with different silica nanoconjugates; the closed symbols are used to indicate the systems with PpIX (in solution or anchored onto silica surface), whereas the open symbols are the control experiments (bare silica nanoparticles with no photosensitizer adsorbed). The irradiation was performed at 420 nm.

Among the mesoporous nanomaterials, those with large pores (PpIX-MPSLP) showed higher antibacterial efficacy than those with small pores (PpIX-MPSSt), which correlates with the respective $^1O_2$ quantum yields and the extent of PpIX aggregation. One could probably expect that if their zeta potentials had been as positive as those of CSNP, their antibacterial efficacy would be higher.

Therefore, the effort to direct the synthesis toward the construction of nanomaterials with definite geometry is crucial to maximize the exploitation of their properties. These results underline that the increase in Φ_Δ is not necessarily the ultimately goal for achieving maximum efficiency in bacterial photoinactivation, factors such as zeta potential and morphology appear at least as crucial. Therefore, for a complete evaluation of new systems, photophysical studies should be correlated with the nanoparticle structure using physicochemical and biological assays to ascertain the effective improvement of the overall efficiency.

Conclusions

In this work, deeper insight on the photophysical behavior, singlet oxygen production efficiency and antimicrobial activity of PpIX-doped silica nanoparticles has been achieved through correlation of the different silica morphology with the optical and photophysical properties of PpIX–silica conjugate.

From our results, it can be derived that the silica nanoparticles' morphology and PpIX localization in the inorganic matrix cause major changes in the photophysical behavior of PpIX, in the photosensitization of $^1O_2$ and in the bacterial photoinactivation efficiency.

Acknowledgements

Financial support for this research was obtained from the Spanish Ministerio de Economía y Competitividad (Grant No. CTQ2013-48767-C3-1-R) and the University of Perugia. G.Z. thanks the support of the University of Perugia for the Erasmus fellowship. O.P. thanks the European Social Funds and the SUR del DEC de la Generalitat de Catalunya for his predoctoral fellowship (grant No. 2016 FI_B2_00100).

Notes and references

1 D. R. Kearns, *Chem. Rev.*, 1971, **71**, 395–427.
2 H. Pelicano, D. Carney and P. Huang, *Drug Resist. Updates*, 2004, **7**, 97–110.
3 R. Dosselli, R. Ruiz-González, F. Moret, V. Agnolon, C. Compagnin, M. Mognato, V. Sella, M. Agut, S. Nonell, M. Gobbo and E. Reddi, *J. Med. Chem.*, 2014, **57**, 1403–1415.

4 F. Giuliani, M. Martinelli, A. Cocchi, D. Arbia, L. Fantetti and G. Roncucci, *Antimicrob. Agents Chemother.*, 2010, **54**, 637–642.
5 H. Ding, B. D. Sumer, C. W. Kessinger, Y. Dong, G. Huang, D. A. Boothman and J. Gao, *J. Controlled Release*, 2011, **151**, 271–277.
6 C. B. Nielsen, J. S. Forster, P. R. Ogilby and S. B. Nielsen, *J. Phys. Chem. A*, 2005, **109**, 3875–3879.
7 L. M. Rossi, P. R. Silva, L. L. R. Vono, a U. Fernandes, D. B. Tada and M. S. Baptista, *Langmuir*, 2008, **24**, 12534–12538.
8 D. G. Fresnadillo and S. Lacombe, in *Singlet Oxygen: Applications in Biosciences and Nanosciences*, 2016, vol. 1, pp. 105–143.
9 J. L. Vivero-Escoto, in *Photodynamic Therapy: Fundamentals, Applications and Health Outcomes*, 2015, pp. 1–35.
10 Y. Hsia, M. Sivasubramanian, N.-T. Chen and L.-W. Lo, in *Nanomaterials for Tumor Targeting Theranostics: A Proactive Clinical Perspective*, 2016, pp. 143–176.
11 V. Ambrogi, A. Donnadio, D. Pietrella, L. Latterini, F. A. Proietti, F. Marmottini, G. Padeletti, S. Kaciulis, S. Giovagnoli and M. Ricci, *J. Mater. Chem. B*, 2014, **2**, 6054.
12 V. Ambrogi, L. Perioli, C. Pagano, L. Latterini, F. Marmottini, M. Ricci and C. Rossi, *Microporous Mesoporous Mater.*, 2012, **147**, 343–349.
13 L. Latterini and L. Tarpani, *J. Phys. Chem. C*, 2011, **115**, 21098–21104.
14 Z. Chu, S. Zhang, C. Yin, G. Lin and Q. Li, *Biomater. Sci.*, 2014, **2**, 827–832.
15 J. Vivero-Escoto and M. Elnagheeb, *Nanomaterials*, 2015, **5**, 2302–2316.
16 M. Manzano, V. Aina, C. O. Areán, F. Balas, V. Cauda, M. Colilla, M. R. Delgado and M. Vallet-Regí, *Chem. Eng. J.*, 2008, **137**, 30–37.
17 I. I. Slowing, B. G. Trewyn, S. Giri and V. S. Y. Lin, *Adv. Funct. Mater.*, 2007, **17**, 1225–1236.
18 I. I. Slowing, J. L. Vivero-Escoto, C.-W. Wu and V. S.-Y. Lin, *Adv. Drug Delivery Rev.*, 2008, **60**, 1278–1288.
19 C. Barbé, J. Bartlett, L. Kong, K. Finnie, H. Q. Lin, M. Larkin, S. Calleja, A. Bush and G. Calleja, *Adv. Mater.*, 2004, **16**, 1959–1966.
20 R. Singh and J. W. Lillard, *Exp. Mol. Pathol.*, 2009, **86**, 215–223.
21 F. Figueira, J. A. S. Cavaleiro and J. P. C. Tomé, *J. Porphyrins Phthalocyanines*, 2011, **15**, 517–533.
22 P. Couleaud, V. Morosini, C. Frochot, S. Richeter, L. Raehma and J.-O. Durand, *Nanoscale*, 2010, **2**, 1083–1095.
23 I. Roy, T. Y. Ohulchanskyy, H. E. Pudavar, E. J. Bergey, A. R. Oseroff, J. Morgan, T. J. Dougherty and P. N. Prasad, *J. Am. Chem. Soc.*, 2003, **125**, 7860–7865.
24 F. Yan and R. Kopelman, *Photochem. Photobiol.*, 2003, **78**, 587–591.
25 V. Simon, C. Devaux, A. Darmon, T. Donnet, E. Thiénot, M. Germain, J. Honnorat, A. Duval, A. Pottier, E. Borghi, L. Levy and J. Marill, *Photochem. Photobiol.*, 2010, **86**, 213–222.
26 J. Qian, A. Gharibi and S. He, *J. Biomed. Opt.*, 2015, **14**, 14012.
27 J. L. Vivero-Escoto and D. L. Vega, *RSC Adv.*, 2014, **4**, 14400.
28 L. Latterini and M. Amelia, *Langmuir*, 2009, **25**, 4767–4773.
29 G. Alberto, I. Miletto, G. Viscardi, G. Caputo, L. Latterini, S. Coluccia and G. Martra, *J. Phys. Chem. C*, 2009, **113**, 21048–21053.
30 R. Lindberg, J. Sjoblom and G. Sundholm, *Colloids Surf., A*, 1995, **99**, 79–88.
31 K. Suzuki, K. Ikari and H. Imai, *J. Am. Chem. Soc.*, 2004, **126**, 462–463.
32 K. Zhang, L.-L. Xu, J.-G. Jiang, N. Calin, K.-F. Lam, S.-J. Zhang, H.-H. Wu, G.-D. Wu, B. Albela, L. Bonneviot and P. Wu, *J. Am. Chem. Soc.*, 2013, **135**, 2427–2430.
33 S. Brunauer, P. H. Emmett and E. Teller, *J. Am. Chem. Soc.*, 1938, **60**, 309–319.
34 E. P. Barrett, L. G. Joyner and P. P. Halenda, *J. Am. Chem. Soc.*, 1951, **73**, 373–380.
35 A. Jiménez-Banzo, X. Ragàs, P. Kapusta and S. Nonell, *Photochem. Photobiol. Sci.*, 2008, **7**, 1003–1010.
36 K. J. Klabunde and R. M. Richards, *Nanoscale Materials in Chemistry*, John Wiley & Sons, 2nd edn, 2009.
37 C. Robertson, R. Beanland, S. a. Boden, A. L. Hector, R. J. Kashtiban, J. Sloan, D. C. Smith and A. Walcarius, *Phys. Chem. Chem. Phys.*, 2015, **17**, 4763–4770.
38 T. Schiestel, H. Brunner and G. E. M. Tovar, *J. Nanosci. Nanotechnol.*, 2004, **4**, 504–511.
39 R. Selvaggi, L. Tarpani, A. Santuari, S. Giovagnoli and L. Latterini, *Appl. Catal., B*, 2015, **168**, 363–369.
40 C. Aggelidou, T. A. Theodossiou and K. Yannakopoulou, *Photochem. Photobiol.*, 2013, **89**, 1011–1019.
41 L. Monsù Scolaro, M. Castriciano, A. Romeo, S. Patanè, E. Cefalì and M. Allegrini, *J. Phys. Chem. B*, 2002, **106**, 2453–2459.
42 A. A. Sivash, Z. Masinovský and G. I. Lozovaya, *BioSystems*, 1991, **25**, 131–140.
43 M. A. Jhonsi, A. Kathiravan and R. Renganathan, *Spectrochim. Acta, Part A*, 2008, **71**, 1507–1511.
44 F. Ricchelli, *J. Photochem. Photobiol., B*, 1995, **29**, 109–118.
45 M. A. Filatov, S. Baluschev and K. Landfester, *Chem. Soc. Rev.*, 2016, **45**, 4668–4689.
46 S. Oelckers, T. Hanke and B. Roder, *J. Photochem. Photobiol., A*, 2000, **132**, 29–32.
47 K. K. Iu and J. K. Thomas, *J. Photochem. Photobiol., A*, 1993, **71**, 55–60.
48 R. H. Young, R. L. Martin, D. Feriozi, D. Brewer and R. Kayser, *Photochem. Photobiol.*, 1973, **17**, 233–244.
49 B. M. Monroe, *J. Phys. Chem.*, 1977, **81**, 1861–1864.
50 B. Cojocaru, M. Laferrière, E. Carbonell, V. Parvulescu, H. García and J. C. Scaiano, *Langmuir*, 2008, **24**, 4478–4481.
51 M. Hild and R. Schmidt, *J. Phys. Chem. A*, 1999, **103**, 6091–6096.
52 E. Boix-Garriga, B. Rodríguez-Amigo, O. Planas and S. Nonell, in *Singlet Oxygen: Applications in Biosciences and Nanosciences*, Royal Society of Chemistry, 2016, vol. 1, pp. 23–46.
53 B. Gottenbos, D. W. Grijpma, H. C. van der Mei, J. Feijen and H. J. Busscher, *J. Antimicrob. Chemother.*, 2001, **48**, 7–13.
54 T. J. Silhavy, D. Kahne and S. Walker, *Cold Spring Harbor Perspect. Biol.*, 2010, **2**, 1–16.
55 A. M. El Badawy, R. G. Silva, B. Morris, K. G. Scheckel, M. T. Suidan and T. M. Tolaymat, *Environ. Sci. Technol.*, 2011, **45**, 283–287.

Electronic Supplementary Material (ESI) for RSC Advances.

Morphology effects on singlet oxygen production and bacterial photoinactivation efficiency by different silica-Protoporphyrin IX nanocomposites

G. Zampini,[a,b] O. Planas,[b] F. Marmottini,[a] O. Gulías,[b] M. Agut,[b] S. Nonell [b,*] and L. L. Latterini[a,*]

[a.] *Department of Chemistry, Biology and Biotechnology, via Elce di Sotto 8, 06123 Perugia, Italy.*

[b.] *Institut Químic de Sarrià, Universitat Ramon Llull, Via Augusta 390, Barcelona 08017, Spain.*

Supporting equation

$$mol_{(PpIX)}/mg_{(Si)} = \frac{(\frac{Abs_0 - Abs_t}{\varepsilon_{405}}) \times V}{mg_{Si}}$$

(Eq. S1)

Abs$_0$: *absorption values at 405 nm of PpIX starting solution.*

Abs$_t$: *absorption values at 405 nm of the supernatant collected after the anchoring procedure.*

ε_{405}: *PpIX extinction coefficient in DMF at 405 nm.*

V: *volume.*

mg$_{Si}$: *silica weight in milligram added to PpIX solution.*

Supporting figures

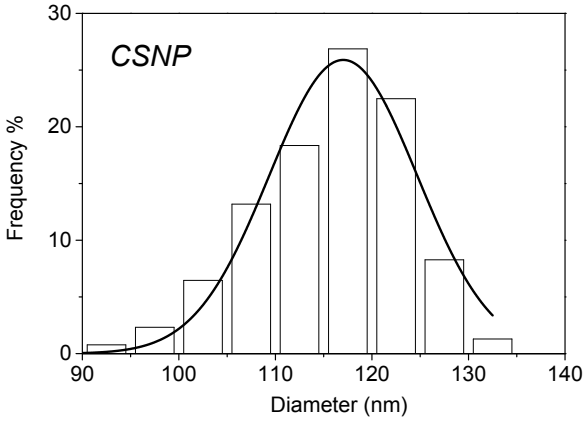

Figure S1. TEM size distribution for CSNP, counting approximately 300 nanoparticles; average diameter 117 nm (σ = 7.1).

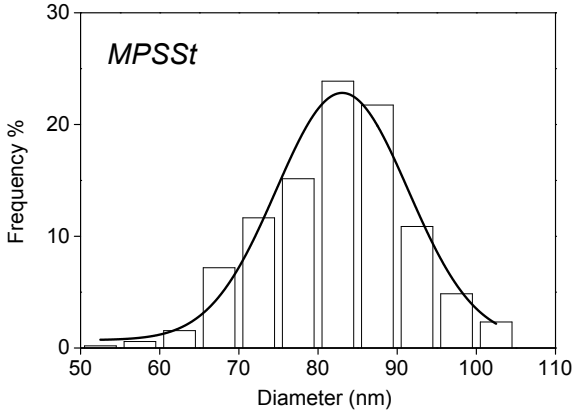

Figure S2. TEM size distribution for MPSSt, counting approximately 300 nanoparticles; average diameter 83 nm (σ = 8.8).

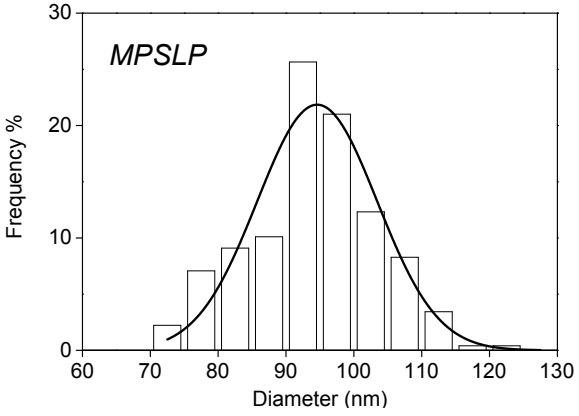

Figure S3. TEM size distribution for MPSLP, counting approximately 300 nanoparticles; average diameter 94 nm (σ = 8.8).

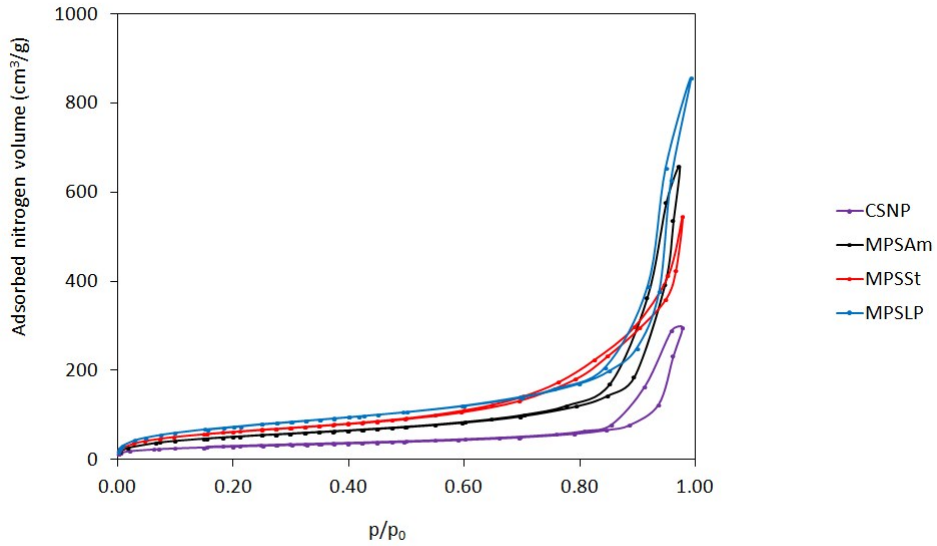

Figure S4. Nitrogen adsorption and desorption isotherms, at 77K, of the indicated samples.

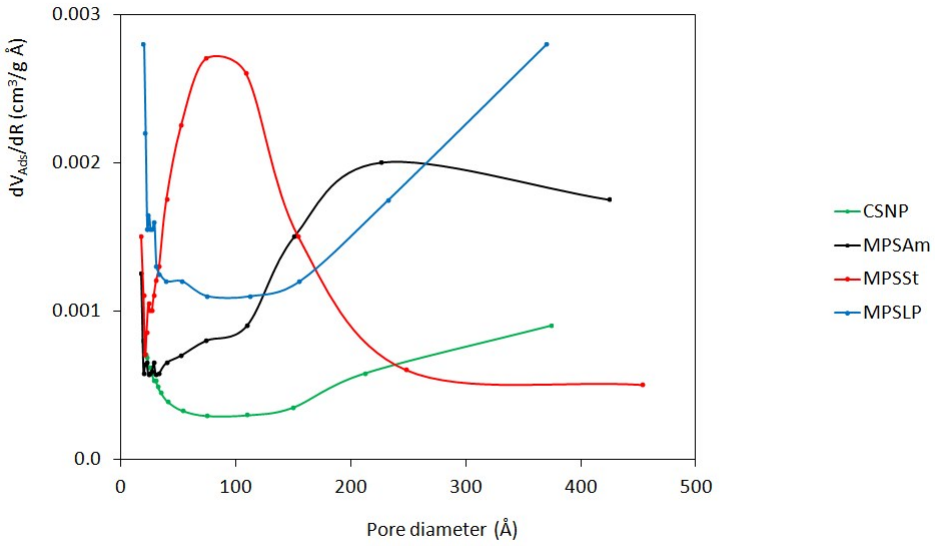

Figure S5. Pore size distribution calculated from nitrogen adsorption data of the indicated samples.

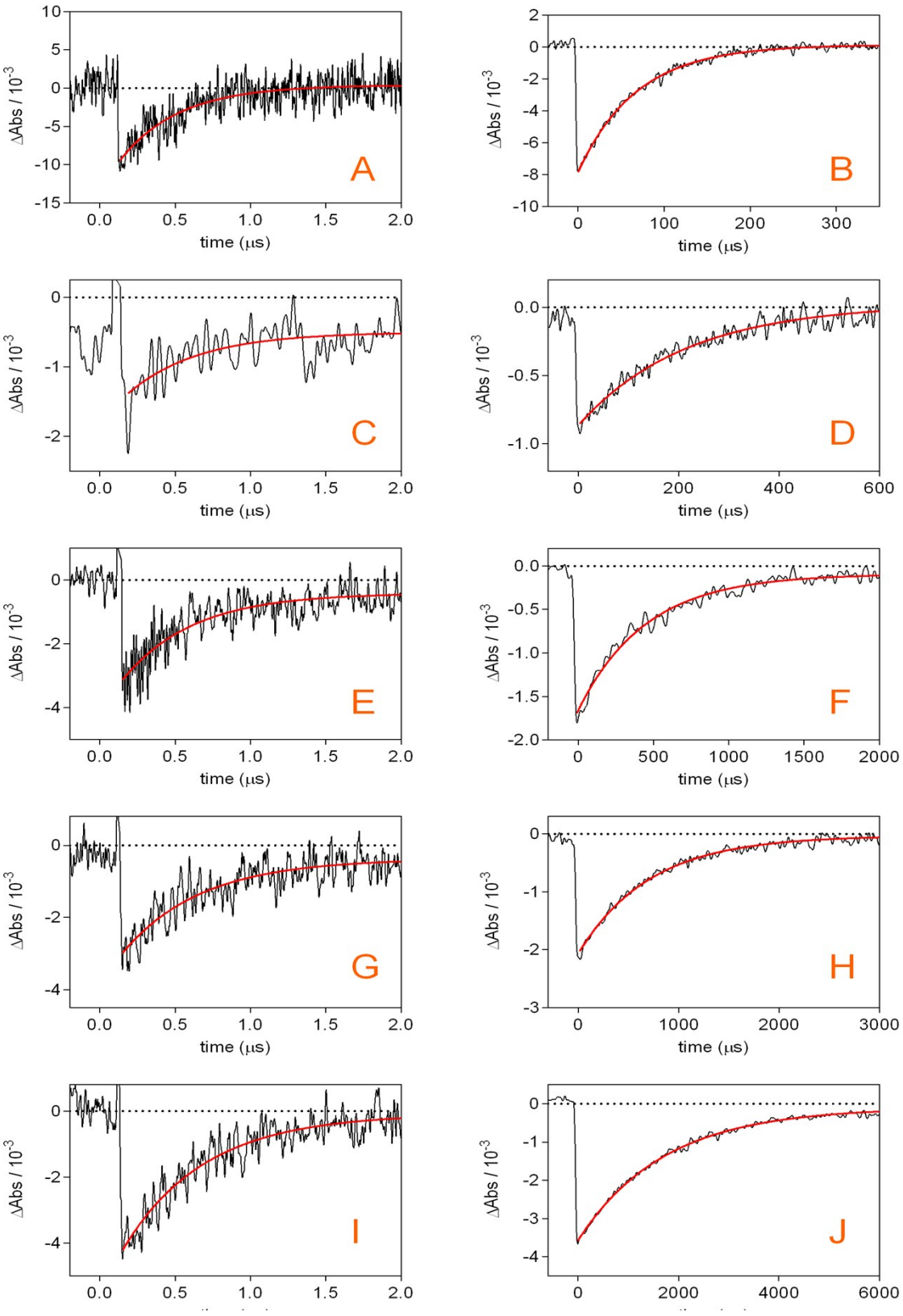
A
B
C
D
E
F
G
H
I
J
ΔAbs / 10-3
time (μs)

Figure S6. Transient absorption signals from PpIX, PpIX-CSNP, PpIX-MPSAm, PpIX-MPSSt and PpIX-MPSLP in air (A,C,E,G,I) and argon-saturated condition (B,D,F,H,J). Observation wavelength 410 nm.

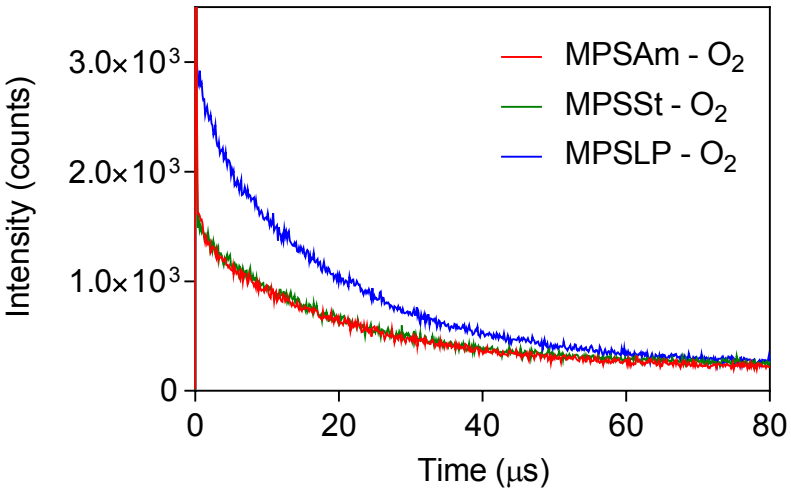

Figure S7. Time-resolved phosphorescence decays at 1270 nm for PpIX-MPSAm, PpIX-MPSSt, PpIX-MPSLP in DMF under oxygen saturated conditions.

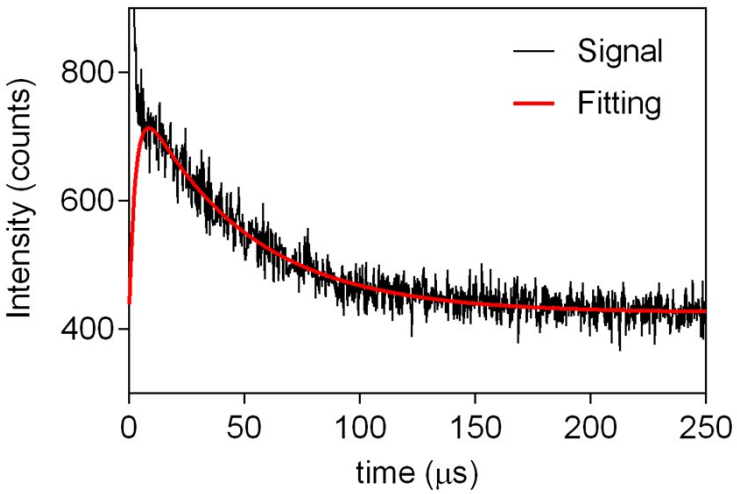

Figure S8. Time-resolved phosphorescence decay at 1270 nm for PpIX-MPSLP in D_2O.

Supporting tables

Table S1. Surface area, mesopore volume, ζ-potential values and relative PpIX quantity per mg of silica, for silica samples.

Sample	Surface area (m^2/g)	Mesopore volume (cm^3/g)	ζ-potential of SiO_2-NH_2 (mV)	Concentration ($nmol_{PpIX}/mg_{silica}$)	ζ- potential of SiO_2-NH_2PpIX (mV)
CSNP	102	0.13	34.3 ± 0.8	1.01 ± 0.04	30.2 ± 0.9
MPSAm	184	0.52	23.4 ± 0.6	0.74 ± 0.03	27.0 ± 0.2
MPSSt	228	0.48	12.3 ± 0.5	0.60 ± 0.02	15.1 ± 0.2
MPSLP	272	0.44	- 0.32 ± 0.13	0.64 ± 0.02	- 5.2 ± 0.2

The specific surface area was determined by the Brunauer, Emmett and Teller (B.E.T.) technique [S. Brunauer, P. H. Emmett and E. Teller, J. Am. Chem. Soc., 60 (1938) 309–319]; mesopore volume was calculated by the BJH method [E. P. Barrett, L. G. Joyner and P. P. Halenda, J. Am. Chem. Soc., 73 (1951) 373–380].

Table S2. PpIX triplet lifetimes in different systems, in air and argon-saturated environment.

System	Air	Argon
$PpIX_{solution}$	0.4 μs	70 μs
PpIX-CSNP	0.3 μs	200 μs
PpIX-MPSAm	0.4 μs	450 μs
PpIX-MPSSt	0.4 μs	720 μs
PpIX-MPSLP	0.4 μs	1.7 ms

Table S3. Fitting parameters obtained from the analysis of singlet oxygen phosphorescence decays sensitized by mesoporous suspensions under oxygen-saturated condition.

Conjugate	$S_{0,1}$ (%)	$S_{0,2}$ (%)	$\tau_{\Delta 1}$ / μs	$\tau_{\Delta 2}$ / μs
PpIX-MPSAm	93%	7%	21.0	3.1
PpIX-MPSSt	92.1%	7.9%	19.2	1.6
PpIX-MPSLP	82%	18%	19.8	2.2

Table S4. Silica and PpIX concentration of each system used in bacterial inactivation.

System	Silica concentration (mg/mL)	PpIX concentration (μM)
PpIX-CSNP	2	2.0
PpIX-MPSAm	2	1.5
PpIX-MPSSt	2	1.2
PpIX-MPSLP	2	1.3

2.3

Planas, O.; Macia, N.; Agut, M.; Nonell, S.; Heyne, B. Distance-Dependent Plasmon-Enhanced Singlet Oxygen Production and Emission for Bacterial Inactivation. *J. Am. Chem. Soc.*, 2016, 138, 2762-2768.
DOI: 10.1021/jacs.5b12704.

See: http://pubs.acs.org/doi/abs/10.1021/jacs.5b12704

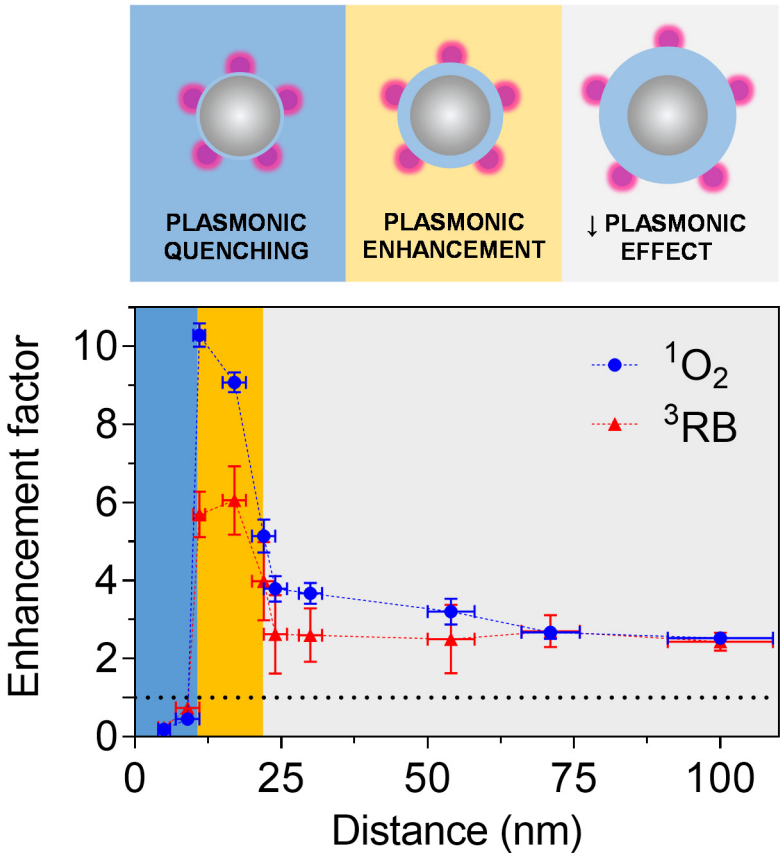

3

General results and discussion

The main results described in the previous chapter are outlined and subsequently discussed. Following, a brief summary of future research in singlet oxgygen photosensitization is presented.

3.1. Discussion of the general results

Spatiotemporal control of the $^1O_2$ photosensitization along with its detection in biological media are still today the major limiting factors for the successful clinical implementation of PDT. The papers collected in chapter two represent different new approaches to overcome the previous problems using the opportunities that the nanotechnology and the biotechnology have brought along. Specifically, we have (1) studied different conjugation strategies of natural and synthetic PSs to nanoparticles and biomolecules, (2) characterized the effect of the nanoparticle surface on the $^1O_2$ production and deactivation, and (3) developed plasmonic PSs to enhance the production and detection of $^1O_2$ in biological media (Figure 3.1).

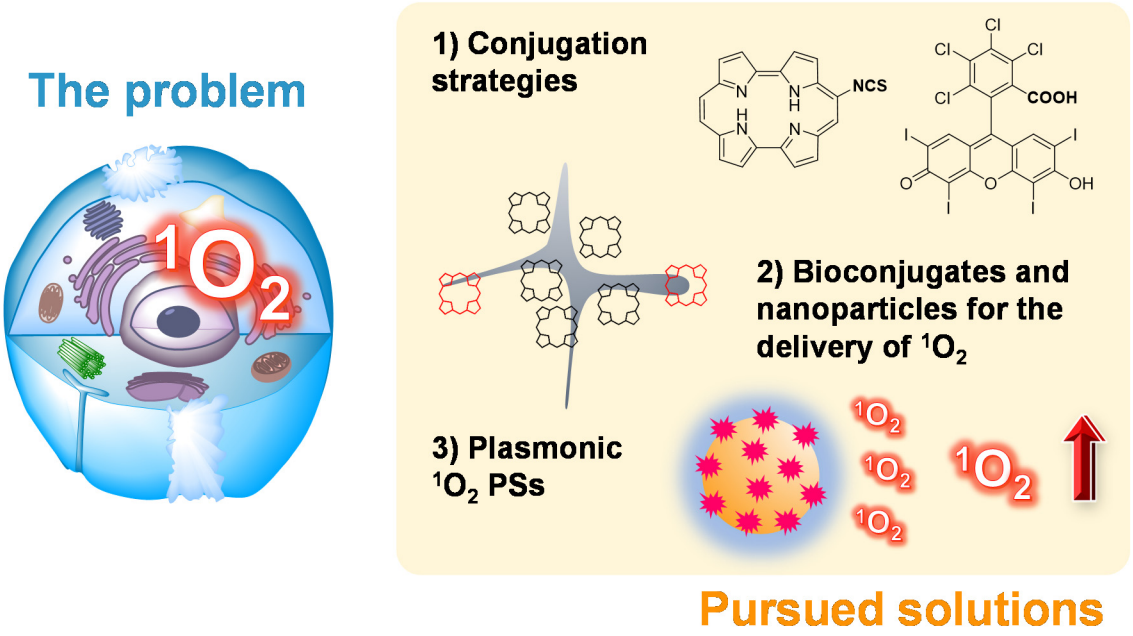

Figure 3.1. In order to improve the generation and detection of $^1O_2$ in biological *milieu* several conjugation strategies of molecular PSs, e.g. porphycene ITCs or rose Bengal, have been studied and applied to the synthesis of bio- and nano-conjugates for the delivery and/or the plasmonic enhancement of $^1O_2$.

On the first basis we used the expertise of the group on the synthesis and characterization of porphycene derivatives to prepare novel 9-isothiocyanate porphycenes (Po-ITCs).[1] We chose ITC groups as a functionality for click chemistry attending to several reasons. Firstly, PS conjugation using the ITC group occurs via an addition reaction yielding a thiourea bridge, thereby preventing the generation of by-products that could potentially contaminate the conjugate. This is a distinct advantage relative to the use of NHS-activated esters, which release the activating hydroxysuccinimide group.[2] Additionally PS-ITCs are stable under regular storage conditions and their conjugation does not require supplementary activating reagents, allowing the bioconjugation to take place under mild conditions.[3,4]

Moreover, several examples of PS-ITCS have been reported encompassing porphyrins and other porphyrin derivatives such as phthalocyanines.[5–8] Likewise prior work performed by Rosas *et. al.* proved the viability of conjugating porphycenes to a monoclonal antibody using the isothiocyanate chemistry.[9] However, in that case, the preparation of 9-glutarimido functionalized porphycenes required several synthetic steps.

In an attempt to simplify the chemistry beyond the conjugation process, we decided to prepare Po-ITCs from the corresponding 9-aminoporphycenes using 1,1′-thiocarbonyldi-2(1H)-pyridone. According to the *state of the art* at that time, we expected that reaction of Po-ITCs with primary and secondary amines would yield the corresponding thiourea moiety. However, to our surprise reaction did not stop on the corresponding thiourea. Isolation of the reaction products of Po-ITCs with amines by NMR and UV/Vis absorption spectroscopy revealed that the originally-formed 9-thiourea porphycene spontaneously evolves to 2-aminothiazolo[4,5-c]porphycenes with a concomitant red-shift on both their absorption and fluorescence emission spectra by more than 70 nm (Figure 3.2). This fluoro-chromogenic reaction was totally unexpected on the basis of the previous reported reactivity since aromatic thioureas cyclize to the corresponding thiazoles only when they contain a halogen leaving group,[10,11] or when they are activated with metals,[12] or in the presence of added oxidants.[13,14]

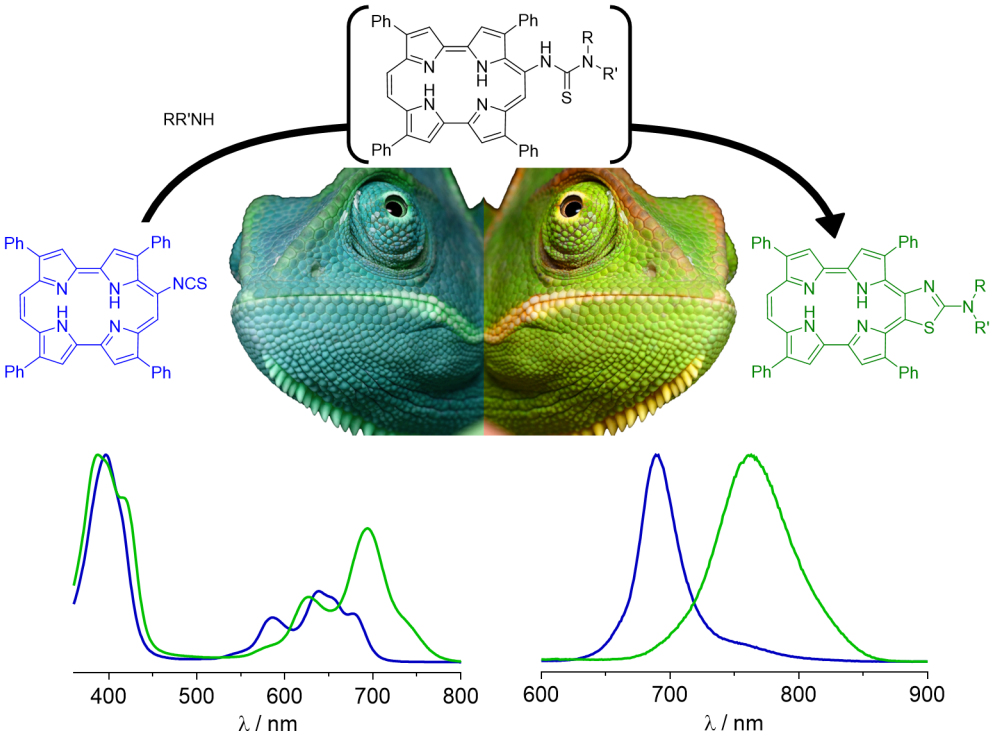

Figure 3.2. Structural, absorption and fluorescence spectral changes upon reaction of 9-isothioyanate-2,7,12,17-tetraphenylporphycene with primary (R'=H) and secondary amines.

Interestingly, conjugates showed fluorescence in the near-infrared (NIR) spectral range and were capable of photosensitizing the production of $^1O_2$ in reasonably high yields (Φ_F≈0.08; Φ_Δ≈0.3). These Φ_F values are comparable to those of approved NIR fluorophores for clinical applications, such as indocyanine green (ICG).[15] However, a clear advantage of Po-ITCs is that they produce $^1O_2$ in high yields, adding a cytotoxic dimension to the regular fluorescent properties of current probes. We thus hypothesized that Po-ITC could be used as novel *click* labels for the preparation of NIR bio- and nanoconjugates which combine in a single nanoentity potential **thera**peutic and diag**nostic** properties; namely a **theranostic** conjugate. As a proof of concept bovine serum albumin (BSA) and alkyl-thiol protected gold nanoclusters (AuNCs), chosen as bio- and nano-models, were successfully labeled with Po-ITCs. The conjugates showed similar photophysical properties to those observed for simple amines, i.e. the conjugates were fluorescent in the NIR and produced $^1O_2$.

We further expanded the labelling chemistry to other amino-containing biomolecules, such as polyallylamine and anti-E.coli monoclonal antibody and tested them against gram-positive and gram-negative bacteria.[16] Results showed that the porphycene conjugates were able to efficiently eliminate bacteria, thereby confirming their cytotoxic effect aiming to the $^1O_2$ generation.[16] Enthusiastic with such results we filed a patent application claiming the use of Po-ITCs labels for phototheranostic applications (see addendum). This patent was awarded the 1st prize of the 4th edition of the VALORTEC contest (Generalitat de Catalunya) for the best valorization and commercialization plan.

Based on all preliminary results we further proposed that Po-ITCs could be used as theranostic labels for the development of an improved protocol for NIR-fluorescence guided cancer surgery. Fluorescence guided surgery is a therapeutic modality by which the emissive properties of fluorescent dyes provide tools to surgeons to locate and discern the malignant cell tissues from the healthy one and then they eliminate it by rejection.[17] However, the current approved NIR fluorescent standard, ICG, suffers from severe drawbacks since surgeons still detect residual tumor in the tumor bed in 50% of cases.[18] Thus there is an urgent need for probes capable of eliminating the residual malignant cells.

A promising candidate for the complete elimination of residual cancer cells using combined cancer-surgery followed by PDT treatment is IRDye700DX®. IRDye700DX® is a Si-phthalocyanine derivate bearing a NHS activated ester which allows its conjugation to targeting moieties.[19,20] Evidence of higher performance of PDT of residual margins after incomplete surgical resection in head and neck cancer models was provided by Moore *et al*.[21] Authors used panitumumab-

IRDye700DX to guide the resection of SCC implemented in the head and neck of mice. According to their results even when 10% or 50% of the tumour was left in the wound bed, long-term growth inhibition of residual disease was observed, suggesting that PDT is capable of eliminating malignant cells left in the surgical procedure.[21] Interestingly, greater suppression of tumour recurrence was achieved in the 90% resection group, indicating that the efficacy of the combined treatment is superior when decreasing amounts of residual tumour.

A clear advantage of the theranostic Po-ITCs labels presented in this thesis with respect to IRDye700DX® is the shift in the emission of the conjugate as the reaction is completed (Figure 3.3). In the prior described examples of PS-ITCs, as the newly-formed thiourea bridge was non-conjugated with the chromophore, no-significant changes on the optical and fluorescent properties of the PSs were observed upon conjugation. This was a disadvantage since it was not possible to distinguish between covalent adducts and non-specific complexes. The latter pose a serious problem in biological therapies as they can be released into the biological *milieu*, altering the result and inducing damage to non-targeted structures. In contrast, thanks to the bathochromic shift in the emission of the conjugates, we have means to detect the reaction completion and thus assure that the conjugate is free of unreacted label. But, what's more, even in the event that some traces of unreacted Po-ITC remained adsorbed in the conjugate, selective irradiation in the NIR (*ca*. 700-720 nm) would only activate the reacted probe, yielding Po-ITC unaffected.

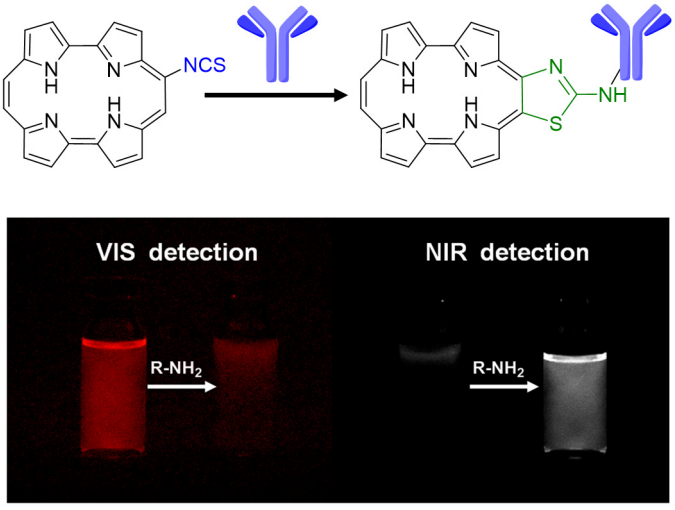

Figure 3.3. Changes in the fluorescence emission of Po-ITCs in the visible and NIR detection channels of a NIR camera before and after the conjugation process. Images from ref [reference].

Finally, the scope of this reaction was extended along two different paths. On one hand, the cyclization of di-ITC porphycenes was studied and it was observed that two thiazole rings were formed, leading to even more dramatic changes in the absorption and fluorescence spectra of the adduct.[16] Also the effect of changing the heteroatoms in the reacting group was explored. Treatment of 9-benzoamido-2,7,12,17-tetraphenyl porphycene with Lawesson's reagent led also to the corresponding thiazolo[4,5-c]porphycene instead of the expected 9-benzothioamide.[1] Thus, cyclisation is not restricted to thioureas but can also be realized with thioamides. Altogether, these results support a novel and specific reaction of porphycenes that allows the formation of fused-porphycene conjugates with red-shifted absorption and fluorescence spectra, and unique photosensitizing properties.

Despite showing promising photophysical properties, in the last two papers of this thesis we decided not to use Po-ITCs but rather more conventional PSs whose photosensitization of $^1O_2$ had been largely characterized as our ultimate goal was to study the effect of the nanoparticle on the $^1O_2$ kinetics. Thus, protoporphyrin IX (PpIX) and rose Bengal (RB) were chosen as model PSs. In order to bind them to the amino-modified surface of silica nanoparticles two different strategies were pursued: PpIX was adsorbed by an acid-base reaction between the carboxylic acids of PpIX and the free amino groups of the silica surface. As PpIX was deprotonated and amino-groups of the silica were protonated, the PS was electrostatically anchored to the nanoparticle's surface. In contrast, RB was covalently bound to the nanoparticle surface using a modified Steglich esterification.

In order to characterize the effect of silica nanoparticles onto the $^1O_2$ production and deactivation, a series silica-PpIX conjugates of distinctive morphologies were prepared:[22] compact silica nanoparticles (CSNP) with no pores, amorphous mesoporous silica nanoparticles (MPSAm), star-shaped mesoporous silica nanoparticles (MPSSt) and large-pore mesoporous nanoparticles (MPSLP). The nanoporosity of the materials was controlled using templating agents of different nature in each synthetic procedure. PpIX was subsequently adsorbed onto the surface of the nanoparticles.

Analysis of the photophysical properties of the silica-PpIX conjugates revealed that aggregation of the PS onto the nanoparticle surface is a critical aspect to bear in mind in order to maximize the $^1O_2$ photosensitization. According to our results, aggregation of PpIX onto the silica nanomaterials limits the production of $^1O_2$. Thus, CSNPs which had the lowest surface for PpIX adsorption showed the least efficient production of $^1O_2$ as PpIX was largely aggregated into the nanoparticle surface. On the other hand, MPSLP were endowed with both the highest surface area and the largest $^1O_2$ production efficiency, in agreement with a lower aggregation of PpIX.

Time-resolved phosphorescence signals at 1270 nm for all nanoconjugates revealed another interesting effect of the silica matrix. As the heterogeneity of the nanosystems was increased from CSNP to MPSLP, two different populations of $^1O_2$ were detected: one generated at the silica-solvent interface and able to escape and decay in the outer bulk solvent and another that relaxes inside the silica pores. While the external component was apparently unaffected by the silica-matrix, the $^1O_2$ population trapped inside the silica nanopores showed a much faster decay. H-D exchange using D_2O revealed that the underlying cause for such effective $^1O_2$ deactivation was the strong quenching by OH groups of the surface silanols and of strongly hydrogen-bonded water molecules remaining from the nanoparticle preparation procedure.

The previous two observations reveal that not only controlling the aggregation state of the PS but also fixing its location is of crucial importance when preparing nanoporous materials for $^1O_2$ delivery. Even if monomeric PSs are dispersed inside nanoporous materials, $^1O_2$ quenching by the nanoparticle components may challenge its accessibility to the targeted cellular components (Figure 3.4). This quenching model can be also applied to other bio- or nanoconstructs, such as genetically encodable PSs or protein nanocarriers where different populations of $^1O_2$ may exist, each of them decaying with their own lifetimes.[23]

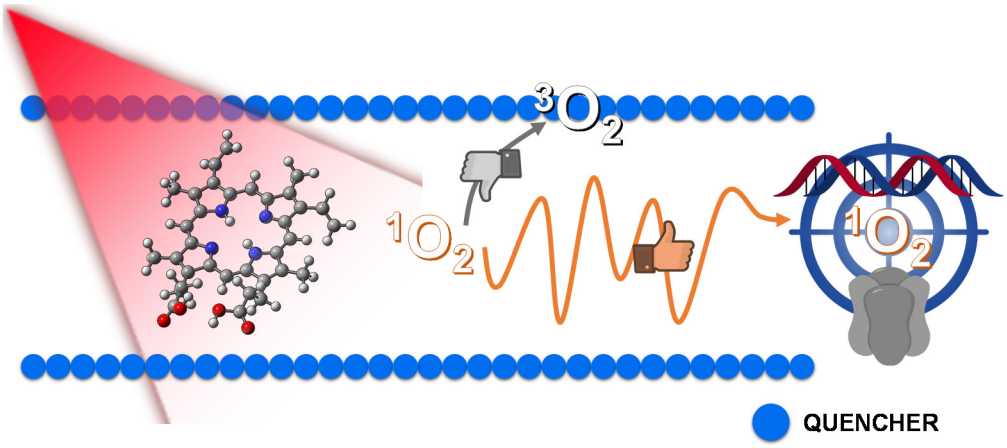

Figure 3.4. Schematic illustration of the $^1O_2$ pathways inside silica pores. Collision with quenching groups of the silica matrix (such as silanol groups or highly H-bonded water molecules) may lead to deactivation of $^1O_2$. Thus location of the PS (in the figure PpIX) is critical to assure that the external target is reached.

Interestingly, CSNPs achieved the highest reduction in the survival fraction of *S. aureus* despite having lowest $^1O_2$ generation efficiency. We believe that this apparent contradiction could be explained as the positive zeta potential of this nanostructure enables the closest proximity to the bacteria, thereby facilitating the delivery of $^1O_2$ and/or PpIX to the bacteria. Thus, bacterial inactivation studies underlined that an increase on the $^1O_2$ generation efficiency does not ultimately translate in higher phototoxicity and that other physicochemical parameters such as the nanoparticle zeta-potential and morphology appear at least as crucial. Altogether, the work carried out in this publication evidences the importance of a rigorous characterization of the photophysical properties of molecular PS bound to nanoparticles as well as exhaustively studying its inactivation efficiency, as the two effects might not necessarily follow the same trend. Not only $^1O_2$ should be produced in high yields but also close to the targeted cellular components as this would ultimately translate in cell death.

All the knowledge acquired on silica nanostructures was applied to design plasmonic nanostructures capable of enhancing the $^1O_2$ production and its radiative deactivation. Prior reports on the plasmonic enhancement of $^1O_2$ had shown its viability on solid supports[24–26] as well as in solution.[27–33] However, in these last series of experimental designs no control in the MNP-PS distance was achieved, making the rationalization of the plasmonic effects extremely challenging. Moreover to that date, plasmon-enhanced $^1O_2$ phosphorescence had only been demonstrated for nanoparticles attached to solid supports.[25,26] In order to fully exploit this phenomena and improve the $^1O_2$ detection in biological *milieu* it was necessary to translate it to biocompatible plasmonic nanomaterials that could be readily dispersed into bulk solution.

In a collaborative work with the group of Prof. Dr. Belinda Heyne form the University of Calgary we designed a series new plasmonic nanostructures capable of enhancing not only the $^1O_2$ production, and therefore their photodynamic activity, but also the $^1O_2$ phosphorescence emission, which impacts in our ability to monitor $^1O_2$ in biological media.[34] Although this is nicely described in our published work, I would like to append here a brief disclosure of how elusive and tricky it has been to achieve success in this particular objective.

I started this journey during my first year as master student (4 years before the publication of the paper). At that time our group had already reported the enhancement of $^1O_2$ production and phosphorescence by C_{60}@silver-island films[26] and we were thrilled by the opportunities that the plasmonic enhancement of $^1O_2$ would bring if we could move it to biological *milieu*. However, at that point it was not clear which factors governed the plasmonic enhancement of $^1O_2$. Actually, most of the theories were taken by analogy to the metal enhanced fluorescence and

phosphorescence of organic and inorganic luminophores.[35–39] It seemed that factors such as the position of the plasmon band (and therefore the nature, size and shape of the MNP), the excitation wavelength, the absorption of the luminophore, the distance between the metal nanoparticle and the luminophore and the scattering component of the MNPs were of critical importance.[40–46] It was also proposed that in order to boost a radiative transition, the plasmon band of the MNPs should match the energy of the transition to be enhanced.[25,47]

Thus, in collaboration with the group of Prof. Dr. Jesus de la Fuente at the Instituto de Nanociencia de Aragón, we first tried to use water dispersions of gold nanoparticles with a plasmon band in the NIR, matching the $^1O_2 \rightarrow {}^3O_2$ transition. Those nanoparticles, designated by the group of Prof. de la Fuente as *nanonachos*, were endowed with a plasmon band at *ca*. 1000, 1100 and 1250 nm which, according to reported results, should have been ideal to achieve plasmonic enhancement of $^1O_2$ luminescence.[25] In order to achieve different distances (albeit uncontrolled) between the metal core and the PSs we mixed them with PS of distinct nature (neutral, cationic and anionic).[48] Results showed a clear reduction in the $^1O_2$ phosphorescence emission intensity upon increasing the ratio metal nanoparticles/PS while leaving the $^1O_2$ kinetics unaffected. We proposed that *nanonachos* acted as inner filters of the $^1O_2$ phosphorescence emission, thereby reducing the signal. Albeit this nanosystem was inspired in the gold nanodiscs support previously reported by Toftegaard *et al.*[25] a critical difference between the two platforms should to be brought into light. In a solid support all photons emitted by $^1O_2$ in the direction of the detector find no obstacles and thus can be easily detected. In contrast, nanoparticles can move freely in solution, thereby blocking the photons emitted by $^1O_2$ before they reach the detector.

As reports on $^1O_2$ enhancement in solution began to appear for gold and silver nanoparticles in solution, we decided to try this kind of nanoparticles. In first attempts, silver and gold nanospheres with plasmon bands at 400 and 532 nm respectively were prepared and tested by mixing them with PS of distinct nature (neutral, cationic and anionic). In all cases quenching of $^1O_2$ was observed and we proposed that nanoparticles acted as inner filters of light absorption by the PSs.[48] Moreover, no control of the distance between the PS and the metal core was achieved.

At the very end of 2013 the group of Prof. Heyne reported a nanosystem capable of enhancing the $^1O_2$ production by RB based on silver nanoparticles coated with a silica shell of approximately 22 nm thick.[29] We particularly liked such nanosystem since the distance between RB and the metal core was elegantly fixed. Moreover we observed that it could be easily translated into a platform to study the effects of the MNP-PS distance on the $^1O_2$ production efficiency. We contacted Prof. Heyne and established a collaboration with her group. After careful examination

of the photophysical properties of a sample of her nanomaterial, we concluded that the silver core was capable not only of enhancing the production of $^1O_2$ by RB but also its radiative decay. A year later we met again and jointly designed the experiments that 2 years later led to the publication in the Journal of the American Chemical Society.

Based on our experience, we decided to stick to the use of RB as $^1O_2$ PS and silver spheres as a metal core since this PS-MNP pair had already proven to be successful, not only in the disclosure by Mooi *et al.*[29] but in prior reports on the $^1O_2$ enhancement by silver island films.[24] In my opinion that was a wise choice since the plasmonic enhancement of the $^1O_2$ production has been strongly dependent on the PS-MNP pair. As stated in the introduction, gold nanoconstructs/PpIX and silver nanoparticles/RB are the most studied *tandems* for $^1O_2$ production enhancement. Other elements that supported the use of the reported platform were that (1) the size of silica shell could be easily and nicely controlled with the appropriate reducing procedure, (2) it allowed the covalent binding of RB to its surface, thereby fixing its location and avoiding the aggregation of the PS and (3) by choosing RB as the PS, we not only guaranteed the use of a FDA approved drug with excellent biocompatibility, but we also ensured spectral overlap between the PS absorption and the plasmon band of the metal nanoparticles, thus enabling the strongest plasmon-enhanced excitation.

According to our results the distance profile of $^1O_2$ enhancement shows three distinct regimes (Figure 3.5): at short distances between RB and the Ag core, the metal quenches the $^1O_2$ production; at intermediate distances $^1O_2$ production is greatly enhanced with a maximum at a RB-Ag distance of 11 nm; at even longer distances the enhancement factor falls and levels off at a value slightly above 1, owing to a slightly enhanced light absorption by scattering due to the larger nanoparticles. This distance dependence is in line with previous documented plasmon enhanced fluorescence of various dyes and metal nanoparticles.[46,49–51] Interestingly, the phosphorescence of ^{3}RB follows an analogous distance dependence(Figure 3.5), yet the maximum enhancement factor for RB phosphorescence is *ca*. 40% smaller than that of $^1O_2$ phosphorescence. Comparison of the ^{3}RB and $^1O_2$ phosphorescence enhancements indicates that not only the production of $^1O_2$ but also to its radiative decay constant are enhanced. This was the first demonstration that the radiative decay of O_2 can be enhanced by metal nanoparticles in suspension.

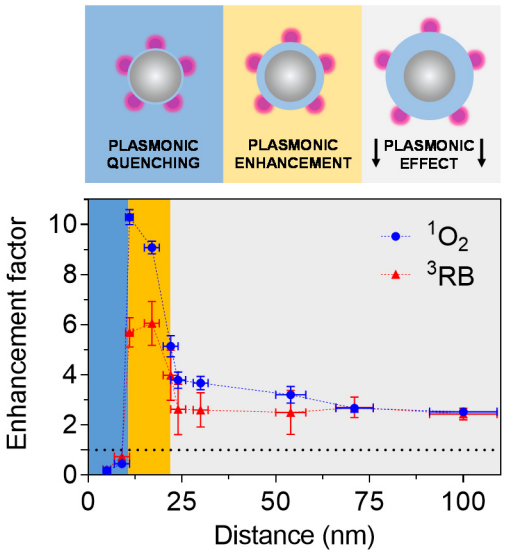

Figure 3.5. $^1O_2$ and ^{3}RB phosphorescence enhancement factors as a function of the distance between the silver core and the PS.

Also of remarkable interest is the observation that the enhancement factors obtained by direct phosphorescence measurements of $^1O_2$ are larger than those determined using the indirect $^1O_2$ probe 9,10-anthracenediyl-bi(methylene)dimalonic acid (ABDA). This confirms that the enhanced emission observed for $^1O_2$ results from two contributions: higher $^1O_2$ production and higher probability of its radiative decay. Actually, assuming that all $^1O_2$ molecules that are generated react with the ABDA probe and that its reactivity against $^1O_2$ is exactly the same for both plasmonic nanoparticles and their etched counterparts, an approximation of the distance dependence of the phosphorescence enhancement of $^1O_2$ can be estimated by making the ratio of the enhancement factors estimated using both the direct and the indirect approaches (Figure 3.6). According to this distance dependence, the maximum enhancement of the $^1O_2$ radiative rate takes place at *ca.* 11 nm between the PS and the metal core, in good agreement with prior reports on radiative rate enhancement for fluorescence and phosphorescence of organic dyes.[46,51–53]

We further assessed the possibility to enhance the phototoxicity of RB and the detection limits of $^1O_2$ in cells using the above prepared plasmonic nanoparticles. We thus incubated the hybrid nanoparticles endowed with the maximum enhancement factor of $^1O_2$ production and emission (sample of silica shell of 11 nm) and their *etched* controls with both *Staphylococcus aureus* and *Escherichia coli* as models of Gram-positive and Gram-negative bacteria respectively. After incubation for a certain time, and washing of the cell cultures, $^1O_2$ signals were collected using time resolved techniques. Interestingly, a clear $^1O_2$ phosphorescence signal was detected for the hybrid plasmonic nanoparticles, whereas the signal was buried into the noise for the *etched* (control) nanoparticles. Such results confirmed that plasmonic photosensitizers of $^1O_2$ could certainly improve the detection of $^1O_2$ in biological *milieu*.

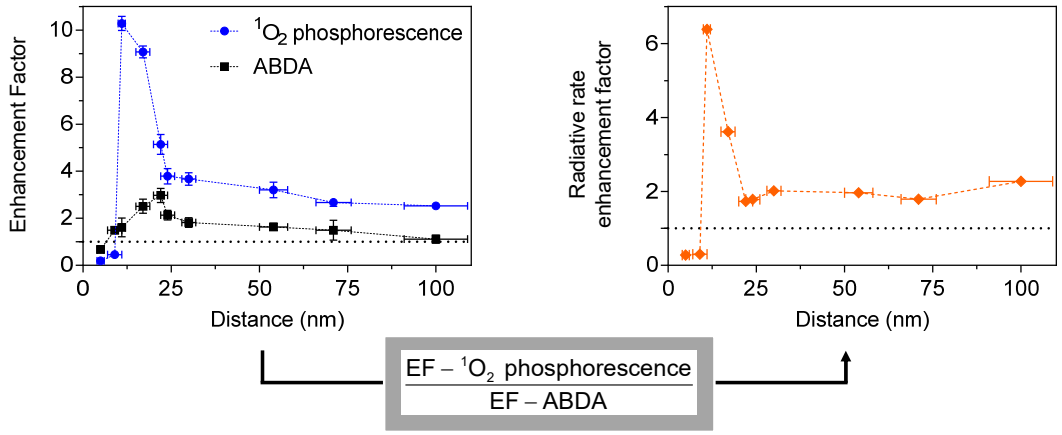

Figure 3.6. The ratio between the enhancement factors estimated using the detection of the $^1O_2$ phosphorescence and the measurement of ABDA quenching rate yields the distance profile of the radiative rate enhancement factors.

A second aliquot of cells incubated with the hybrid nanoparticles and their control was used to evaluate the ability of hybrid plasmonic nanoparticles to photoinactivate bacteria compared to their etched counterparts and free RB. According to our results the photoinactivation efficiency of RB against both *Staphylococcus aureus* and *Escherichia coli* was significantly enhanced by the plasmonic nanoparticles. We thus demonstrated that well-designed plasmonic $^1O_2$ photosensitizers showed great potential for the photodynamic inactivation of bacteria.

In light of all results, it seems reasonable to conclude that hybrid plasmonic-PS nanoparticles show great promise for improving the efficiency of molecular PS for PDT as well as for $^1O_2$ dosimetry using real-time phosphorescence monitoring. However, based on our experience it is also safe to conclude that fine control of the metal-PS distance and the choice of the metal nanoparticle – PS tandem is crucial in order to achieve the desired plasmonic effects.

3.2 Summary and outlook

In summary, three new strategies to improve the generation and detection of $^1O_2$ in biological media have been proposed. As a first approximation a novel fluorochromogenic click reaction for the labeling of biomolecules and nanoparticles using Po-ITCs has been developed. This new technology shows great potential for the preparation of theranostic bio- and nanoprobes since porphycenes have high fluorescence emission quantum yields, remarkable Φ_Δ values and can be easily conjugated to antibodies, antibody fragments and nanoparticles containing amino residues. Thus, thanks to the technology developed in this doctoral thesis, a single entity can be provided with both **thera**peutic and diag**nostic** capabilities resulting in a **theranostic** bio- or nanoconjugate. However, in order to achieve its full potential for medical translation, the *hit* identified in this thesis should be converted into a *lead* candidate by adding incremental value to the technology. Work is currently in progress to explore such applications using a new porphycene candidate and results shall be reported in due course

The second paper, devoted to the analysis of the effect of the morphology of silica nanoparticles onto the $^1O_2$ photosensitization, evidences the importance of a thorough characterization of the effects of every nanostructure on the $^1O_2$ kinetics for a rational design of an ideal *nanoproducer* of $^1O_2$. In the case of silica nanostructures, mesoporous silica nanoparticles of large pores show great potential for boosting the production of $^1O_2$ by hydrophobic PS as their large surface to volume ratio allows for high absorption of molecular PS while preventing its aggregation. However, the precise location of the PS should be adequately controlled in order to avoid quenching by the nanoparticle surface.

On the other side, photoinactivation studies performed in this work are not fully conclusive since the electrostatic adsorption of PpIX to the nanomaterial surface may allow a partial leak of the PS and the nanoconjugates were endowed with different zeta-potential values. Future studies should be focused on preparing and studying mesoporous nanomaterials with covalently-bound PSs and of equal zeta-potential in order to rule out their effects in photoinactivation studies. Moreover, different surface/PS ratios and different location of the PS should be tested to confirm the results of the present work

Finally, the last paper outlines the potential of nanoplasmonics in improving the production and detection of $^1O_2$ in biological environments thanks to the nanoantena effects. Still, particular attention should be paid to the design of water dispersible plasmonic nanostructures and factors such as the pair metal nanoparticle/PS or the distance between the metal core and the PS should be precisely controlled. Moreover, from other metal-enhanced processes it is well known that

other factors such as the excitation wavelength or the relative position of the plasmon band may play a fundamental role on the plasmonic enhancement of $^1O_2$. Thus, future research should focus on clarifying such phenomena.

Altogether, the results presented in this thesis proof that the combination of the advances in fields as diverse as molecular engineering, bioengineering and nanotechnology offer new and promising opportunities to address some of the main current challenges in the $^1O_2$ field: to provide spatiotemporal control on its production and to boost the performance of current PSs.

3.3. References

(1) Planas, O.; Gallavardin, T.; Nonell, S. *Chem. Commun.* **2015**, *51* (26), 5586.

(2) Cline, G. W.; Hanna, S. B. *J. Am. Chem. Soc.* **1987**, *109* (10), 3087.

(3) Bullous, A. J.; Alonso, C. M. A.; Boyle, R. W. *Photochem. Photobiol. Sci.* **2011**, *10* (5), 721.

(4) Pereira, P. M. R.; Korsak, B.; Sarmento, B.; Schneider, R. J.; Fernandes, R.; Tomé, J. P. C. *Org. Biomol. Chem.* **2015**, *13* (9), 2518.

(5) Clarke, O. J.; Boyle, R. W. *Chem. Commun.* **1999**, *21*, 2231.

(6) Hudson, R.; Carcenac, M.; Smith, K.; Madden, L.; Clarke, O. J.; Pèlegrin, A.; Greenman, J.; Boyle, R. W. *Br. J. Cancer* **2005**, *92* (8), 1442.

(7) Sutton, J. M.; Clarke, O. J.; Fernandez, N.; Boyle, R. W. *Bioconjug. Chem.* **2002**, *13* (2), 249.

(8) Duan, W.; Smith, K.; Savoie, H.; Greenman, J.; Boyle, R. W. *Org. Biomol. Chem.* **2005**, *3* (13), 2384.

(9) Rosàs, E.; Santomá, P.; Duran-Frigola, M.; Hernández, B.; Llinàs, M. C.; Ruiz-González, R.; Nonell, S.; Sánchez-García, D.; Edelman, E. R.; Balcells, M. *Langmuir* **2013**, *29* (31), 9734.

(10) Feng, E.; Huang, H.; Zhou, Y.; Ye, D.; Jiang, H.; Liu, H. *J. Comb. Chem.* **2010**, *12* (4), 422.

(11) Kim, S.-G.; Jung, S.-L.; Lee, G.-H.; Gong, Y.-D. *ACS Comb. Sci.* **2013**, *15* (1), 29.

(12) Nakamura, I.; Yamamoto, Y. *Chem. Rev.* **2004**, *104* (5), 2127.

(13) Jordan, A. D.; Luo, C.; Reitz, A. B. *J. Org. Chem.* **2003**, *68* (22), 8693.

(14) Wang, R.; Yang, W.; Yue, L.; Pan, W.; Zeng, H. *Synlett* **2012**, *23* (11), 1643.

(15) Escobedo, J. O.; Rusin, O.; Lim, S.; Strongin, R. M. *Curr. Opin. Chem. Biol.* **2010**, *14* (1), 64.

(16) Nonell, S.; Planas, O.; Gallavardin, T. *WO2015197510 (A1)* **2015**.

(17) Nguyen, Q. T.; Tsien, R. Y. *Nat. Rev. Cancer* **2013**, *13* (9), 653.

(18) Keating, J.; Tchou, J.; Okusanya, O.; Fisher, C.; Batiste, R.; Jiang, J.; Kennedy, G.; Nie, S.; Singhal, S. *J. Surg. Oncol.* **2016**, *113* (5), 508.

(19) Peng, X.; Draney, D. R.; Volcheck, W. M.; Bashford, G. R.; Lamb, D. T.; Grone, D. L.; Zhang, Y.; Johnson, C. M. *Biomed. Opt. 2006* **2006**, *60970*, 1.

(20) Mitsunaga, M.; Ogawa, M.; Kosaka, N.; Rosenblum, L. T.; Choyke, P. L.; Kobayashi, H. *Nat. Med.* **2011**, *17* (12), 1685.

(21) Moore, L. S.; de Boer, E.; Warram, J. M.; Tucker, M. D.; Carroll, W. R.; Korb, M. L.; Brandwein-Gensler, M. S.; van Dam, G. M.; Rosenthal, E. L. *Cancer Med.* **2016**, *5* (7), 1526

(22) Zampini, G.; Planas, O.; Marmottini, F.; Gulías, O.; Agut, M.; Nonell, S.; Latterini, L. *RSC Adv.* **2017**, *7* (24), 14422.

(23) Lepeshkevich, S. V.; Parkhats, M. V.; Stasheuski, A. S.; Britikov, V. V.; Jarnikova, E. S.; Usanov, S. A.; Dzhagarov, B. M. *J. Phys. Chem. A* **2014**, *118* (10), 1864.

(24) Zhang, Y.; Aslan, K.; Previte, M. J. R.; Geddes, C. D. *Proc. Natl. Acad. Sci. U. S. A.* **2008**, *105* (6), 1798.

(25) Toftegaard, R.; Arnbjerg, J.; Daasbjerg, K.; Ogilby, P. R.; Dmitriev, A.; Sutherland, D. S.; Poulsen, L. *Angew. Chem. Int. Ed.* **2008**, *47* (32), 6025.

(26) Ragàs, X.; Gallardo, A.; Zhang, Y.; Massad, W.; Geddes, C. D.; Nonell, S. *J. Phys. Chem. C* **2011**, *115* (33), 16275.

(27) Khaing Oo, M. K.; Yang, Y.; Hu, Y.; Gomez, M.; Du, H.; Wang, H. *ACS Nano* **2012**, *6* (3), 1939.

(28) Hayden, S. C.; Austin, L. A.; Near, R. D.; Ozturk, R.; El-Sayed, M. A. *J. Photochem. Photobiol. A* **2013**, *269*, 34.

(29) Mooi, S. M.; Heyne, B. *Photochem. Photobiol.* **2013**, *90* (39), 85.

(30) de Melo, L. S. A.; Gomes, A. S. L.; Saska, S.; Nigoghossian, K.; Messaddeq, Y.; Ribeiro, S. J. L.; de Araujo, R. E. *J. Fluoresc.* **2012**, *22* (6), 1.

(31) Rapulenyane, N.; Antunes, E.; Nyokong, T. *New J. Chem.* **2013**, *37* (4), 1216.

(32) Huang, X.; Tian, X.-J.; Yang, W.; Ehrenberg, B.; Chen, J.-Y. *Phys. Chem. Chem. Phys.* **2013**, *15* (38), 15727.

(33) Mthethwa, T. P.; Tuncel, S.; Durmuş, M.; Nyokong, T.; Durmus, M. *Dalton Trans.* **2013**, *42* (14), 4922.

(34) Planas, O.; Macia, N.; Agut, M.; Nonell, S.; Heyne, B. *J. Am. Chem. Soc.* **2016**, *138* (8), 2762.

(35) Geddes, C. D.; Lakowicz, J. R. *J. Fluoresc.* **2002**, *12* (2), 121.

(36) Geddes, C. D.; Parfenov, A.; Lakowicz, J. R. *Appl. Spectrosc.* **2003**, *57*, 526.

(37) Aslan, K.; Lakowicz, J. R.; Szmacinski, H.; Geddes, C. D. *J. Fluoresc.* **2004**, *14*, 677.

(38) Aslan, K.; Gryczynski, I.; Malicka, J.; Matveeva, E.; Lakowicz, J. R.; Geddes, C. D. *Curr. Opin. Biotechnol.* **2005**, *16*, 55.

(39) Zhang, Y. X.; Aslan, K.; Malyn, S. N.; Geddes, C. D. *Chem. Phys. Lett.* **2006**, *427* (4–6), 432.

(40) Lakowicz, J. R.; Ray, K.; Chowdhury, M.; Szmacinski, H.; Fu, Y.; Zhang, J.; Nowaczyk, K. *Analyst* **2008**, *133* (10), 1308.

(41) Zhang, Y.; Dragan, A.; Geddes, C. D. *J. Phys. Chem. C* **2009**, *113* (28), 12095.

(42) Pribik, R.; Dragan, A. I.; Zhang, Y.; Gaydos, C.; Geddes, C. D. *Chem. Phys. Lett.* **2009**, *478* (1–3), 70.

(43) Dragan, A. I.; Geddes, C. D. *Appl. Phys. Lett.* **2012**, *100* (9), 93115.

(44) Mahmoud, M. A.; Chamanzar, M.; Adibi, A.; El-Sayed, M. A. *J. Am. Chem. Soc.* **2012**, *134* (14), 6434.

(45) Karolin, J.; Geddes, C. D. *Phys Chem Chem Phys* **2013**, *15* (38), 15740.

(46) Mishra, H.; Mali, B. L.; Karolin, J.; Dragan, A. I.; Geddes, C. D. *Phys. Chem. Chem. Phys.* **2013**, *15* (45), 19538.

(47) Toftegaard, R.; Arnbjerg, J.; Cong, H.; Agheli, H.; Sutherland, D. S.; Ogilby, P. R. *Pure Appl. Chem.* **2011**, *83* (4), 885.

(48) Planas, O. Interacción del oxígen molecular con nanoclústeres y nanosondas plasmónicas: producción e intensificación del oxígeno singlete, Institut Químic de Sarrià - Universitat Ramón Llull, 2013.

(49) Pompa, P. P.; Martiradonna, L.; Torre, A. Della; Sala, F. Della; Manna, L.; De Vittorio, M.; Calabi, F.; Cingolani, R.; Rinaldi, R. *Nat. Nanotechnol.* **2006**, *1* (2), 126.

(50) Cheng, D.; Xu, Q.-H. *Chem Commun* **2007**, No. 3, 248.

(51) Abadeer, N. S.; Brennan, M. R.; Wilson, W. L.; Murphy, C. J. *ACS Nano* **2014**, *8* (8), 8392.

(52) Anger, P.; Bharadwaj, P.; Novotny, L. *Phys. Rev. Lett.* **2006**, *96* (11), 113002.

(53) Ming, T.; Chen, H.; Jiang, R.; Li, Q.; Wang, J. *J. Phys. Chem. Lett.* **2012**, *3* (2), 191.

4

Conclusions

Conclusions

1. A novel fluoro- and chromogenic click reaction of porphycenes has been discovered. 9-isothiocyanatoporphycenes react with primary and secondary amines to yield 2-aminothiazolo[4,5-c]porphycene derivatives that show valuable near-infrared fluorescence and are capable of photosensitizing the production of the cytotoxic species singlet oxygen. This discovery paves the way for the development of near-infrared active phototheranostic agents based on porphycene bio- and nano-conjugates.

2. The scope of the novel porphycene cyclization reaction has been extended to di-isothiocyanates and amidoporphycenes using the Lawesson's reagent leading to a variety of π-expanded porphycenes with unique absorption, fluorescence and photosensitizing properties.

3. The size, shape and porosity of silica nanoparticles exerts a dramatic influence on the ability of silica-bound photosensitizers to produce singlet oxygen under exposure to light. Aggregation of the photosensitizer onto the silica surface and quenching of singlet oxygen by superficial moieties hinder the production and accessibility to $^1O_2$.

4. Precise control of the photosensitizer-to-metal nanoparticle distance is essential to obtain an optimum plasmonic enhancement of singlet oxygen production. Three different regions have been identified: at distances below 10 nm the metal quenches the production and phosphorescence of singlet oxygen; at intermedium distances, between 10 and 20 nm, the production and phosphorescence of singlet oxygen is greatly enhanced; finally, at distances over 20 nm the enhancement factor falls off.

5. Plasmonic metal-silica core-shell nanoparticles with surface-coated rose Bengal show excellent prospects as a novel type of photoantimicrobial agents and hold great promises for the real-time monitoring of singlet oxygen in biological milieu.

5. LIST OF ABBREVIATIONS

ABDA	9,10-anthracenediyl-bi(methylene)dimalonic acid
AgNPs	Silver nanoparticles
ATAZPo	2-aminothiazolo[4,5-c]porphycene
AuNCs	Gold nanoclusters
BSA	Bovine serum albumin
CSNP	Compact silica nanoparticles
ITC	Isothiocyanate
mAb	Monoclonal antibody
MNPs	Metal nanoparticles
MPSAm	Mesoporous silica nanoparticles
MPSSt	Star-shaped mesoporous silica nanoparticles
MPSLP	Large pore mesoporous silica nanoparticles
NIR	Near-infrared
PDT	Photodynamic therapy
PIT	Photoimmunotherapy
Po-ITCs	9-isothiocyanate porphycenes
PpIX	Protoporhyrin IX
PS	Photosensitizer
RB	Rose bengal
ROS	Reactive oxygen species
$^1O_2$	Singlet molecular oxygen
$^3O_2$	Ground state molecular oxygen
TAZPo	thiazolo[4,5-c]porphycene
Φ_Δ	Singlet oxygen quantum yield

6

Addenda

Other publications derived from this thesis are listed below:

Papers

6.1. **Planas, O.**; Bresolí-Obach, R.; Nos, J.; Gallavardin, T.; Ruiz-Gonzalez, R.; Agut, M.; Nonell, S.; Synthesis, photophysical characterization and photoinduced antibacterial activity of methylene blue-loaded amino- and mannose-targeted mesoporous silica nanoparticles. *Molecules*, 2015, 20, 6284-6298. DOI:10.3390/molecules20046284.

6.2. **Planas, O.**; Tejedor-Estrada, R.; Nonell, S.; Tautomerism and dual fluorescence in 9-substituted n-propyl- and methoxyethyl- porphycenes. *J. Porphyrins Phthalocyanines* 2012, 16, 633-640. DOI: 10.1142/S1088424612500526

Patent applications

6.3. **Planas, O.**; Gallavardin, T.; Nonell, S.; NEAR-INFRARED FLUOROGENIC PORPHYCENE DERIVATIVES AS FLUORESCENT LABELS FOR PHOTODIAGNOSIS AND PHOTOTHERAPEUTIC USE. Application number: PCT/EP2015/063907 and publication number WO/2015/197510.

Book Chapters

6.4. **Planas, O.**; Boix-Garriga, E.; Rodriguez-Amigo, B.; Torra, J.; Bresolí-Obach, R.; Flors, C.; Viappiani, C.; Agut, M.; Ruiz-González, R.; Nonell S.; Chapter 9: *Newest approaches to singlet oxygen photosensitisation in biological media.* In Photochemistry: Volume 42; Fasani, E.; Albini, A., Eds.; Photochemistry; Royal Society of Chemistry, 2015, 42, 233-278. ISBN: 978-1-84973-956-6.

6.5. **Planas, O.**; Gallavardin, T.; Nonell, S.; Chapter 4: *Unusual Properties of Asymmetric Porphycenes.* In Handbook of Porphyrin Science, Volume 41; Guilard, R.; Smith, K. M.; Kadish K. M. Eds.; World Scientific, 2016,41, 299-349. ISBN: 978-981-3143-52-4.

6.6. Boix-Garriga, E.; Rodriguez-Amigo, **Planas, O.**; Nonell S.; Chapter 2: *Properties of Singlet Oxygen.* In Singlet Oxygen: Applications in Biosciences and Nanosciences, Volume 1; Flors C.; Nonell, S., Eds. Royal Society of Chemistry, 2016, 1, 23-46. ISBN: 978-1-78262-038 -9.

6.7. Rodriguez-Amigo, B.; **Planas, O**; Torra, J; Bresolí-Obach, R.; Ruiz-González, R.; Nonell, S.; Chapter 2: *Photosensitisers for Photodynamic Therapy: State of the Art and Perspectives.* In Photodynamic Medicine: From Bench to Clinic; Kostron, H.; Hasan, T., Eds.; Royal Society of Chemistry, 2016, 1, 23-62. ISBN: 978-1-78262-451-6.